Astronomy & Astrophysics

ViCTORIA project: The LOFAR HBA Virgo Cluster Survey[*]

H. W. Edler[1] , F. de Gasperin[1,2] , T. W. Shimwell[3,4] , M. J. Hardcastle[5], A. Boselli[6], V. Heesen[1] , H. McCall[7],
D. J. Bomans[8], M. Brüggen[1] , E. Bulbul[9], K. T. Chyży[10], A. Ignesti[11], A. Merloni[9], F. Pacaud[7], T. H. Reiprich[7],
I. D. Roberts[3], H. J. A. Rottgering[3], and R. J. van Weeren[3]

[1] Hamburger Sternwarte, University of Hamburg, Gojenbergsweg 112, 21029 Hamburg, Germany
   e-mail: henrik.edler@hs.uni-hamburg.de
[2] INAF – Istituto di Radioastronomia, via P. Gobetti 101, Bologna, Italy
[3] Leiden Observatory, Leiden University, PO Box 9513, 2300 RA Leiden, The Netherlands
[4] ASTRON, Netherlands Institute for Radio Astronomy, Oude Hoogeveensedijk 4, 7991 PD Dwingeloo, The Netherlands
[5] Centre for Astrophysics Research, University of Hertfordshire, College Lane, Hatfield AL10 9AB, UK
[6] Aix Marseille Univ., CNRS, CNES, LAM, 13388 Marseille Cedex 13, France
[7] Argelander-Institut für Astronomie (AIfA), Universität Bonn, Auf dem Hügel 71, 53121 Bonn, Germany
[8] Ruhr University Bochum, Faculty of Physics and Astronomy, Astronomical Institute (AIRUB), Universitätsstrasse 150, 44801 Bochum, Germany
[9] Max Planck Institute for Extraterrestrial Physics, Giessenbachstrasse 1, 85748 Garching, Germany
[10] Astronomical Observatory, Jagiellonian University, ul. Orla 171, 30-244 Kraków, Poland
[11] INAF – Astronomical Observatory of Padova, vicolo dell'Osservatorio 5, 35122 Padova, Italy

ABSTRACT

Context. The Virgo cluster is the nearest ($d = 16.5$ Mpc) massive ($M \geq 10^{14}\,M_\odot$) galaxy cluster and is therefore a prime target for studying astrophysical processes in dense large-scale environments. In the radio band, we can probe the nonthermal components of the interstellar medium, the intracluster medium (ICM), and of active galactic nuclei (AGN). This allows an investigation of the impact of the environment on the evolution of galaxies and the contribution of AGN to ICM heating. With the ViCTORIA (VIrgo Cluster multi-Telescope Observations in Radio of Interacting galaxies and AGN) project, we are carrying out multiple wide-field surveys of the Virgo cluster at different frequencies.
Aims. We aim to investigate the impact of the environment on the evolution of galaxies and the contribution of AGN to ICM heating – from the inner cluster regions out to beyond the virial radius.
Methods. We performed a survey of the cluster at $120-168$ MHz using the LOw-Frequency ARray (LOFAR). We imaged a 132 deg^2 region of the cluster, reaching an order-of-magnitude greater sensitivity than existing wide-field radio surveys of this field at three times higher spatial resolution compared to other low-frequency observations. We developed a tailored data processing strategy to subtract the bright central radio galaxy M 87 from the data. This allowed us to correct for systematic effects due to ionospheric variation as a function of time and direction.
Results. In the final mosaic, which has a resolution of $9'' \times 5''$, we reach a median noise level of 140 μJy beam^{-1} inside the virial radius and 280 μJy beam^{-1} for the full area. We detect 112 Virgo member galaxies and 114 background galaxies. In at least 18 cases, the radio morphology of the cluster member galaxies shows clear signs of ram-pressure stripping. This includes three previously unreported candidates. In addition, we reveal previously undiscovered tails of 150 kpc in length from a previous epoch of AGN activity for NGC 4472 (M 49). While no cluster-scale diffuse radio sources are discovered, we find the presence of an extended radio signature of the W' group. This feature is coincident with an X-ray filament detected with SRG/eROSITA in the outskirts of the cluster. We speculate that this emission is synchrotron radiation, which could be related to shocks or turbulence from accretion processes.
Conclusions. The data published in this paper serve as a valuable resource for future studies. In the follow-up work of the ViCTORIA project, we will use these data for an analysis of environmental effects on the radio properties of star-forming galaxies in Virgo.

Key words. galaxies: clusters: individual: Virgo Cluster – radio continuum: general – surveys – catalogs

1. Introduction

The Virgo cluster, referred to hereafter as "Virgo", is the nearest galaxy cluster to us; its center is coincident with the bright radio galaxy M 87 (Virgo A, NGC 4486, e.g., Owen et al. 2000; de Gasperin et al. 2012) at a distance of 16.5 Mpc (Gavazzi et al. 1998; Mei et al. 2007; Cantiello et al. 2018). Due to its proximity, the cluster spans an enormous angular size with a virial radius of 3.3° (974 kpc), (Simionescu et al. 2017). Estimates of the virial mass $M_{\rm vir}$ ($\approx M_{200}$) of the cluster span the range of $M_{\rm vir} \approx 1.0-1.4 \times 10^{14} M_\odot$ (Urban et al. 2011; Ferrarese et al. 2012; Simionescu et al. 2017). The system is considered to be dynamically young and in the process of formation, as indicated by the high fraction of spiral galaxies, the significant deviation from spherical symmetry (Binggeli et al. 1987), and the properties of the intracluster stars (Aguerri et al. 2005; Arnaboldi et al. 2005). A further indication of the young age of the cluster is the presence of pronounced substructure in the galaxy distribution as well as in the X-rays, such as the subclusters and subgroups

---

associated with the massive ellipticals M 49, M 60, and M 86 (Böhringer et al. 1994). All of these features mean that Virgo is an exceptional target for studies of the evolution of clusters and their member galaxies.

An example of a phenomenon that can be studied in rich and dynamic environments such as Virgo is ram-pressure stripping, a perturbation that affects galaxies that move at high velocity with respect to the intracluster medium (ICM). This effect removes part of the interstellar medium (ISM) of star-forming galaxies, eventually causing a quenching of star formation, whereafter they are referred to as quiescent (e.g., Gunn & Gott 1972; Sarazin 1986; Boselli et al. 2022). The synchrotron-emitting cosmic rays in the ISM of star-forming galaxies are accelerated in the supernovae of short-lived massive stars, which gives rise to the particularly tight radio–SFR relation (van der Kruit et al. 1971, 1973; Calistro Rivera et al. 2017; Gürkan et al. 2018). For galaxies that experience ram-pressure stripping, an excess of radio emission can often be found (Gavazzi et al. 1991; Gavazzi & Boselli 1999; Miller & Owen 2001; Murphy et al. 2009; Ignesti et al. 2022a). Integrated flux density measurements and high-resolution studies of individual cluster galaxies can help us to understand the cause of this excess. Cosmic-ray electrons in the stripped ISM of galaxies likely show a steep spectrum due to radiative aging. Low-frequency ($\lesssim 1$ GHz) observations are required to detect the oldest and most distant parts of those stripped tails. Indeed, a number of studies utilizing 144 MHz observations with the Low-Frequency Array High-band Antenna (LOFAR HBA) recently demonstrated that low-frequency observations are well suited to discover ram-pressure-stripped tails (Ignesti et al. 2022b,a; Roberts et al. 2021a,b, 2022b).

Contrary to star-forming galaxies, where the radio luminosity is dominated by the aforementioned star formation, in early-type galaxies, active galactic nuclei (AGN) are responsible for the radio emission. The relativistic plasma supplied by AGN can halt the star formation of the host galaxy (Gaspari et al. 2012) and in clusters it can even influence the thermodynamical properties of the ICM via AGN feedback (Fabian 2012). For Virgo, interactions between the AGN jets and the surrounding ICM have previously been observed for M 87 (Forman et al. 2007; Million et al. 2010) as well as for numerous other systems at the centers of the less massive substructures (Kraft et al. 2011; Dunn et al. 2010; Paggi et al. 2014; Su et al. 2019) or in noncentral galaxies (Finoguenov et al. 2008; Bîrzan et al. 2008; Kraft et al. 2011; Million et al. 2010; Paggi et al. 2014; Su et al. 2019). As the relativistic electrons accelerated by the AGN lose energy over time, their radio spectrum also becomes steeper. Therefore, observations at low frequencies are required in order to unveil the emission of past phases of nuclear activity.

Furthermore, in the radio band, the nonthermal component of the ICM can generate radio halos and radio relics if there is sufficient particle acceleration and magnetic field strength (Brunetti & Jones 2014; van Weeren et al. 2019). Such emission is prominent in nearby clusters like Coma and Abell 1367. Contrary to these clusters of higher richness, Virgo is not known to host cluster-scale diffuse radio emission. Nevertheless, deeper observations may provide the means to reveal (or put stringent limits on) the presence of such a source, which could possibly be linked to merging subsystems. Again, observations at low frequency are critical because of the steep-spectrum nature of diffuse radio sources. This is the case for Virgo in particular, given that clusters of lower mass are expected to host steeper radio halos (Cassano 2010).

Until now, the most sensitive wide-field surveys that cover Virgo are the TIFR GMRT Sky-Survey (TGSS, Intema et al.

2017), the NRAO VLA Sky Survey (NVSS, Condon et al. 1998), and, more recently, the Rapid ASKAP Continuum Sky Survey (RACS, McConnell et al. 2020) and the *Karl G. Jansky* Very Large Array Sky Survey (Lacy et al. 2020). All of these are subject to strong imaging and calibration artifacts in proximity to M 87, and only TGSS is a low-frequency survey, at 150 MHz. In addition to the wide-field surveys, there have been a number of radio studies of samples of Virgo galaxies (Vollmer et al. 2007, 2010, 2013; Weżgowiec et al. 2007, 2012; Murphy et al. 2009; Capetti et al. 2009). However, those are limited to a small number of objects (<20).

We aim to significantly increase the radio coverage of Virgo with the ViCTORIA (Virgo Cluster multi-Telescope Observations in Radio of Interacting galaxies and AGN) project. The project includes data from the low- and high-band systems of LOFAR as well as MeerKAT and will greatly improve the sensitivity and resolution of the wide-field coverage in radio continuum between 42 and 1700 MHz and in the 21 cm line. Polarization data from the *L*-band observations will also be included. This work represents the first data release of ViCTORIA, and presents data taken with the LOFAR HBA at 144 MHz. LOFAR (van Haarlem et al. 2013) is a radio interferometer based in the Netherlands and operating at frequencies of between 10 and 240 MHz. The LOFAR Surveys Key Science Project is currently carrying out the LOFAR Two-metre Sky Survey (LoTSS, Shimwell et al. 2017, 2019, 2022), imaging the Northern Sky at more than an order of magnitude greater sensitivity and significantly higher resolution than previous large sky surveys. Due to its low declination and the presence of the extremely bright source M 87 (1250 Jy at 144 MHz), which severely complicates calibration and imaging of the field, Virgo is not yet included in the published footprint of LoTSS. With this work, we take advantage of significant advances in low-frequency radio interferometric calibration techniques developed for LoTSS (Tasse et al. 2021) to extend the coverage of sensitive LOFAR surveys to the Virgo region by employing a partly custom-developed calibration strategy to address the severe image fidelity issues associated with M 87.

A wealth of multiwavelength data exists on Virgo, which is complemented by the LOFAR observations presented in this paper and the further releases of the ViCTORIA project. For example, the classical reference for galaxies in the Virgo field is Binggeli et al. (1985), who carried out optical observations and published the photographic Virgo Cluster Catalog (VCC), which includes 2096 galaxies in an area of 140 deg^2. A digital successor to the VCC is the Extended Virgo Cluster Catalog (EVCC), (Kim et al. 2014), which is based on SDSS Data Release 7 photometric and spectroscopic data (Abazajian et al. 2009) and provides an updated cluster membership and morphology categorization of galaxies residing in a five times larger area than the VCC. The deepest optical survey of the cluster is the Next Generation Virgo Cluster Survey (NGVS, Ferrarese et al. 2012) conducted with the MegaCam instrument at the CFHT. Other auxiliary data include the Virgo Environmental Survey Tracing Ionised Gas Emission (VESTIGE, Boselli et al. 2018b), which mapped the cluster in Hα + [NII] also using MegaCam and following the NGVS footprint. In the far-infrared, data of the *Herschel* Reference Survey (HRS, Boselli et al. 2010) and the *Herschel* Virgo Cluster Survey (HeViCS, Davies et al. 2010) exists. In the near- and far-ultraviolet, the cluster was observed by the GALEX Ultraviolet Virgo Cluster Survey (GUViCS, Boselli et al. 2011). Combined, these data give an outstanding repertoire of star-formation tracers over the entire cluster region. Other data include the sample from the ACS Virgo Cluster Survey

(ACSVCS, Cote et al. 2004) of 100 early-type Virgo galaxies. In infrared and X-rays, this sample has also been studied with *Spitzer* and *Chandra* (Gallo et al. 2010). Samples of late-type galaxies were the subject of dedicated studies with *Chandra* in X-rays (Soria et al. 2022), ALMA in molecular gas (Brown et al. 2021) and with the VLA in atomic gas (HI, Chung et al. 2009). The properties of the ICM were analyzed based on X-ray observations with ROSAT (Böhringer et al. 1994), *XMM-Newton* (Urban et al. 2011), and Suzaku (Simionescu et al. 2017). An study beyond the virial radius is currently being conducted with the extended ROentgen Survey with an Imaging Telescope Array (eROSITA, (Merloni et al. 2012; Predehl et al. 2021; McCall et al., in prep.).

With this paper, we extend the multiwavelength coverage of Virgo by providing wide-field images of the cluster and radio measurements of all LOFAR-detected Virgo galaxies. A detailed scientific interpretation of the radio data will follow in upcoming publications, where we will analyze the environmental impact on galaxy evolution and the radio galaxy population in the Virgo cluster.

Throughout this paper, we assume a flat ΛCDM cosmology with $\Omega_{\rm m} = 0.3$ and $H_0 = 70\,{\rm km\,s^{-1}\,Mpc^{-1}}$. At the distance of M 87, for which we adopt a value of 16.5 Mpc (Mei et al. 2007; Cantiello et al. 2018), one arcsecond corresponds to 80 pc. This paper is arranged as follows: in Sect. 2, we present the observations and the data reduction strategy of the survey. In Sect. 3, we report details of the catalog of Virgo galaxies we provide, and in Sect. 4, we highlight individual objects and findings in the LOFAR maps. We conclude in Sect. 5.

2. Observations and data reduction

The LOFAR HBA Virgo Cluster Survey covers a 132 deg² region of the Virgo cluster between a declination of 3° and 18°. The survey footprint displayed in Fig. 1 is composed of the nine different pointings listed in Table 1. In total, eight observations of 8 h each were conducted (project: LC11_010) between March 18, 2019, and April 2, 2019, book-ended by 10 min calibrator scans of 3C 196 and 3C 295. The observations were taken in dual-beam mode, with one beam always pointing toward M 87, and the other toward one of the eight outer fields. The outer fields lie on the grid of LoTSS. The total observation time of M 87 is only 56 h rather than 64 h because the observation parallel to field 1 is missing in the LOFAR Long-Term Archive (LTA). Data were taken with the LOFAR HBA in a setup identical to observations taken for LoTSS with a nearly continuous frequency range from 120 to 168 MHz, a frequency resolution of 3.07 kHz, and a time resolution of 1 s. After initial flagging of the raw data, the data are averaged to a resolution of 12.2 kHz in frequency and stored in the LTA.

2.1. Challenges of the Virgo field

The presence of M 87 in the cluster center makes radio calibration and imaging of the Virgo field particularly challenging. It is not only one of the brightest sources on the radio sky (1.25 kJy at 144 MHz, Scaife & Heald 2012), but is also highly extended with an angular size of 15′. This complex morphology makes an accurate deconvolution of the source hard to achieve, and the large extent means that the primary beam variation across M 87 is non-negligible; indeed it is >20% for some pointings. Another difference in comparison to observations of LoTSS-DR2 is the declination of the LOFAR Virgo field, which is between +3°

and +18°; this translates to rather low-elevation observations in the range of ~25°–50° (see Fig. 2). This causes an elongated primary beam shape, an increased thermal noise level due to the reduced sensitivity of the dipoles, and greater susceptibility to ionospheric disturbances caused by the higher air mass compared to observations at more favorable declinations. Furthermore, the LOFAR primary beam model is expected to be less accurate at lower elevations, which affects the accuracy of the flux density scale. Finally, the majority of the Virgo cluster galaxies are extended objects with a low radio-continuum surface brightness and as such, are difficult to fully deconvolve.

2.2. Data reduction

To address the aforementioned difficulties, we developed a strategy specifically tailored to the Virgo cluster field and the targets of interest. The main difference from the default calibration approach for LOFAR HBA, which is used, for example, for LoTSS-DR2, is an additional step in which we accurately subtract M 87 from the *uv*-data. Subsequently, direction-dependent calibration can mostly be carried out in a similar way to LOFAR HBA observations of normal fields.

The data reduction is split into a series of steps, which are implemented in various pipelines: The first step is preprocessing, the second is to reduce the data of the calibrator scans, the third is to subtract M 87 from the data, and the last step is a full direction-dependent calibration. Subsequently, an extraction and re-calibration procedure can be applied for selected targets (see van Weeren et al. 2021). For the first three steps, we make use of the Library for Low Frequencies (LiLF[1]), and for the direction-dependent calibration and extraction, we use the ddf-pipeline[2] (Tasse et al. 2021).

In the pre-processing step, the data of all calibrator and target observations were downloaded from the LTA. Subsequently, all baselines containing international LOFAR stations were removed and the data were averaged down to 48.8 kHz in frequency (four channels per sub-band) and 4 s in time. The strategy used to find the calibrator solutions is described in detail in de Gasperin et al. (2019); nevertheless, we briefly summarize the key steps below. The pipeline derived the polarization alignment delays as well as the Faraday rotation and bandpass solutions. These were then applied to the data in physical order together with the primary beam model. Finally, we solved for scalar phases, which describe the ionospheric and clock delays.

2.2.1. Peeling pipeline

The purpose of this pipeline is to subtract M 87 from the *uv*-data of each observation of the Virgo field. A key requirement for this is a high-quality model of the source, which did not exist at 144 MHz prior to this project. Starting from the $21'' \times 15''$ image of de Gasperin et al. (2012), we performed multiple rounds of self-calibration using an 8 h observation with M 87 at the phase center. In each iteration, we solved for scalar phases at full time- and frequency resolution and for full-Jones matrices at a resolution of 64 s and 0.49 MHz using DP3[3]. For imaging, we used the multi-scale and multi-frequency deconvolution mode of WSCLEAN (Offringa et al. 2014; Offringa & Smirnov 2016). As M 87 is extremely bright, highly resolved, and of complex morphology, deconvolution is particularly delicate. With improving

---

[1] https://github.com/revoltek/LiLF
[2] https://github.com/mhardcastle/ddf-pipeline
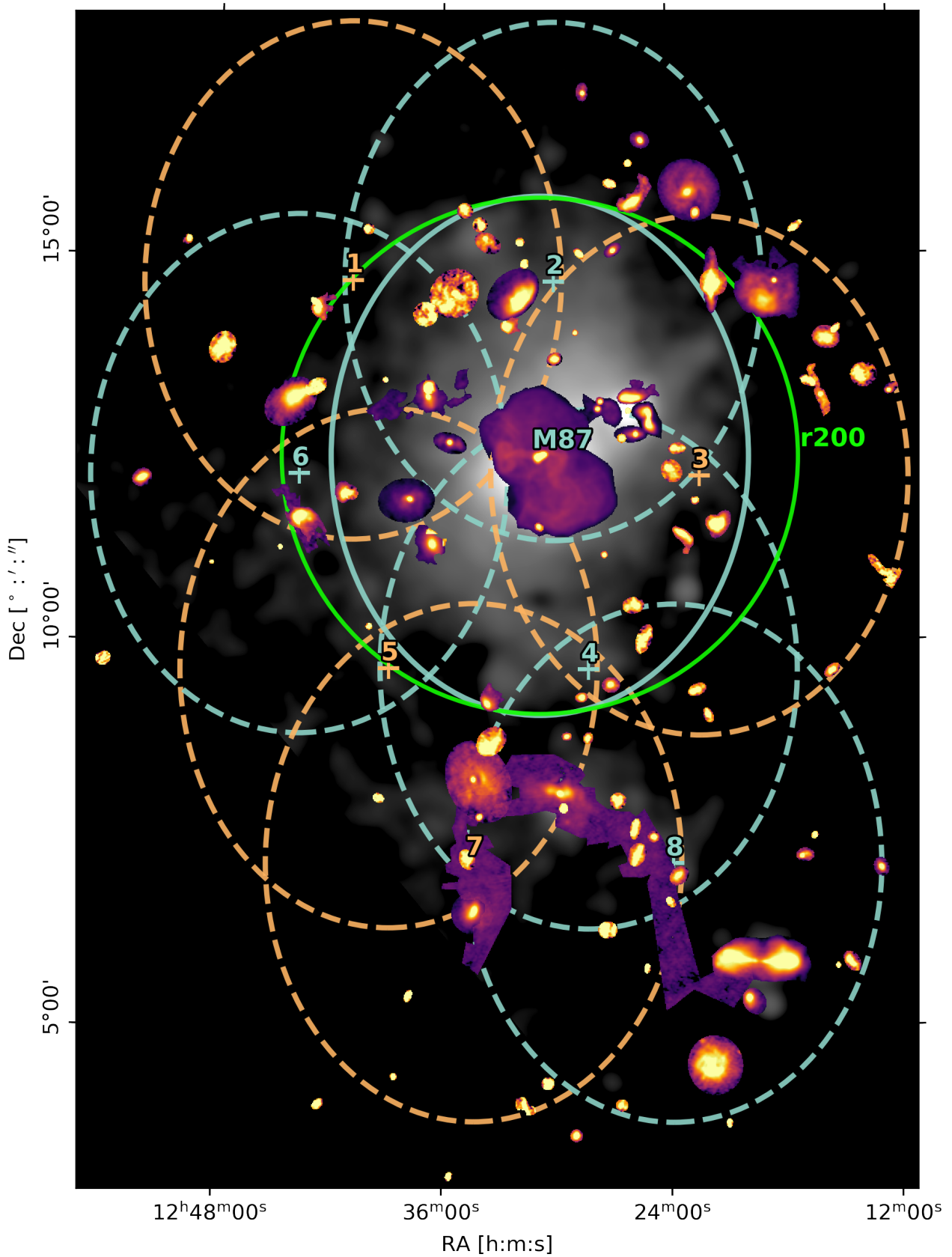[3] https://github.com/lofar-astron/DP3

Fig. 1. Overview of the LOFAR HBA Virgo cluster survey. As cutouts, we show the radio-detected galaxies from the 20″ mosaic; for better visualization, their sizes are magnified by a factor of six and their color mappings adjusted individually. The central points and the half-maximum primary beam ellipses of the nine survey pointings are displayed in alternating colors (orange/blue). The green circle marks r_{200} and the grayscale background image is the eROSITA X-ray map in the $0.3-2$ keV band (McCall et al., in prep.) where we mask the southeastern emission in the direction of the NPS.

Table 1. Virgo cluster pointings.

Field	RA (J2000) [h:m:s]	Dec (J2000) [°:′ :″]	Observation time [h]	Comments
M87	12:30:49.42	+12:23:28.0	56	
1	12:40:47.46	+14:39:45.5	8	Severe ionosphere, high noise level
2	12:30:05.30	+14:38:54.9	8	
3	12:22:22.72	+12:07:42.3	8	
4	12:28:16.58	+09:37:33.7	8	
5	12:38:46.71	+09:38:23.2	8	
6	12:43:33.66	+12:09:22.3	8	Dynamic ionosphere
7	12:34:18.36	+07:07:25.6	8	Bright sources
8	12:23:52.29	+07:06:36.4	8	Bright sources
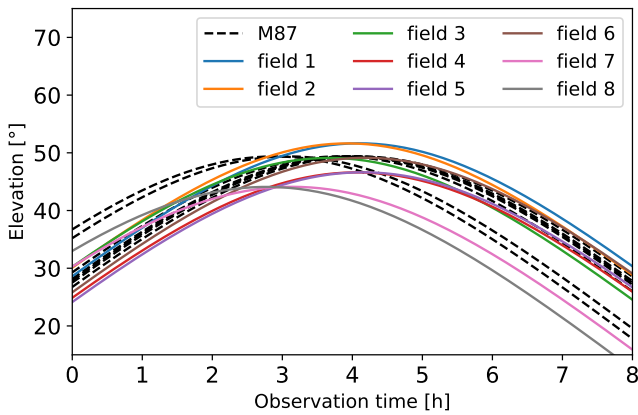
Fig. 2. Elevation as a function of observation time for the Virgo cluster observations.
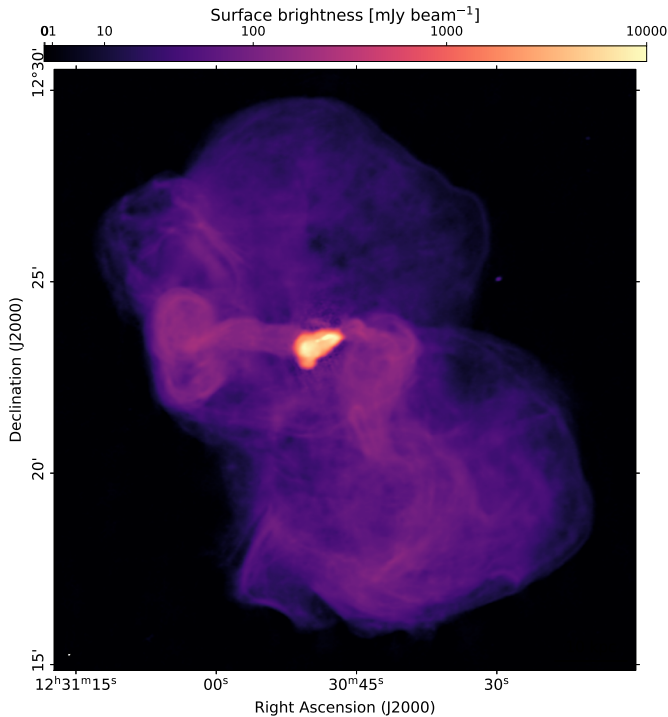
Fig. 3. LOFAR image of M 87 at 144 MHz. The ellipse in the bottom left corner indicates the primary beam size of $5.6'' \times 4.1''$. The noise level is 350 µJy beam^{-1}, corresponding to a dynamic range of 44 000.

8 h observation was created using a *Briggs*-value of -1.2 – shown in Fig. 3 – and the final model of M 87 used for the peeling is created with a *Briggs*-weighting of -0.6.

The following peeling procedure was carried out for each observation. The first step of the peeling pipeline is to apply the polarization alignment, bandpass, and scalar-phase solutions from the calibrator together with the primary beam model at the phase center to the target field. Here, we used the corresponding calibrator observation with the least amount of flagged data. Next, we perform 'A-Team clipping'. The purpose of this procedure is to flag the parts of the data where the bright sources Cassiopeia A, Cygnus A, and Taurus A (which form the infamous "A-team" together with "Virgo A") reside in a side-lobe of the primary beam. If their predicted amplitude is above 5 Jy for any time, frequency, or polarization, this part of the data is flagged. In addition, we flag the parts of the data affected by radio-frequency interference using AOFLAGGER (Offringa et al. 2012) as well as all data taken below 20° elevation. Afterwards, time steps that contain more than 50% flagged data are discarded.

Next, the data are phase-shifted toward the location of M 87, that is, if they are not already centered on the source, and are corrected for the difference between the primary beam at the original phase center and M 87. From this phase-shifted data set, a smaller data set is created by averaging down to a resolution of 16 s in time and 0.39 MHz in frequency. This speeds up computation and suppresses the contribution of sources away from M 87 by time- and frequency-smearing them. The model-*uv*-data of this small data set is populated with the M 87 source model using WSCLEAN together with the image domain gridder (idg, van der Tol et al. 2019). Due to a large angular size of $15'$, the primary beam variations across M 87 are non-negligible, especially for the pointings where M 87 is close to the edge of the primary beam. Therefore, we find that it is important to adjust the predicted visibilities with the direction-dependent component of the primary beam during prediction. Then, complex scalar gain solutions are derived by solving against the model data on the full time resolution of the averaged data set. In the solver, the solutions are smoothed in frequency with a 1 MHz kernel. From the resulting calibration solutions, we only apply those phases to the data that encompass the ionospheric delays. However, the amplitudes are used to identify bad parts of the data by flagging all time and frequency intervals where the amplitudes are more than a factor of five from unity. We perform a second, slow full-Jones calibration on timescales of 256 s. In this solve step, we smooth the calibration solutions with a 2 MHz kernel in frequency. After deriving the solutions towards M 87 from the small data set, we predict the *uv*-data corresponding to the M 87 model to the large data set at 48.8 kHz bandwidth and 4 s time resolution, again
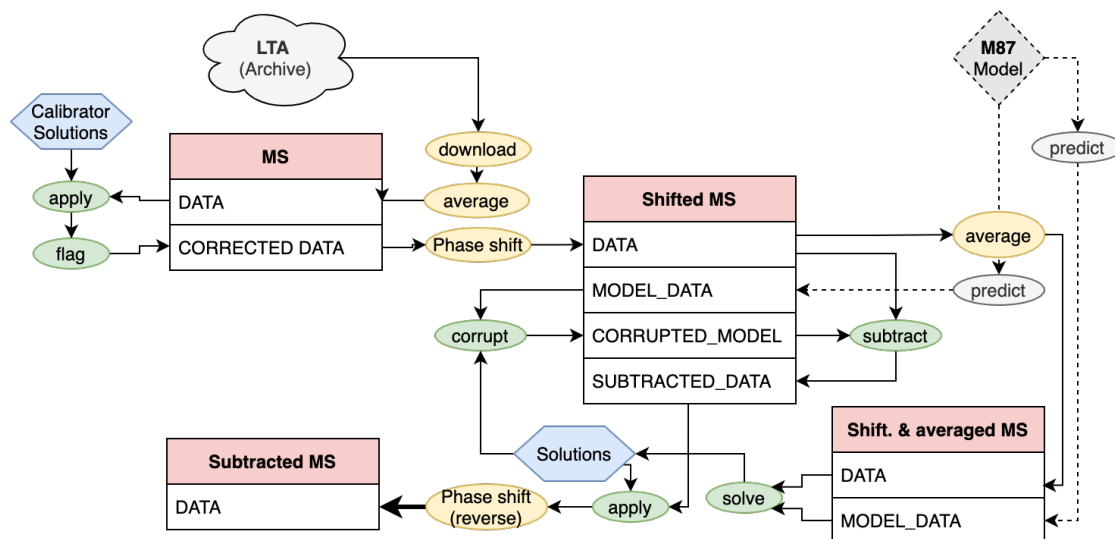
solutions during self-calibration, less conservative deconvolution parameters can be used. A high-resolution image of a single

Fig. 4. Scheme of the peeling strategy.

using `idg` to include the direction-dependent component of the primary beam. The predicted visibilities are then corrupted with the phase and slow full-Jones solutions. We create a new data set by subtracting the corrupted M 87 model from the data. We then correct the subtracted data using the scalar phases towards M 87, which is intended to correct the clock delays as well as to pre-correct the ionospheric delays in the direction of Virgo. The pre-corrected subtracted data column is then phase-shifted back to the original phase center, averaged to a resolution of 8 s in time and 98 kHz in frequency, and is concatenated into frequency blocks of 1.95 MHz. Finally, we correct for the difference of the primary beam at the phase center and at the location of M 87. The resulting measurement sets now have M 87 subtracted and are therefore prepared in a format that is suitable for the following direction-dependent calibration. A schematic overview of the peeling strategy is presented in Fig. 4.

For the observations centered on M 87, the subtraction procedure was slightly altered. The phase-shifting and additional beam-correction steps are not necessary due to the greater apparent brightness. Furthermore, the calibration solutions are derived at a higher time resolution of 4 s for the Jones scalar, and 64 s for the full-Jones matrix.

For field 8, the subtraction of M 87 is particularly challenging due to the presence of NGC 4261 (=3C 270; S_{144} = 73 Jy) in the center of the field. To obtain robust solutions for this pointing, we used a parallel solve on both NGC 4261 and M 87, where we employed a model of two Gaussian components obtained from the TGSS for NGC 4261. In addition, we solved for a diagonal instead of a full-Jones matrix and used a 4 MHz kernel to smooth the solutions in frequency to reduce the effective number of free parameters. The solutions for M 87 were used for subtraction and to pre-calibrate the phases; the solutions for NGC 4261 were discarded. Stable calibration solutions were not obtained for all time- and frequency windows, which lead to a high ratio of flagged data for this field (55%).

2.2.2. Direction-dependent calibration

For direction-dependent calibration, the `ddf-pipeline` (Shimwell et al. 2019; Tasse et al. 2021) is used, which is a framework that is based on the `DDFacet` imager (Tasse et al. 2018) and the `killMS` solver (Tasse 2014a,b). The `ddf-pipeline`

algorithm was also used for the second data release of LoTSS. As it is described in detail in Tasse et al. (2021), only a very brief summary is provided here, mainly focusing on the differences in processing compared to LoTSS-DR2. The algorithm starts with a sparse selection of the data, taking every fourth frequency sub-band. In a series of direction-independent and direction-dependent calibration steps, a sky model of a $8.3° \times 8.3°$ square region of the target field is obtained. Using this model, calibration is carried out on all sub-bands, again in a series of direction-independent and direction-dependent self-calibration cycles. The direction-dependent steps are carried out in a facet-based approach; that is, the sky model is split into 45 discrete directions, which are solved in parallel. An important difference from the LoTSS-calibration is that no amplitude solutions are applied to the data; this is because we experienced divergent amplitude solutions in a small number of facets with a low flux density. This divergence is likely caused by the reduced quality of the data because of residuals of M 87 and/or a low signal-to-noise ratio due to the low elevation of the observations. As a consequence of the missing amplitude corrections, artifacts exist around a number of bright sources, mainly further away from the phase center, suggesting that they may be at least partly caused by errors in the primary beam model. However, this does not notably affect the science quality of the images regarding studies of Virgo cluster objects, because the vast majority of these sources are of low-surface brightness. During the various imaging steps, it is challenging but also critical to accurately deconvolve faint and extended structures in order to obtain a complete sky model for calibration and accurate surface brightness values. The `ddf-pipeline` strongly optimizes deconvolution for these targets using multiple `CLEAN` iterations with progressively improved masks. Using a mask based on lower resolution images for the deep high-resolution deconvolution, it is possible to further improve deconvolution for extended structures. Nevertheless, a number of faint Virgo galaxies are not fully picked up in the masking procedure and are therefore not accurately deconvolved. To address this, we manually add all detected galaxies of the optical VCC and EVCC catalogs to the masks created by the `ddf-pipeline` and perform one additional deep `CLEAN` iteration for both the low- and high-resolution images. For the seven observations pointed on M 87, we follow the procedure used for the LoTSS deep fields

(Tasse et al. 2021). A single 8 h observation is fully calibrated to derive an accurate sky model. This model is then used to jointly calibrate and deconvolve all 56 h of data.

For three of the eight outer fields, a slightly different strategy was necessary: field 6 is affected by the presence of 3C 275.1 outside of the 8.3° square region used for imaging and calibration. We address this by carrying out an additional initial imaging step with a larger field of view (FoV) to subtract sources outside of the square normally used for calibration. Calibration of the two southern pointings on fields 7 and 8 is particularly challenging, as they have a bright source in the FoV (NGC 4261), and the bright quasar 3C 273 (116 Jy, Jacobs et al. 2011) in the side-lobes. The subtraction of sources outside the primary beam, which was used for field 6, did not yield satisfactory results for fields 7 and 8. Instead, the image size used for direction-dependent calibration of these two fields was increased to allow for direction-dependent solutions towards 3C 273. As this strongly increased memory requirements and computation time, the data set was phase-shifted beforehand such that the image size is only increased so as to cover 3C 270, without increasing the coverage in the opposite direction. The size of the square region used for calibration of fields 7 and 8 is 9.5°.

Per field, a number of wide-field imaging products are created from the calibrated data sets: We image Stokes I at angular resolutions of $9'' \times 5''$, $20''$, and $1'$; hereafter, we refer to these resolutions as high, low, and very low. Compact source-subtracted images were created at $1'$ and $4'$ resolution. In addition, we produced Stokes Q and U "dirty" images in a frequency spacing of 97.6 kHz at $20''$ and $4'$ resolution and Stokes V dirty images at $20''$ resolution. No flux-density-scale correction was applied to the per-field data products.

2.2.3. Flux-scale alignment and mosaicing

Uncertainties on the beam model of LOFAR HBA currently limit the accuracy of the flux density scale when it is directly transferred from a calibrator source by introducing a per-field flux density scaling $f_i \neq 1$. Therefore, Shimwell et al. (2022) correct the flux density scale in a post-processing step. By cross-matching sources between LOFAR and the 151 MHz sixth Cambridge survey of radio sources (6C Hales et al. 1988) and between LOFAR and the 1.4 GHz NVSS, these latter authors derive the median flux density ratios $F_{6C,i}$ and $F_{NVSS,i}$ of each field i and both surveys. Under the assumption that the flux-density-scale offsets are direction-independent for a given field, both median ratios should be equally offset by a factor of f_i from the value found for a perfectly accurate flux density scale. Therefore, the ratio of the median flux density ratios per field $F_{6C,i}/F_{NVSS,i}$ should be approximately independent of the offset f_i and also therefore constant between the fields if there is no spatial variation in the NVSS and 6C scales. Considering the median of the median ratios found across all fields, a value of $F_{6C}/F_{NVSS} = 5.724$ was found in Shimwell et al. (2022). Taking into account the frequency difference between LOFAR and 6C, and using the median spectral index of sources in 6C and NVSS of $\alpha = -0.783$, the LOFAR observations are aligned with the 6C flux density scale if the median flux density ratio equals $F_{NVSS} = 5.724 \times (144/151)^{-0.783} = 5.936$. Consequently, the flux-density-scale correction factors f_i^{-1} can be determined from the measured median flux-density-scale ratio $F_{NVSS,i}$ of each field as $f_i^{-1} = 5.936/F_{NVSS,i}$. We followed the procedure developed in Shimwell et al. (2022) with two minor modifications: First, as a flux cut of 30 mJy is applied in the cross-matching
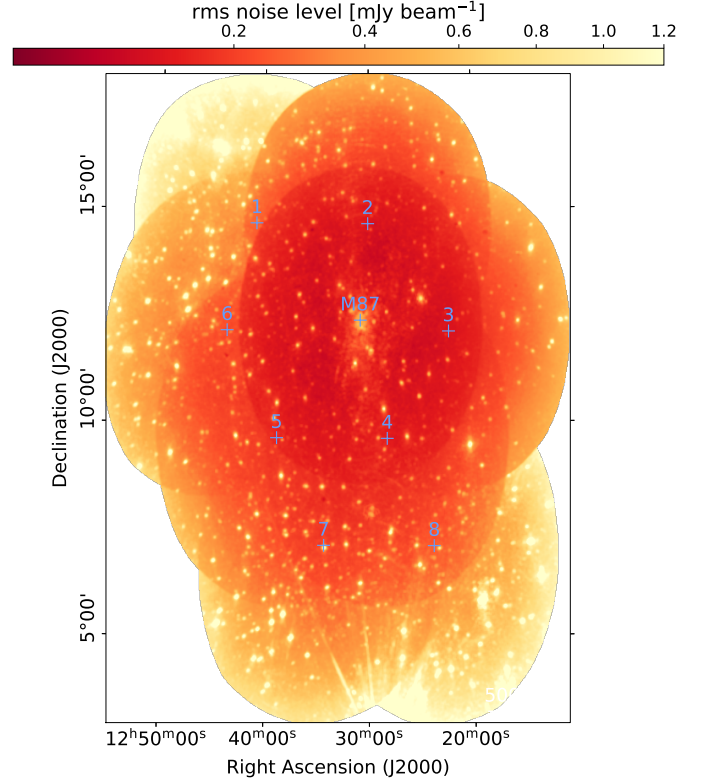
Fig. 5. RMS noise map of the $9'' \times 5''$ mosaic. Blue annotations indicate the pointing centers of the nine LOFAR fields.

with NVSS prior to the re-scaling, and given that we found correction factors strongly different from unity for some fields, we iteratively repeated the calculation of the correction factors f_i, updating the flux cut to $30\,\text{mJy} \times f_i^{-1}$ each time. Second, we estimated the correction factors from the $20''$-resolution maps, because in the high-resolution maps, ionospheric smearing leads to a systematic over-correction of 10–20% for the fields where we have lower quality (fields 1, 6, 7, 8). For the remaining fields with good image quality, the difference between the correction factors estimated from the high- and low-resolution maps is between 1 and 8%. To derive these factors, we created a LOFAR source catalog for each Virgo field using the Python Blob Detector and Source Finder (PyBDSF, Mohan et al. 2015) and only considered sources with: no neighbor within $30''$; a major axis of less than $25''$; and a significance of at least 5σ. The final correction factors we found were applied to the fields during mosaicing, ultimately placing our survey on the scale of the 6C survey, which in turn is aligned with the flux density scale of Roger et al. (1973). In the mosaicing procedure, pixels were weighted according to the primary beam response as well as the central noise level of the corresponding field. We also excluded all areas with a primary beam attenuation factor of below 0.3. In the final mosaic, we restore the clean components of M 87 that were subtracted in the peeling pipeline. Wide-field mosaics are created for the high-, low-, and very-low-resolution Stokes I maps as well as for the source-subtracted images. The image parameters of all Virgo field mosaics are presented in Table 2; the image files are available online in fits format[4].

A map of the root mean square (RMS) noise level of the high-resolution Stokes I mosaic is displayed in Fig. 5; the median noise level is $140\,\mu\text{Jy beam}^{-1}$ within the virial radius

---

[4] https://lofar-surveys.org

Table 2. Imaging parameters.

Resolution	Subtracted	['' × '']	Robust weighting	min. *uv* [km]	max. *uv* [km]
High		9×5	-0.5	0.1	120.6
Low		20×20	-0.25	0.1	25.8
Very low		60×60	-0.2	0.04	7.0
Very low	yes	60×60	-0.2	0.04	~ 7.0 (1′-taper)

and 280 μJy beam^{-1} across the full footprint. In the vicinity of M 87, the noise level is ~170 μJy beam^{-1}, only 40% deeper than what we find for a single 8 h observation, which indicates that we are limited by dynamic range in the central few square degrees. Beyond 2° separation from M 87, the sensitivity ratio between 8 h and 56 h of data approaches the expected ratio of $\sqrt{56\,h/8\,h} \approx 2.65$. Remaining artifacts related to M 87 manifest themselves as wave-like patterns, the most dominant of those originate from M 87 and cross the image towards the north and south, extending for multiple degrees. In some of the outer regions of the survey, the noise level is strongly increased. This is most apparent in the northeast, where the observation of field 1 was affected by particularly unfortunate ionospheric conditions with rapid high-amplitude variations of the ionospheric parameters. The noise level for the region that is exclusively covered by this pointing is ~800 μJy beam^{-1}. Fortunately, only very few Virgo cluster galaxies populate that area. Similarly, the eastern field 6 to the south of field 1 was also affected by a dynamic ionosphere, which increased the noise level to 250 μJy beam^{-1}. Another region where the image quality is reduced is the southwestern field 8, where the presence of the bright sources 3C 270 and 3C 273, as well as a high flag ratio and low elevation, increase the noise level to ~400 μJy beam^{-1}. In the lower-resolution mosaics in particular, this area also shows the presence of larger-scale calibration artifacts.

In Fig. 6, we compare the noise level of the LOFAR HBA Virgo cluster survey to that of other surveys and targeted observations of the Virgo field. The quoted noise level of ~150 μJy beam^{-1} corresponds to the region just inside the area covered by the deeper M 87 pointing, which approximately coincides with the Virgo cluster virial radius.

2.3. Flux density scale

For LoTSS-DR2, the global uncertainty of the flux density scale was estimated to be 10%, with an additional positional variation of 10% (Shimwell et al. 2022). For a number of reasons, we expect the uncertainty to be higher for the Virgo field: first, due to the low declination of Virgo, the LOFAR beam model should be less accurate, which translates to a higher systematic uncertainty on the flux densities. Indeed, Shimwell et al. (2022) found a declination dependency of the flux density scale that becomes increasingly severe at lower declination. Second, the presence of M 87 in the field not only causes image artifacts in our LOFAR data, but also – and even more severely – in the NVSS and other all-sky surveys, where no tailored strategy was used to address this bright source. This decreases the quality of reference radio catalogs within a few degrees around M 87. Finally, the direction-dependent variation of the flux density scale should be higher for simple statistical reasons; since our survey consists of only nine pointings, the degree of overlap is lower than in LoTSS, where the mosaicing of multiple pointings was shown to reduce the scatter of flux density measurements (Shimwell et al. 2022).
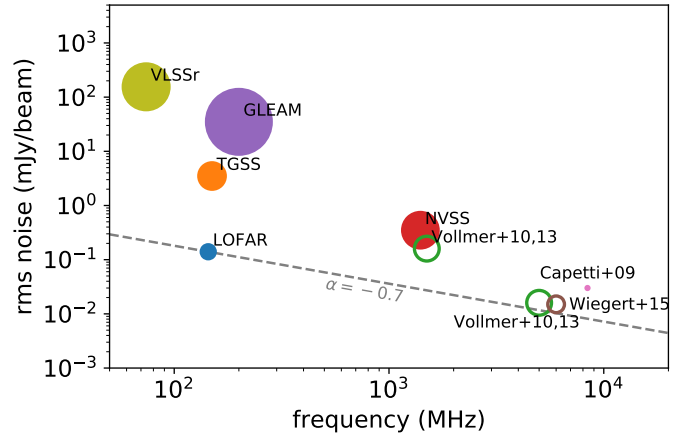
Fig. 6. Noise-level comparison of different Virgo cluster surveys. The circles show different wide-field surveys (filled circles) and targeted observations of samples of Virgo galaxies (hollow circles). The marker size is proportional to the angular resolution of the corresponding survey. The quoted noise level for LOFAR refers to the median noise inside the virial radius. The dashed line shows an interpolation of this noise level assuming a spectral index of -0.7.

To assess the systematic uncertainty of the flux density scale of the LOFAR HBA Virgo cluster survey, we created a source catalog of the final low-resolution mosaic using PyBDSF. We first compared the LOFAR catalog to NVSS, which was also used for the flux density scale alignment. Repeating the source selection and matching as described in Sect. 2.2.2, we find a median ratio of $S_{\mathrm{LOFAR}}/S_{\mathrm{NVSS}} = 5.42$, which differs by 9% from the value of 5.94 we used for the alignment.

We then cross-matched the LOFAR catalog with sources of the TGSS and the Galactic and extragalactic all-sky MWA survey (GLEAM Hurley-Walker et al. 2017), which are at almost the same frequency as LOFAR HBA. We searched for unique matches inside a radius of 10″ for TGSS and 50″ for GLEAM. To avoid complex sources, where the flux density measurements might not be accurate, we only kept the LOFAR sources that have no other source within 30″ for TGSS and within 2′ for GLEAM. Furthermore, we removed sources with an extension above 25″ or a signal-to-noise ratio below five. This resulted in 576 matched sources with TGSS and 68 with GLEAM. We extrapolated the TGSS 150 MHz flux densities to 144 MHz using a factor of $(144/150)^{-0.783} = 1.03$. For GLEAM, we used the 143 MHz catalog and neglected the frequency difference as well as the <3% systematic uncertainty arising due to the Baars flux density scale (Baars et al. 1977) of GLEAM (Hurley-Walker et al. 2017; Perley & Butler 2017). Compared to TGSS, the median flux scale ratio is 1.05 with a standard deviation of 0.23, and for GLEAM, it is 1.02 with a standard deviation of 0.19. This independent test shows that the flux density scale is aligned accurately, albeit with considerable scatter. This scatter is partly caused by the
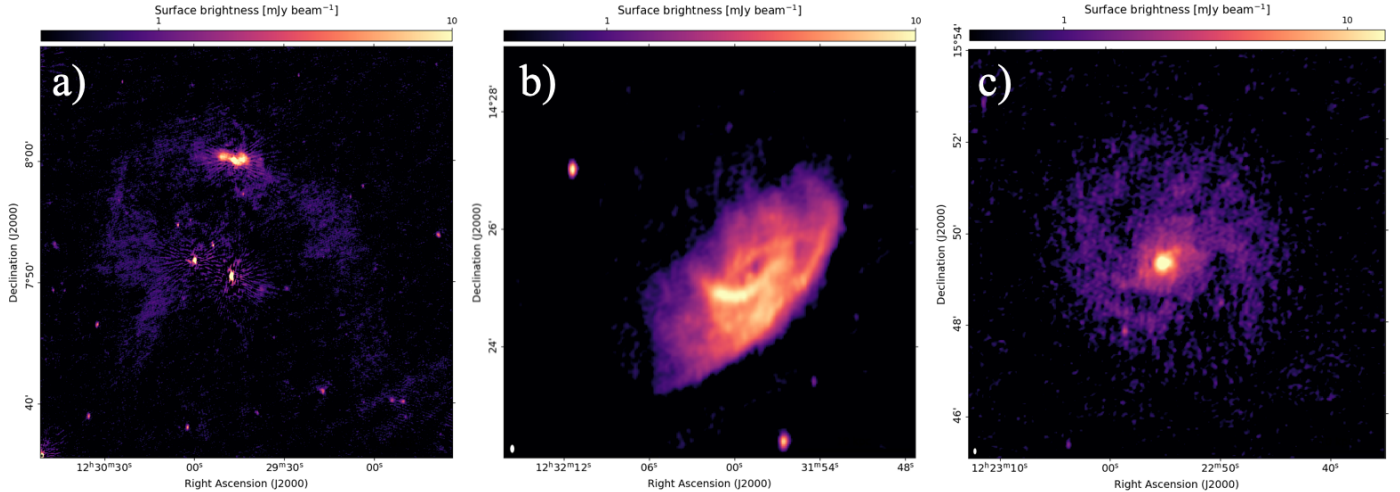
Fig. 7. LOFAR maps of selected Virgo cluster galaxies. The panels show (a) NGC 4472 (M 49), (b) NGC 4501 (M 88), and (c) NGC 4321 (M 100). The ellipse in the bottom left corner of the panels indicates the synthesized beam size of $9'' \times 5''$.

direction-dependent flux scale uncertainty in the LOFAR maps; another contribution stems from outliers in the cross-matching procedure. Additionally, the reference surveys also add considerably to the scatter. By cross-matching 211 sources in the Virgo field between TGSS and GLEAM, we find that the flux densities of those two surveys show a median flux ratio of 1.01 (expected: $(143/150)^{-0.78} = 1.04$) with a standard deviation of 0.29. Given the comparison with both TGSS and GLEAM, we assume that the systematic uncertainty on the flux density scale of our LOFAR HBA survey of the Virgo cluster is $f_{sys} = 20\%$, which includes both the uncertainty of the absolute flux density scale and the direction-dependent variation.

During the flux-scale alignment, we used the low-resolution mosaic, because it is less affected by poor ionospheric conditions. Indeed, repeating the procedure for the high-resolution images, we find that the median flux density is significantly lower for the observations with poor ionospheric conditions. The most extreme case is field 1, where the difference in median flux between the high-resolution and the low-resolution image is 28%. A significant difference of ~20% is also observed for the southern fields 7 and 8, where bright sources limit the quality of the calibration. This indicates that for regions close to the edge of the survey footprint, which are exclusively covered by one of those fields, particular care must be taken when working with the high-resolution images.

3. LOFAR Virgo cluster catalog

To create the catalog of all Virgo cluster galaxies that are detected in the 144 MHz LOFAR Virgo cluster survey, we considered all galaxies in the EVCC, which fully covers our LOFAR footprint. For the EVCC, a radial velocity cut of $v < 3000\,\mathrm{km\,s^{-1}}$ is employed to select possible cluster members, and a redshift-based infall model is used to identify certain cluster members (Kim et al. 2014). Of the 1589 galaxies, 991 are in the footprint of our LOFAR survey. The classical VCC includes a high number of background objects that do not fall into the radial velocity cut. As the VCC is still used as a common reference for galaxies in the Virgo field, we also compiled a radio catalog of the background VCC galaxies that are not part of the Virgo cluster.

As the radio continuum emission of the galaxies is mostly faint, extended, and often not well described by a Gaussian

profile (see Fig. 7), it is challenging to accurately identify all emission attributed to galaxies using an automatized source finder. We therefore measured the flux densities manually. We visually inspected the high- and low-resolution images of every galaxy in the EVCC and VCC with a z-band magnitude of 16 or below in the footprint of the LOFAR Virgo field. If emission is detected, we manually determine an elliptical region around the emission, if possible fully enclosing the 3σ contours in the low-resolution mosaic. In cases where the radio morphology is particularly complex or background sources are superimposed on the emission, we instead use a more complex polygon region to trace the emission. To check for misidentifications, the optical images of the DESI Legacy Imaging Survey DR9 (Dey et al. 2019) were inspected together with the radio contours.

We measure the integrated flux density in the regions, and the corresponding uncertainty σ_S is calculated according to:

$$\sigma_S = \sqrt{\sigma_{rms}^2 N_{beam} + \left(f_{sys} S\right)^2}, \qquad (1)$$

where $f_{sys} = 0.2$ is the systematic uncertainty of the flux density scale, N_{beam} the number of synthesized beams covering the region, and σ_{rms} the local statistical uncertainty as measured from the RMS of the residual maps. We only consider sources with a statistical significance above 4σ in the low-resolution mosaic. This results in 112 Virgo cluster galaxies that are detected in the LOFAR maps out of the 991 EVCC galaxies in the survey footprint. The detection fraction strongly depends on the optical brightness; it is above 50% for the 171 galaxies brighter than a z-band magnitude of 12. In contrast, none of the objects fainter than a z-band magnitude of 14.6 are radio-detected, although those constitute more than half of the EVCC objects in the LOFAR footprint. The optically bright objects that are not detected in LOFAR are mostly ellipticals and lenticulars without strong AGN. Additionally, we detect 114 background galaxies that are listed in the VCC.

As the galaxies are mostly low-surface-brightness extended sources, particular care must be taken during the deconvolution. If sources are not fully deconvolved, emission coming from the side-lobes of the point-spread function may remain and their flux density will be overestimated. This problem mostly affects the high-resolution mosaic, where the objects are more strongly resolved. To assess the completeness of the deconvolution, we

Table 3. LOFAR catalog of Virgo cluster galaxies.

VCC	NGC	IC	RA J2000 [h:m:s]	Dec J2000 [°:′:″]	Type	m_r [mag]	S [Jy]	A [″×″]	d [Mpc]	L_{144} [W Hz^{-1}]
(1)	(2)	(3)	(4)	(5)	(6)	(7)	(8)	(9)	(10)	(11)
49	4168		12:12:17.2	+13:12:19	E	11.00	(2.5±0.5)e-2	4291	32.0	(3.1±0.7)e+21
66	4178	3042	12:12:46.1	+10:51:55	SBc	11.24	(5.6±1.2)e-2	14149	16.5	(1.8±0.4)e+21
73	4180		12:13:03.0	+07:02:20	Sb	12.23	(1.6±0.3)e-1	7735	32.0	(2.0±0.4)e+22
89	4189	3050	12:13:47.4	+13:25:34	SBc	11.51	(9.0±1.8)e-2	17831	32.0	(1.1±0.2)e+22
120	4197		12:14:38.6	+05:48:23	Sc	12.65	(7.1±1.5)e-2	8902	32.0	(8.7±1.8)e+21

Notes. This table is available in its entirety at the CDS and contains the following information. The first three columns list the index of the galaxies in the VCC, NGC, and IC. Columns 4–7 list the optical coordinates, the morphological classification, and the r-band magnitude of the galaxies as in Kim et al. (2014). Column 8 shows the integrated flux density as measured from the 20″-resolution mosaics, Col. 9 quotes the source area, Col. 10 the distance, and Col. 11 the 144 MHz radio luminosity.

compare the flux densities of the sources in the high- and low-resolution images using identical regions. This comparison is presented in Fig. 8. Particularly for fainter sources, the flux density estimated from the high-resolution image is systematically above the measurement at low resolution, even after we perform an additional round of deep deconvolution with manual clean-masks for all objects in the catalog (see Sect. 2.2.2). A further measure of the completeness of the deconvolution is the integrated flux density measured from the residual images using the source regions. If a source is not or barely deconvolved, the flux density in the residual image will be close or equal to the flux density in the restored image, while for a perfect deconvolution in the absence of noise and systematic errors, the integrated flux in the residual image should be zero. In Fig. 9, we show the flux density ratio between the residual and restored mosaics for the Virgo cluster galaxies as a function of the mean surface brightness and mark the galaxies where the difference between the high- and low-resolution images is larger than 20%. At high resolution, for 13 out of 112 galaxies, the residual flux ratio is at least 50%, and for all but one of these cases, there is a difference of above 20% between the integrated flux densities at the different resolutions. On the contrary, at low resolution, the residual flux density ratio is always below 50%. We therefore decided to report the flux density measurements of the low-resolution images. Two galaxies in Fig. 9 show a residual flux density ratio of <-0.5. The orange cross marks VCC 144, which is located in a high-noise region and is not significantly detected in the high-resolution map, causing this fluctuation. The blue cross is VCC 758, which is located directly next to an extended radio feature that we discuss in Sect. 4.2. Around this feature, a bowl of negative surface brightness is present, which is caused by the incomplete deconvolution of the large-scale emission. Table 3 lists the measured flux densities of the LOFAR-detected Virgo cluster member galaxies together with the position, morphological classification, and r-band magnitude as provided in Kim et al. (2014). Additionally, we specify the area of the region used for the flux-density measurements as well as redshift independent distance measurements. We assume the distances of the galaxies to be identical to the mean distance of the substructure they belong to. We follow the substructure distances and membership criteria defined in (Boselli et al. 2014), which report the clusters A and C and the low-velocity cloud (LVC) at $d = 17$ Mpc, the cluster B and W' cloud at 23 Mpc and the W and M clouds at 32 Mpc. However, for consistency with the VESTIGE (Boselli et al. 2018b) and NGVS (Ferrarese et al. 2012) projects, we assume a distance of $d = 16.5$ Mpc instead
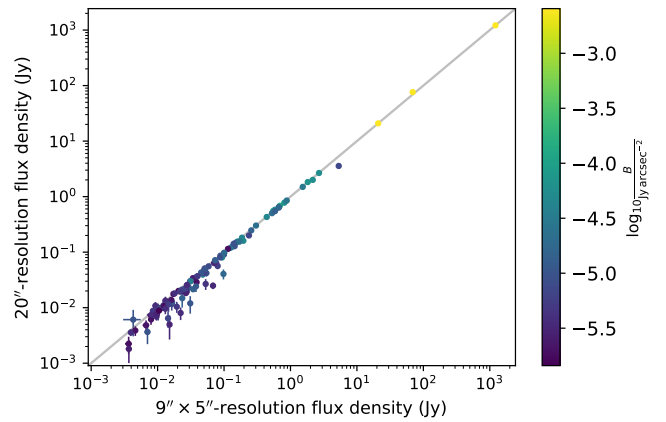
Fig. 8. Flux densities of Virgo cluster members measured from the high-resolution (9″ × 5″, x-axis) and low-resolution (20″ × 20″, y-axis) mosaics using identical regions. The color scale corresponds to the logarithm of the average surface brightness.
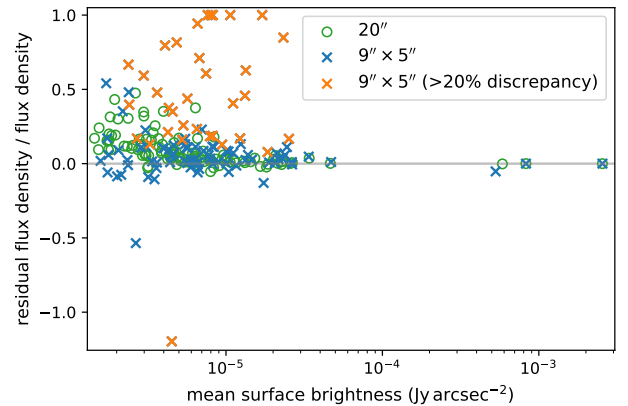
Fig. 9. Ratio between the flux density measured from the residual and the restored images (y-axis) as a function of mean surface brightness (x-axis). Circles and crosses mark measurements from the low-resolution and high-resolution mosaic, respectively. For the orange crosses, the difference between the flux density in the low- and high-resolution measurements is above 20%.

of 17 Mpc for clusters A, B, and the LVC. Based on these distances, we also calculated the radio luminosity for all galaxies in the catalog. The catalog is made available online at the CDS together with cutout images of all detected galaxies, and is

Table 4. LOFAR catalog of VCC galaxies in the background of the Virgo cluster.

VCC	NGC	IC	RA J2000 [h:m:s]	Dec J2000 [°:′:″]	Type	m_r [mag]	S [Jy]	A [″×″]	d [Mpc]	L_{144} [W Hz^{-1}]
(1)	(2)	(3)	(4)	(5)	(6)	(7)	(8)	(9)	(10)	(11)
76		3046	12:13:07.8	+12:55:05	Sc(s)I	14.16	(1.3±0.3)e-2	3420	119	(2.2±0.5)e+22
121			12:14:42.5	+12:59:24	E7/S0l7	14.87	(3.5±1.1)e-3	1463	267	(3.0±0.9)e+22
123			12:14:45.7	+13:19:35	Sa	14.57	(7.1±1.6)e-3	1346	306	(8.0±1.8)e+22
129		3060	12:15:02.0	+12:32:49	Sab	14.39	(4.9±1.5)e-3	2544	86	(4.3±1.3)e+21
134		3062	12:15:05.3	+13:35:42	ScI	14.00	(4.2±1.3)e-3	1852	116	(6.8±2.1)e+21

Notes. This table is available in its entirety at the CDS and contains the following information. The first, second, and third column list the indices of the galaxies in the VCC, NGC, and IC. The fourth to seventh columns list the optical coordinates, the morphological classification, and the *r*-band magnitude of the galaxies as reported in Binggeli et al. (1985). Column 8 shows the integrated flux density as measured from the low-resolution mosaics. Column 9 quotes the source area, Col. 10 the radial-velocity-inferred distance, and Col. 11 the resulting radio luminosity.
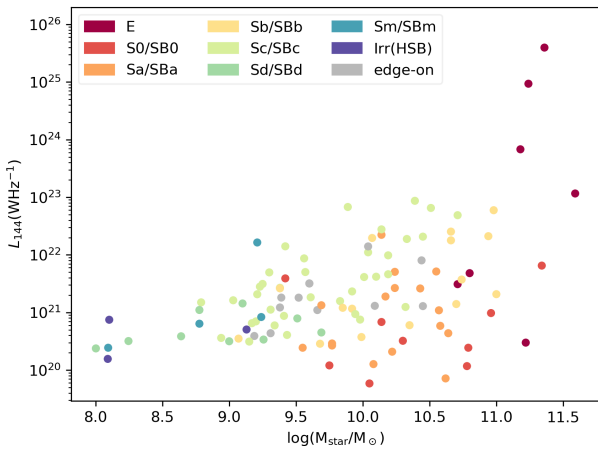
Fig. 10. Stellar mass (*x*-axis) vs. 144 MHz radio luminosity (*y*-axis) for galaxies in the LOFAR Virgo cluster catalog. The marker color corresponds to the Hubble-type.

also available at the LOFAR Surveys web page[5]. We report the LOFAR flux density measurements and the auxiliary data for the LOFAR-detected VCC background galaxies, which can be found in Table 4. Furthermore, while not suitable for the analysis of nearby galaxies, the full wide-field source catalog obtained with PyBDSF from the low-resolution mosaic is still highly valuable for studies of background objects, and so we also provide this catalog online.

The Hubble morphological classification is shown together with the stellar masses and radio-luminosities of the LOFAR Virgo cluster catalog galaxies in Fig. 10. Stellar masses were taken from Boselli et al. (2015), or, if not available, from (Boselli et al. 2014). In both cases, we used the calibration of Zibetti et al. (2009) based on the Chabrier initial mass function (Chabrier 2003). The most radio-bright and most massive objects are radio galaxies in giant ellipticals. For spiral galaxies, later-type objects are on average brighter than earlier-type spirals of similar mass.

4. Discussion

A dedicated scientific analysis of the radio data presented here will be the subject of follow-up work by our team, including a study of the radio–star formation rate(SFR) relation and the ram-pressure stripped objects in Virgo. However, here we present highlights and a brief initial discussion of radio sources that

---

are noteworthy either due to their environmental interaction or because they otherwise belong to a class of objects that is of particular interest in the radio continuum, such as giant ellipticals or dwarf galaxies. See Appendix A for an image atlas of all the galaxies.

4.1. Galaxies

VCC 144

VCC 144 is discussed in Brosch et al. (1998) as a blue compact dwarf galaxy with an extended HI envelop currently undergoing an intense starburst. These authors propose it to be an example of galaxy formation currently taking place in the southern extension of the Virgo cluster. In the optical wavelengths, VCC 144 is the faintest galaxy in our radio catalog. It is also part of the HERSCHEL far-infrared-selected star-forming dwarf galaxy survey of Grossi et al. (2016).

VCC 241 (IC 3105)

This irregular galaxy shows low-surface brightness emission in our LOFAR maps. In the south of the galaxy, the radio emission appears to extend towards the west. This feature is coincident with extra-planar HII regions traced by VESTIGE (Boselli, priv. comm.). It is therefore likely that the low-frequency radio continuum emission distribution traces cosmic-ray electrons advected due to ram pressure and/or tracing the star formation in the stripped gas.

VCC 307 (NGC 4254, M 99)

M 99 is the most radio-bright late-type galaxy in the Virgo cluster and is oriented close to face-on. The high SFR, the disturbed morphology, with a peculiar spiral arm in the west, and the long HI tail (Haynes et al. 2007) are thought to originate from an encounter with another massive cluster member in the past (Vollmer et al. 2005; Chyzy et al. 2007; Duc & Bournaud 2008; Chyzy 2008; Boselli et al. 2018a). However, even though the galaxy is located in the cluster outskirts at a distance of ≈1 Mpc to M 87, ram-pressure stripping also appears to play a role (Murphy et al. 2009). In the LOFAR images and previous low-frequency studies (Kantharia et al. 2008), the radio emission extends beyond the optical disk towards the north for at least 10 kpc; this, together with the steep surface brightness gradient toward the south, is interpreted as a sign of interaction with

the ICM while the galaxy is moving rapidly toward the cluster center.

VCC 345 (NGC 4261, 3C 270)

This bright Fanaroff-Riley type I radio galaxy sits at the center of a poor group located ~12 Mpc behind the Virgo cluster core in a structure know as the *W*-cloud (de Vaucouleurs 1961). It is well studied at radio wavelengths (Dunn et al. 2010; Kolokythas et al. 2015; Grossová et al. 2022) and shows clear signs of interaction between the AGN and the surrounding medium (O'Sullivan et al. 2011).

VCC 596 (NGC 4321, M 100)

M 100 is another grand-design spiral galaxy in the outskirts of the Virgo cluster. In the high-resolution LOFAR map, the supernova SN1979C (Urbanik et al. 1986) is visible in the southeast of the galaxy as a faint point source with a background-subtracted flux density of 3.9 ± 0.5 mJy. The galaxy does not show particularly asymmetric radio emission or other clear signs of perturbation, and is therefore currently unlikely to be undergoing significant ram-pressure stripping.

VCC 630 (NGC 4330)

The radio emission of this edge-on galaxy shows the presence of a tail in the southwest that is caused by ram-pressure stripping (Murphy et al. 2009; Vollmer et al. 2012a) and also visible in the LOFAR maps. Tails in the same region are also present in atomic hydrogen (Chung et al. 2007, 2009) and Hα (Fossati et al. 2018; Sardaneta et al. 2022).

VCC 664 (IC 3258)

To our knowledge, we detect this late-type spiral galaxy for the first time in the radio continuum. It is among the faintest Virgo cluster members at optical wavelengths in our catalog. The 3σ contours in the low-resolution map are elongated towards the west. The orientation of the tail opposite to the cluster center and the lack of any associated stellar component in the optical image suggest that the galaxy is suffering a ram-pressure stripping event. This could also explain the H$_I$ deficiency of the object (Köppen et al. 2018).

VCC 699 (IC 3268)

This galaxy is another Virgo star-forming dwarf galaxy from the Grossi et al. (2016) sample. The LOFAR detection is slightly offset from the optical image but is toward the projected center of the Virgo cluster. If real, this would imply an orbit moving away from the cluster center. In view of the relatively small mass and very high SFR, interpretation of the offset as a galactic outflow would be even more compelling.

VCC 763 (NGC 4374, M 84)

The radio galaxy M 84 is the second-brightest radio source in the central Virgo cluster after M 87 and is a well-studied example of AGN-feedback in noncentral galaxies (Finoguenov & Jones 2001; Bîrzan et al. 2004; Finoguenov et al. 2008; Laing et al. 2011; Bambic et al. 2023). The radio lobes/tails are deflected after 5 kpc, a clear sign of interaction with the ICM. They coincide with *Chandra*-detected X-ray cavities

(Finoguenov & Jones 2001; Finoguenov et al. 2008; Bambic et al. 2023). In the 144 MHz LOFAR images, the source is not significantly more extended than at GHz frequencies.

VCC 836 (NGC 4388)

This object hosts a Seyfert 2-type nucleus and is the only spiral galaxy in the Virgo cluster where an AGN contributes a large fraction of the total radio emission. The subparsec nuclear jets are oriented perpendicular to the disk (Giroletti & Panessa 2009) and give rise to a biconical outflow (Damas-Segovia et al. 2016) that is barely resolved even in our high-resolution maps. Furthermore, the galaxy, which is believed to be post-core passage and moving to the southwest, is undergoing a ram-pressure stripping event (Murphy et al. 2009) that generates a spectacular H$_I$ tail (Oosterloo & van Gorkom 2005), which can also be partly traced in Hα (Yoshida et al. 2002). In the LOFAR maps, this manifests as a strong intensity gradient on the leading side and an extension of the emission beyond the stellar component toward the trailing side of the galaxy. Still, Damas-Segovia et al. (2016) found that the leading-edge polarized outflow is able to resist the ram pressure.

VCC 865 (NGC 4396)

The presence of a tail in neutral hydrogen (Chung et al. 2007) is a sign of ram-pressure stripping also acting on this galaxy. However, a lack of compression in the H$_I$ contours (Chung et al. 2009) and a radio-to-infrared deficit (Murphy et al. 2009) on the leading edge make this interpretation somewhat uncertain. In the low-resolution LOFAR map, the radio emission shows a strong gradient toward the southeast, with a tail-like extension in the opposite direction, which favors the scenario that the galaxy is suffering from ram-pressure stripping while falling into the cluster center. Within the optical disk, the LOFAR images reveal enhanced radio emission in the leading half of the galaxy, coincident with a blue region of current or recent star formation in the optical. This may be an example of ram-pressure-induced star-formation due to gas compression on the leading edge (e.g., Boselli et al. 2021; Roberts et al. 2022a)

VCC 873 (NGC 4402)

This edge-on spiral is located at a distance of ≈ 700 kpc from M 87 and shows a truncated radio profile to the southeast with an extension in the opposite direction (see also Murphy et al. 2009). Furthermore, signs of ram-pressure stripping are also visible in the H$_I$ and the dust components of the galaxy (Crowl et al. 2005). We speculate that in the LOFAR images, a low-surface-brightness patch to the northwest of the galaxy might constitute part of a radio continuum tail, which has not previously been observed.

VCC 881 (NGC 4406, M 86)

While close in projection, the massive elliptical galaxy and its surrounding group, which is extended in the X-rays (Böhringer et al. 1994), likely lie around 2 Mpc behind M 87 (Cantiello et al. 2018). M 86 is rapidly falling towards the cluster center from behind, as indicated by the blueshifted spectrum. The galaxy was first discovered in the radio continuum at 4.9 GHz as a faint point source in Dunn et al. (2010), and was recently also detected at 1.5 GHz by Grossová et al. (2022). These latter authors concluded that the radio emission could be dominated by

star formation instead of nuclear activity; furthermore, no signs of X-ray cavities were observed.

VCC 1043 (NGC 4438)

NGC 4438 is a unique object in the Virgo cluster, which shows strong disruption of the stellar component. This was caused by a gravitational interaction with NGC 4435 and NGC 4406 (M 86), to which it is connected by filaments visible in Hα emission (Kenney et al. 2008). NGC 4438 shows peculiar radio emission; a central point source corresponds to the LINER-type AGN (Decarli et al. 2007) and unresolved inner lobes (Hota et al. 2007), with an accompanying radio bubble to the west (Weżgowiec et al. 2007; Vollmer et al. 2009).

VCC 1226 (NGC 4472, M 49)

Being optically brighter than M 87, M 49 is the BCG of a southern subcluster falling into the Virgo core almost perpendicular to the line of sight (Mei et al. 2007). It lies at a projected distance of 1.3 Mpc ($1.3 r_{\rm vir}$) from the cluster center. At GHz frequencies, it hosts a slightly extended, double-lobed radio source of low power (e.g., Dunn et al. 2010). X-ray observations with the *XMM-Newton* and *Chandra* satellites (Kraft et al. 2011; Gendron-Marsolais et al. 2017; Su et al. 2019) revealed the presence of cavities in the thermal plasma, which have been excavated by the AGN. These inner cavities connect to X-ray filaments of $\sim$30 kpc in length. These are thought to originate from a previous nuclear outbreak, which can only be revealed in the radio by deep, low-frequency observations. With our LOFAR survey, we report the discovery of radio tails that correspond to the X-ray features. The tails extend far beyond the X-ray cavities for a projected distance of 150 kpc ($\cong$0.52°) and are detected at a surface-brightness significance of $2-4\sigma$ even in the high-resolution image (panel a) of Fig. 7). Due to the ram pressure they experience from the Virgo ICM, they are bent southwards, giving rise to a wide-angle tail morphology. Follow-up studies of the spectral aging along the tails using 54 MHz observations of LOFAR LBA will allow us to constrain both the duty cycle of the AGN and the infall-history of the M 49 subcluster.

VCC 1316 (NGC 4486, M 87)

M 87 is the famous radio galaxy at the center of the Virgo cluster and is among the brightest radio sources on the sky. It consists of an inner pair of jets also visible in the X-ray and optical and forming a cocoon with an extension of $\sim$6 kpc (see Fig. 3). This emission is embedded in a highly extended halo with a size of $\sim$75 kpc, which contains the outer jets with a prominent smoking-gun morphology. The extended emission was studied in detail in Owen et al. (2000) at 300 MHz using the VLA, which for the past 20 yr remained the highest quality published image of the large-scale structure of M 87. In the early commissioning stage of LOFAR, the source was studied from 20 to 160 MHz, although with limited resolution and image fidelity owing to the incompleteness of the instrument and the lack of sophisticated calibration strategies (de Gasperin et al. 2012). A high-fidelity LOFAR LBA image is provided in de Gasperin et al. (2020). M 87 and the filaments permeating the extended halo of the source will be the subject of a dedicated multifrequency study combining our LOFAR data with unpublished VLA and MeerKAT observations (de Gasperin et al., in prep.).

VCC 1401 (NGC 4501, M 88)

The radio map Fig. 7b of this bright, highly inclined spiral galaxy shows significant asymmetry with a strong gradient toward the southwest. This asymmetry is caused by the ram-pressure stripping the galaxy experiences during the infall onto the central Virgo cluster. In our LOFAR 144 MHz image, the radio emission in the northeast extends further from the optical disk than at 1.4 GHz (Vollmer et al. 2010), which is in agreement with the greater age of the advected cosmic-ray electrons.

VCC 1450 (IC 3476)

Boselli et al. (2021) reported the presence of ionized gas tails for VCC 1450 caused by a recent onset of ram-pressure stripping. This is in agreement with the LOFAR images, where a strong gradient on the leading (eastern) side and a tail on the trailing side are visible. To the best of our knowledge, this is the first time this tail is reported in the radio continuum.

VCC 1516 (NGC 4522)

This galaxy is observed at high inclination and shows strongly asymmetric radio emission with a tail toward the northwest (Vollmer et al. 2004; Murphy et al. 2009). It is undergoing active ram-pressure stripping and also shows extraplanar and UV emission (Kenney & Koopmann 1999; Kenney et al. 2004; Vollmer et al. 2012b).

VCC 1532 (IC 800)

The LOFAR maps of VCC 1532 reveal a gradient of radio emission at the edge of the galaxy facing the cluster center, and a tail in the opposite direction. To the best of our knowledge, the galaxy has not previously been reported to show signs of ram-pressure stripping. We therefore note it as a new candidate for ongoing ram-pressure stripping.

VCC 1575 (IC 3521)

This is another Virgo star-forming dwarf galaxy from the Grossi et al. (2016) sample. The LOFAR emission appears to extend beyond the optical image of the galaxy, which implies a galactic outflow, consistent with the high SFR of this low-mass galaxy.

VCC 1632 (NGC 4552, M 89)

M 89 hosts a nuclear point source surrounded by two lobes reminiscent of ears, each of 5 kpc in extent. Those ears correspond to X-ray cavities revealed by *Chandra* studies (Machacek et al. 2006; Allen et al. 2006; Kraft et al. 2017).

VCC 1686 (IC 3583)

VCC 1686 has a projected location very close to VCC 1690, but both galaxies differ by more than 1300 km s^{-1} in radial velocity, making a tidal interaction between the two galaxies very unlikely. Still, there is a spur of LOFAR emission in the south of VCC 1686 pointing toward VCC 1690. This feature also has a counterpart in at least two independent Hα maps of VCC 1686. The origin of the Hα feature is unclear, but the radio emission is more extended than the optical image of the galaxies over the whole quadrant, and so this may be a large-scale outflow. This would be consistent with the high SFR of this dwarf galaxy. We

note that the two relatively bright radio sources are likely background and not physically connected to VCC 1686. VCC 1686 also belongs to the Grossi et al. (2016) sample.

VCC 1690 (NGC 4569, M 90)

M 90 is one of the brightest spiral galaxies in the Virgo cluster. As traced by tails of ionized gas to the east (Boselli et al. 2016), it is currently undergoing a ram-pressure stripping event. Observations in the radio continuum revealed symmetric bubbles extending up to 24 kpc perpendicular to the disk (Chyzy et al. 2006). Our LOFAR map detects both radio lobes and the southwestern ridge of the emission connected to the star-forming disk. The southwestern ridge likely results from gas and magnetic field compression by the ambient ICM. As M 90 does not show signs of strong nuclear activity, it was concluded that the lobes are likely powered by a nuclear starburst event. A detailed analysis of the stellar emission in the innermost region by Gabel & Bruhweiler (2002) using spectral synthesis led the authors to propose an age for the starburst of $5-6$ Myr and 5×10^4 O and B stars, which would be sufficient to create a large-scale outflow or wind.

VCC 1727 (NGC 4579, M 58)

The massive barred spiral galaxy M 58 hosts a Seyfert 2-type low-luminosity AGN (Contini 2004). Despite its significant H I deficiency, it was found to have the radio properties of a normal star-forming galaxy by Vollmer et al. (2013), even after subtracting the AGN contribution. In the LOFAR images, a central point source can be observed, with swirling features extending over 5 kpc; as their direction is counterclockwise, opposite to the spiral arms, they most likely correspond to the AGN jets. The central structure is embedded in low-surface brightness emission covering a region that is similar in size to the optical disk that traces the star formation activity.

VCC 1791 (IC 3617)

VCC 1791 also belongs to the Grossi et al. (2016) sample. It has a relatively high SFR (but lower than that of VCC 1686) but also a relatively low mass. Therefore, the extent of the radio emission beyond the optical body of the galaxy is suggestive of an outflow. The brightest peak of the radio emission coincides with three very blue compact knots.

VCC 1932 (NGC 4634)

The low-resolution LOFAR map of this edge-on spiral galaxy, which forms a close pair with NGC 4633, shows extra-planar radio emission to the west, which could be interpreted as a radio tail. In the same direction, a star forming object can be seen that was likely created from material stripped (or tidally ejected) from VCC 1932 (Stein et al. 2018). However, the galaxy is not known to show a tail at any other wavelength, and therefore interpretation of the radio morphology remains somewhat difficult.

VCC 1972 (NGC 4647)

The spiral galaxy VCC 1972 lies close to M 60 in an eastern subcluster of Virgo. The radio surface brightness and the molecular gas distribution (Young et al. 2006) of this galaxy are asymmetric, which is likely due to ram pressure exerted by the ICM around M 60 and/or a disturbance of the gravitational well.

VCC 1978 (NGC 4649, M 60)

This giant elliptical galaxy is the most massive galaxy in the Virgo cluster and dominates a small, X-ray-bright subcluster (Böhringer et al. 1994). Deep *Chandra* and VLA observations revealed the presence of X-ray cavities coincident with the radio jets of the central AGN (Shurkin et al. 2007; Dunn et al. 2010; Paggi et al. 2014; Grossová et al. 2022), placing it among the Virgo galaxies that are prime examples of AGN feedback in noncentral galaxies. In the 144 MHz LOFAR images, the inner radio source of 5 kpc in extension, which is also visible at GHz frequencies, is embedded in an area of low-surface brightness diffuse emission of 75 kpc in size.

4.2. Extended emission

For the following discussion of emission on large angular scales, it must be considered that radio interferometers have a reduced sensitivity to features beyond a certain extent; for LOFAR, the flux density loss at a scale of 18′ is around 20% (Bruno et al. 2023), and more extended sources will be attenuated more drastically. Figure 11 shows the very low-resolution source-subtracted mosaic that is sensitive to large-scale diffuse radio emission in the Virgo cluster environment. Among the most prominent large-scale features are at least four sets of diagonal stripes that extend from the northeast toward the southwest and are marked by black dashed lines. Given their location and orientation, they are certainly associated with the North Polar Spur (Loop I), a Galactic spherical structure which is thought to either be local ($d \sim 100$ pc Salter 1983) or originating from the Galactic center, as indicated by studies of the coincident X-ray emission (see also Fig. 1, Sofue 2000; Predehl et al. 2020). Further large-scale emission with an extent of $\approx 1°$ is marked in Fig. 11 by two dashed ellipses. The emission in the SW follows a similar orientation to the tails of M 49, which might indicate that it is part of those. However, the emission does not show a clear connection to M 49. Furthermore, if the emission were indeed due to a tail of this giant elliptical galaxy, it would follow a highly unexpected surface brightness trend with a complete fainting and a subsequent rebrightening. While this is not fully unheard of for cluster radio galaxies (de Gasperin 2017; Cuciti et al. 2018; Edler et al. 2022), it is a rare phenomenon. Thus, we consider it unlikely that the southwestern extended feature is causally connected to the AGN in M 49. However, we note that directly coincident with the radio emission is the W' cloud (de Vaucouleurs 1961), a group of galaxies ~ 5.5 Mpc behind M 49 and located in a filament connecting the cluster to the background W cloud (Binggeli et al. 1993; Mei et al. 2007). In Fig. 12, we show that the elongated structure of the filament is apparent both in the galaxy density distribution and the eROSITA (McCall et al., in prep.) X-ray surface brightness distribution and has a similar morphology and location to the radio emission. The displayed galaxy density was obtained from the EVCC by smoothing the galaxy distribution with a Gaussian kernel of $\sigma = 14′$ in width. These aspects combined suggest that the emission originates from phenomena related to the ICM or intragroup medium, that is, either turbulent reacceleration processes or accretion shocks. This could explain the similar morphology of the X-ray and radio signals. An alternative explanation is that the radio emission traces a past phase of nuclear activity of a galaxy in the group, such as the
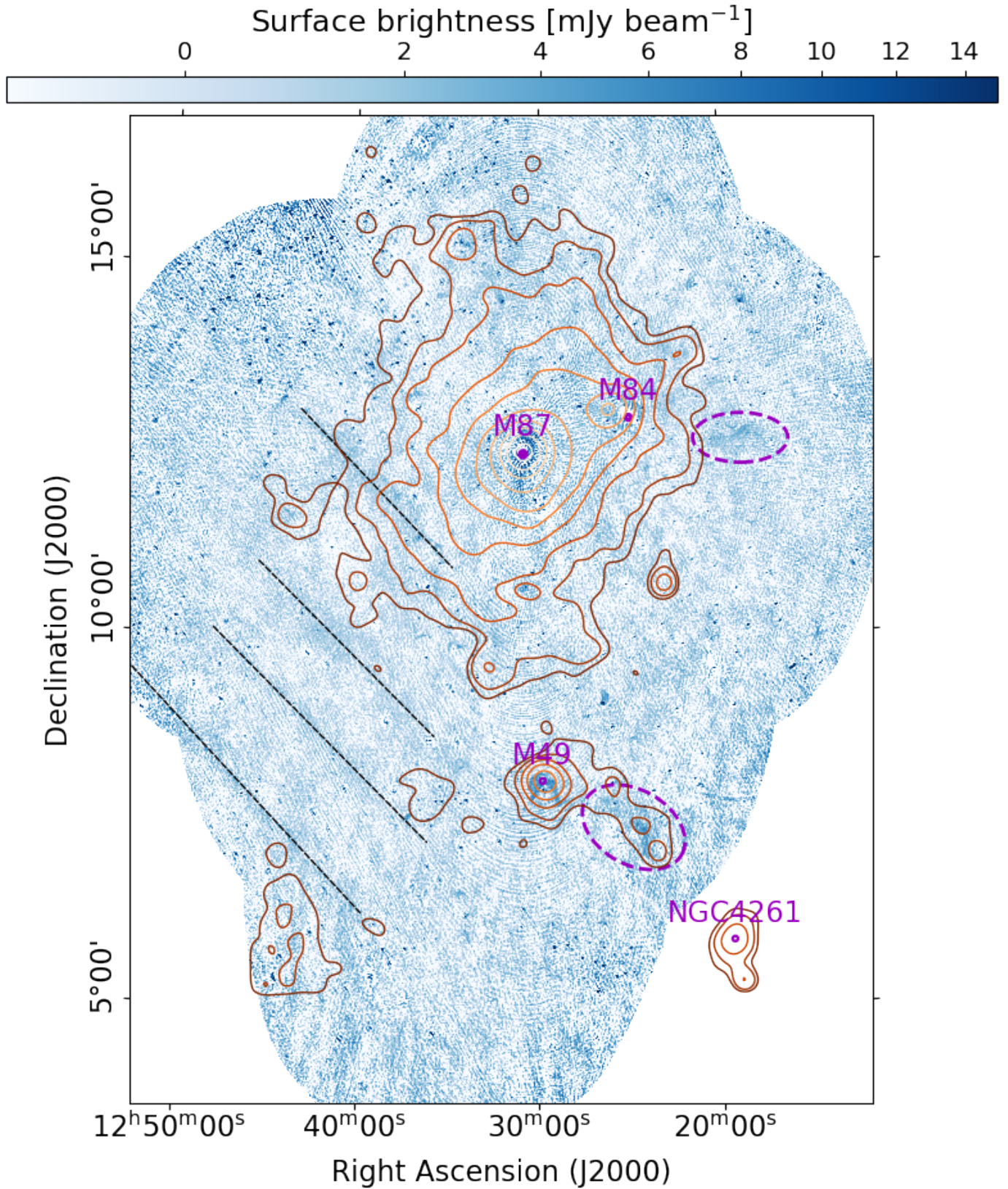
Fig. 11. Compact source-subtracted mosaic at 1′ resolution. Due to the poor quality of the very low-resolution images, field 1 and 8 are excluded. Black dashed lines correspond to large-scale Galactic emission of the North Polar Spur (NPS), purple circles mark the position of the giant elliptical galaxies M 49 (NGC 4472), M 84 (NGC 4374), and M 87 (NGC 4486). The dashed purple ellipses highlight candidate extragalactic emission, which could be related to the wider Virgo environment, and orange contours mark the eROSITA compact source-subtracted X-ray surface brightness (McCall et al., in prep.).
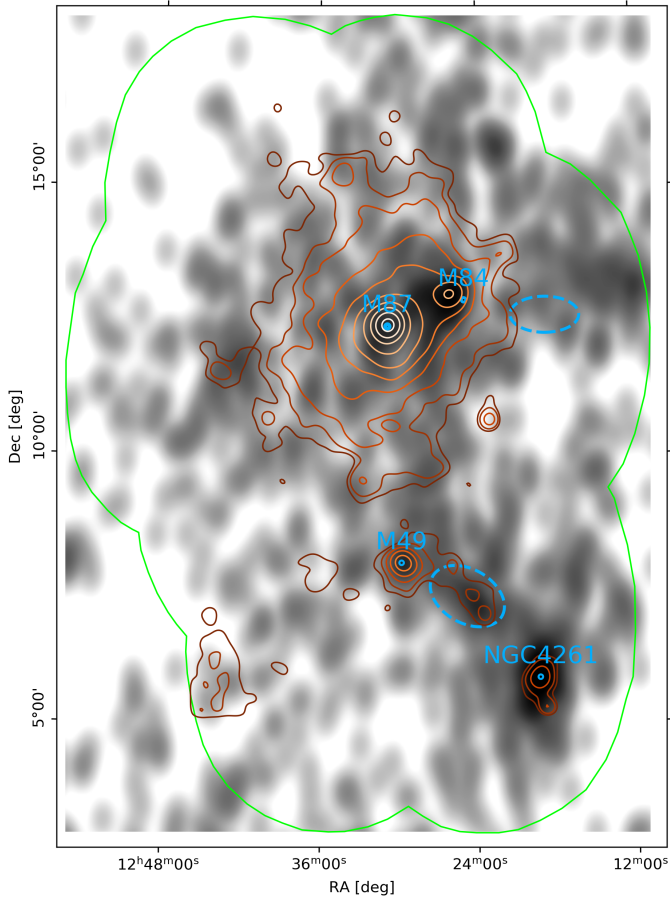
Fig. 12. Projected galaxy density of the EVCC. Orange contours show the eROSITA source-subtracted X-ray surface brightness (McCall et al., in prep.), the green contour outlines the footprint of the LOFAR observations, and the blue circles and dotted ellipses mark individual galaxies and the extended emission as in Fig. 11.

dominant elliptical NGC 4365. However, at present, NGC 4365 is not associated with a compact radio source. The only radio-detected galaxy nearby is NGC 4370, although there is no clear connection to the diffuse emission. The extended radio source coincident with the W' group or filament will be the subject of a forthcoming multifrequency follow-up study. The second extended and elongated feature in the northeast is of similar size, but does not directly coincide with an over-density of galaxies in the EVCC or with an increase in surface brightness in the ROSAT (Böhringer et al. 1994) or eROSITA (McCall et al., in prep.) X-ray images. However, it is located between the Virgo core and the M cloud of galaxies, which is another concentration of galaxies in the wider Virgo environment (de Vaucouleurs 1961; Mei et al. 2007).

The three small circles in Fig. 11 mark the location of extended emission possibly associated with giant elliptical galaxies in the cluster. The extended tails of M 49 are discussed in Sect. 4.1. Around M 87, there is extended emission on a scale of ~1° (four times larger than M 87). Given the cool-core nature of the Virgo cluster and the 200−300 kpc extent of the candidate diffuse emission, a tentative possibility is that this emission is caused by a radio mini-halo (Gitti et al. 2004; Giacintucci et al. 2017, 2019; van Weeren et al. 2019) caused by the sloshing of gas in the Virgo core (Gatuzz et al. 2022). However, due to the presence of strong systematic uncertainties directly next to M 87, we cannot conclude with certainty that the emission is

physical. Around the bright (21 Jy) radio galaxy M 84, a circular halo of emission with an embedded negative hole is most likely a calibration or imaging artifact.

5. Summary

In this work, we present the LOFAR HBA Virgo cluster survey, which is the first data release of the ViCTORIA project and represents the deepest wide-field radio survey of the Virgo cluster field published to date. This advance was made possible by the general progress in low-frequency radio calibration techniques and the development of a specifically tailored subtraction procedure introduced in this work, which mitigates dynamic range limitations due to the extremely bright source M 87. Within the virial radius of the cluster, where we have increased exposure time and pointing overlap, we reach a median noise level of 140 μJy beam^{-1} at a resolution of $9'' \times 5''$, while across the full survey area, the median noise is twice as high. We use this data to create a catalog of the radio properties of 112 LOFAR-detected certain and possible Virgo cluster galaxies ($v_{\rm rad} < 3000 \, \rm km \, s^{-1}$). The detected objects include at least 18 cases of galaxies exhibiting a radio morphology indicative of ongoing ram-pressure stripping. Of those, we report VCC 664 (IC 3258), VCC 1532 (IC 800), and VCC 1932 (NGC 4632) as new ram-pressure-stripping candidates. Further, for the giant elliptical galaxy VCC 1226 (NGC 4472, M 49), we reveal the presence of old radio tails of 0.5°/150 kpc in extent. Due to the interaction with the ICM, the tails are bent toward the south and assume a wide-angle tail morphology. The image cutouts, the catalog of the Virgo galaxies, and the full mosaics are made available online[6].

We also investigated the presence of large-scale diffuse emission in the Virgo cluster. While no radio emission attributable to the radio halo or radio relic phenomena is found, we detect extended emission coincident with the W' group in a filament between Virgo and the background W cloud. The scale of this feature is ≈1 deg and emission with a similar extent and orientation is also present in the eROSITA/SRG X-ray map of the cluster. We therefore speculate that this radio emission may be caused by accretion processes due to shocks or turbulence.

This work is the first part of ViCTORIA, a project designed to drastically improve the multifrequency radio coverage of the Virgo cluster. Further planned radio surveys are being conducted at 54 MHz with the LOFAR low-band antenna system as well as in the L-band using MeerKAT, including the 21 cm line. In a forthcoming work of the ViCTORIA project, we will use the LOFAR data presented here to analyze the impact of the cluster environment on the evolution of star-forming galaxies in Virgo. Further, we will employ the multifrequency data provided by ViCTORIA for detailed spectral studies of the interacting radio tail we unveil for VCC 1226 and the extended emission coincident with the W' filament.

6 https://lofar-surveys.org/virgo_survey.html

References

Abazajian, K. N., Adelman-Mccarthy, J. K., Agüeros, M. A., et al. 2009, ApJS, 182, 543

Aguerri, J. A. L., Gerhard, O. E., Arnaboldi, M., et al. 2005, AJ, 129, 2585

Allen, S. W., Dunn, R. J. H., Fabian, A. C., Taylor, G. B., & Reynolds, C. S. 2006, MNRAS, 372, 21

Arnaboldi, M., Gerhard, O., Aguerri, J. A. L., et al. 2005, ApJ, 614, L33

Baars, J. W. M., Genzel, R., Pauliny-Toth, I. I. K., & Witzel, A. 1977, A&A, 61, 99

Bambic, C. J., Russell, H. R., Reynolds, C. S., et al. 2023, MNRAS, 522, 4374

Binggeli, B., Sandage, A., & Tammann, G. A. 1985, AJ, 90, 1681

Binggeli, B., Tammann, G. A., Sandage, A., et al. 1987, AJ, 94, 251

Binggeli, B., Popescu, C. C., Tammann, G. A., et al. 1993, A&AS, 98, 275

Bîrzan, L., Rafferty, D. A., McNamara, B. R., Wise, M. W., & Nulsen, P. E. J. 2004, ApJ, 607, 800

Bîrzan, L., McNamara, B. R., Nulsen, P. E. J., Carilli, C. L., & Wise, M. W. 2008, ApJ, 686, 859

Böhringer, H., Briel, U. G., Schwarz, R. A., et al. 1994, Nature, 368, 828

Boselli, A., Eales, S., Cortese, L., et al. 2010, PASP, 122, 261

Boselli, A., Boissier, S., Heinis, S., et al. 2011, A&A, 528, A107

Boselli, A., Voyer, E., Boissier, S., et al. 2014, A&A, 570, A69

Boselli, A., Fossati, M., Gavazzi, G., et al. 2015, A&AS,, 579, A102

Boselli, A., Cuillandre, J. C., Fossati, M., et al. 2016, A&A, 587, A68

Boselli, A., Fossati, M., Cuillandre, J. C., et al. 2018a, A&A, 615, A114

Boselli, A., Fossati, M., Ferrarese, L., et al. 2018b, A&A, 614, A56

Boselli, A., Lupi, A., Epinat, B., et al. 2021, A&A, 646, A139

Boselli, A., Fossati, M., & Sun, M. 2022, A&ARv, 30, 3

Brosch, N., Almoznino, E., & Hoffman, G. L. 1998, A&A, 331, 873

Brown, T., Wilson, C. D., Zabel, N., et al. 2021, ApJS, 257, 21

Brunetti, G., & Jones, T. W. 2014, Int. J. Mod. Phys. D, 23, 1430007-98

Bruno, L., Brunetti, G., Botteon, A., et al. 2023, A&A, 672, A41

Calistro Rivera, G., Williams, W. L., Hardcastle, M. J., et al. 2017, MNRAS, 469, 3468

Cantiello, M., Blakeslee, J. P., Ferrarese, L., et al. 2018, ApJ, 856, 126

Capetti, A., Kharb, P., Axon, D. J., Merritt, D., & Baldi, R. D. 2009, AJ, 138, 1990

Cassano, R. 2010, A&A, 517, A10

Chabrier, G. 2003, PASP, 115, 763

Chung, A., van Gorkom, J. H., Kenney, J. D. P., & Vollmer, B. 2007, ApJ, 659, L115

Chung, A., Van Gorkom, J. H., Kenney, J. D., Crowl, H., & Vollmer, B. 2009, AJ, 138, 1741

Chyzy, K. T. 2008, A&A, 482, 755

Chyzy, K. T., Soida, M., Bomans, D. J., et al. 2006, A&A, 447, 465

Chyzy, K. T., Ehle, M., & Beck, R. 2007, A&A, 474, 415

Condon, J. J., Cotton, W. D., Greisen, E. W., et al. 1998, AJ, 115, 1693

Contini, M. 2004, MNRAS, 354, 675

Cote, P., Blakeslee, J. P., Ferrarese, L., et al. 2004, ApJS, 153, 223

Crowl, H. H., Kenney, J. D. P., van Gorkom, J. H., & Vollmer, B. 2005, AJ, 130, 65

Cuciti, V., Brunetti, G., Van Weeren, R., et al. 2018, A&A, 609, A61

Damas-Segovia, A., Beck, R., Vollmer, B., et al. 2016, ApJ, 824, 30

Davies, J. I., Baes, M., Bendo, G. J., et al. 2010, A&A, 518, L48

de Gasperin, F. 2017, MNRAS, 467, 2234

de Gasperin, F., Orrú, E., Murgia, M., et al. 2012, A&A, 547, A56

de Gasperin, F., Dijkema, T. J., Drabent, A., et al. 2019, A&A, 622, A5

de Gasperin, F., Vink, J., McKean, J. P., et al. 2020, A&A, 635, A150

de Vaucouleurs, G. 1961, ApJS, 6, 213

Decarli, R., Gavazzi, G., Arosio, I., et al. 2007, MNRAS, 381, 136

Dey, A., Schlegel, D. J., Lang, D., et al. 2019, AJ, 157, 168

Duc, P.-A., & Bournaud, F. 2008, ApJ, 673, 787

Dunn, R. J. H., Allen, S. W., Taylor, G. B., et al. 2010, MNRAS, 404, 180

Edler, H. W., de Gasperin, F., Brunetti, G., et al. 2022, A&A, 666, A3

Fabian, A. C. 2012, ARA&A, 50, 455

Ferrarese, L., Côté, P., Cuillandre, J.-C., et al. 2012, ApJS, 200, 4

Finoguenov, A., & Jones, C. 2001, ApJ, 547, L107

Finoguenov, A., Ruszkowski, M., Jones, C., et al. 2008, ApJ, 686, 911

Forman, W., Jones, C., Churazov, E., et al. 2007, ApJ, 665, 1057

Fossati, M., Mendel, J. T., Boselli, A., et al. 2018, A&A, 614, A57

Gabel, J. R., & Bruhweiler, F. C. 2002, AJ, 124, 737

Gallo, E., Treu, T., Marshall, P. J., et al. 2010, ApJ, 714, 25

Gaspari, M., Brighenti, F., & Temi, P. 2012, MNRAS, 424, 190

Gatuzz, E., Sanders, J. S., Dennerl, K., et al. 2022, MNRAS, 511, 4511

Gavazzi, G., & Boselli, A. 1999, A&A, 343, 93

Gavazzi, G., Boselli, A., & Kennicutt, R. 1991, AJ, 101, 1207

Gavazzi, G., Boselli, A., Scodeggio, M., Pierini, D., & Belsole, E. 1998, MNRAS, 304, 595

Gendron-Marsolais, M., Kraft, R. P., Bogdan, A., et al. 2017, ApJ, 848, 26

Giacintucci, S., Markevitch, M., Cassano, R., et al. 2017, ApJ, 841, 71

Giacintucci, S., Markevitch, M., Cassano, R., et al. 2019, ApJ, 880, 70

Giroletti, M., & Panessa, F. 2009, ApJ, 706, 260

Gitti, M., Brunetti, G., Feretti, L., & Setti, G. 2004, A&A, 417, 1

Grossi, M., Corbelli, E., Bizzocchi, L., et al. 2016, A&A, 590, A27

Grossová, R., Werner, N., Massaro, F., et al. 2022, ApJS, 258, 30

Gunn, J. E., & Gott, J. Richard, I. 1972, ApJ, 176, 1

Gürkan, G., Hardcastle, M. J., Smith, D. J. B., et al. 2018, MNRAS, 475, 3010

Hales, S. E. G., Baldwin, J. E., & Warner, P. J. 1988, MNRAS, 234, 919

Haynes, M. P., Giovanelli, R., & Kent, B. R. 2007, ApJ, 665, L19

Hota, A., Saikia, D. J., & Irwin, J. A. 2007, MNRAS, 380, 1009

Hurley-Walker, N., Callingham, J. R., Hancock, P. J., et al. 2017, MNRAS, 464, 1146

Ignesti, A., Vulcani, B., Poggianti, B. M., et al. 2022a, ApJ, 937, 58

Ignesti, A., Vulcani, B., Poggianti, B. M., et al. 2022b, ApJ, 924, 64

Intema, H. T., Jagannathan, P., Mooley, K. P., & Frail, D. A. 2017, A&A, 598, A78

Jacobs, D. C., Aguirre, J. E., Parsons, A. R., et al. 2011, ApJ, 734, L34

Kantharia, N. G., Rao, A. P., & Sirothia, S. K. 2008, MNRAS, 383, 173

Kenney, J. D. P., & Koopmann, R. A. 1999, AJ, 117, 181

Kenney, J. D. P., van Gorkom, J. H., & Vollmer, B. 2004, AJ, 127, 3361

Kenney, J. D. P., Tal, T., Crowl, H. H., Feldmeier, J., & Jacoby, G. H. 2008, ApJ, 687, L69

Kim, S., Rey, S.-C., Jerjen, H., et al. 2014, ApJS, 215, 22

Kolokythas, K., O'Sullivan, E., Giacintucci, S., et al. 2015, MNRAS, 450, 1732

Köppen, J., Jáchym, P., Taylor, R., & Palouš, J. 2018, MNRAS, 479, 4367

Kraft, R. P., Forman, W. R., Jones, C., et al. 2011, ApJ, 727, 41

Kraft, R. P., Roediger, E., Machacek, M., et al. 2017, ApJ, 848, 27

Lacy, M., Baum, S. A., Chandler, C. J., et al. 2020, PASP, 132, 035001

Laing, R. A., Guidetti, D., Bridle, A. H., Parma, P., & Bondi, M. 2011, MNRAS, 417, 2789

Machacek, M., Nulsen, P. E. J., Jones, C., & Forman, W. R. 2006, ApJ, 648, 947
McConnell, D., Hale, C. L., Lenc, E., et al. 2020, PASA, 37, e048
Mei, S., Blakeslee, J., Cote, P., et al. 2007, ApJ, 655, 144
Merloni, A., Predehl, P., Becker, W., et al. 2012, arXiv e-prints [arXiv:1209.3114]
Miller, N. A., & Owen, F. N. 2001, AJ, 121, 1903
Million, E. T., Werner, N., Simionesc, A., et al. 2010, MNRAS, 407, 2046
Mohan, N., Rafferty, D., Mohan, N., & Rafferty, D. 2015, Astrophysics Source Code Library [record ascl:1502.007]
Murphy, E. J., Kenney, J. D., Helou, G., Chung, A., & Howell, J. H. 2009, ApJ, 694, 1435
Offringa, A. R., & Smirnov, O. 2016, MNRAS, 000, 1
Offringa, A. R., Van De Gronde, J. J., & Roerdink, J. B. 2012, A&AS, 539, A95
Offringa, A. R., McKinley, B., Hurley-Walker, N., et al. 2014, MNRAS, 444, 606
Oosterloo, T., & van Gorkom, J. 2005, A&A, 437, L19
O'Sullivan, E., Worrall, D. M., Birkinshaw, M., et al. 2011, MNRAS, 416, 2916
Owen, F. N., Eilek, J. A., & Kassim, N. E. 2000, ApJ, 543, 611
Paggi, A., Fabbiano, G., Kim, D. W., et al. 2014, ApJ, 787, 134
Perley, R. A., & Butler, B. J. 2017, ApJS, 230, 7
Predehl, P., Sunyaev, R. A., Becker, W., et al. 2020, Nature, 588, 227
Predehl, P., Andritschke, R., Arefiev, V., et al. 2021, A&A, 647, A1
Roberts, I. D., Van Weeren, R. J., Mcgee, S. L., et al. 2021a, A&A, 650, A111
Roberts, I. D., van Weeren, R. J., McGee, S. L., et al. 2021b, A&A, 652, A153
Roberts, I. D., Lang, M., Trotsenko, D., et al. 2022a, ApJ, 941, 77
Roberts, I. D., Van Weeren, R. J., Timmerman, R., et al. 2022b, A&A, 658, A44
Roger, R. S., Costain, C. H., & Bridle, A. H. 1973, AJ, 78, 1030
Salter, C. J. 1983, BASI, 11, 1
Sarazin, C. L. 1986, Rev. Mod. Phys., 58, 1
Sardaneta, M. M., Amram, P., Boselli, A., et al. 2022, A&A, 659, A45
Scaife, A. M. M., & Heald, G. H. 2012, MNRAS, 423, 30
Shimwell, T. W., Röttgering, H. J. A., Best, P. N., et al. 2017, A&A, 598, 104
Shimwell, T. W., Tasse, C., Hardcastle, M. J., et al. 2019, A&A 622, A1
Shimwell, T. W., Hardcastle, M. J., Tasse, C., et al. 2022, A&A, 659, A1
Shurkin, K., Dunn, R. J. H., Gentile, G., Taylor, G. B., & Allen, S. W. 2007, MNRAS, 383, 923
Simionescu, A., Werner, N., Mantz, A., Allen, S. W., & Urban, O. 2017, MNRAS, 469, 1476
Sofue, Y. 2000, ApJ, 540, 224
Soria, R., Kolehmainen, M., Graham, A. W., et al. 2022, MNRAS, 512, 3284
Stein, Y., Bomans, D. J., Kamphuis, P., et al. 2018, A&A, 620, A29
Su, Y., Kraft, R. P., Nulsen, P. E. J., et al. 2019, AJ, 158, 6
Tasse, C. 2014a, arXiv e-prints [arXiv:1410.8706]
Tasse, C. 2014b, A&A, 566, A127
Tasse, C., Hugo, B., Mirmont, M., et al. 2018, A&A, 611, A87
Tasse, C., Shimwell, T., Hardcastle, M. J., et al. 2021, A&A, 648, A1
Urban, O., Werner, N., Simionescu, A., Allen, S. W., & Böhringer, H. 2011, MNRAS, 414, 2101
Urbanik, M., Klein, U., & Graeve, R. 1986, A&A, 166, 107
van der Kruit, P. C., 1971, A&A, 15, 110
van der Kruit, P. C., 1973, A&A, 29, 263
van der Tol, S., Veenboer, B., & Offringa, A. R. 2019, A&A, 616, A27
van Haarlem, M. P., Wise, M. W., Gunst, A. W., et al. 2013, A&A, 556, A2
van Weeren, R. J., de Gasperin, F., Akamatsu, H., et al. 2019, Space Sci. Rev., 215, 16
van Weeren, R. J., Shimwell, T. W., Botteon, A., et al. 2021, A&A, 651, A115
Vollmer, B., Beck, R., Kenney, J. D. P., & van Gorkom, J. H. 2004, AJ, 127, 3375
Vollmer, B., Huchtmeier, W., & Van Driel, W. 2005, A&A, 439, 921
Vollmer, B., Soida, M., Beck, R., et al. 2007, A&A, 464, L37
Vollmer, B., Soida, M., Chung, A., et al. 2009, A&A, 496, 669
Vollmer, B., Soida, M., Chung, A., et al. 2010, A&A, 512, A36
Vollmer, B., Soida, M., Braine, J., et al. 2012a, A&A, 537, A143
Vollmer, B., Wong, O. I., Braine, J., Chung, A., & Kenney, J. D. P. 2012b, A&A, 543, A33
Vollmer, B., Soida, M., Beck, R., et al. 2013, A&A, 553, A116
Weżgowiec, M., Urbanik, M., Vollmer, B., et al. 2007, A&A, 471, 93
Weżgowiec, M., Urbanik, M., Beck, R., Chyży, K. T., & Soida, M. 2012, A&A, 545, A69
Yoshida, M., Yagi, M., Okamura, S., et al. 2002, ApJ, 567, 118
Young, L. M., Rosolowsky, E., van Gorkom, J. H., & Lamb, S. A. 2006, ApJ, 650, 166
Zibetti, S., Charlot, S., & Rix, H.-W. 2009, MNRAS, 400, 1181

Appendix A: Images of Virgo cluster galaxies

NGC 4168 / VCC 49

(a)

NGC 4178 / IC 3042 / VCC 66

(b)
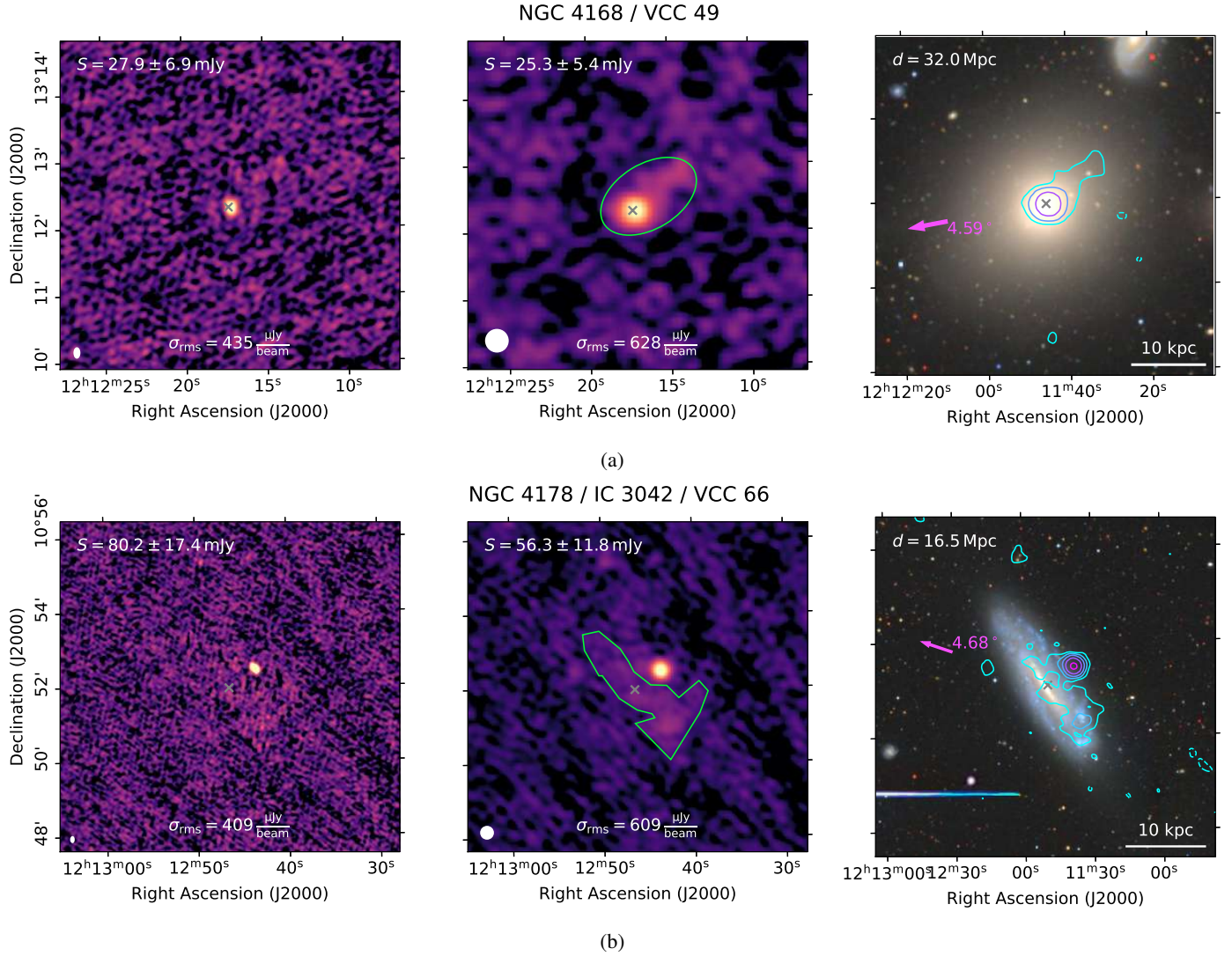
Fig. A.1: LOFAR images of the galaxy VCC 144 at resolutions of $9'' \times 5''$ (left panel) and $20''$ (center panel), and the corresponding optical image of the DESI Legacy Imaging Survey DR9 (Dey et al. 2019) with the $20''$ LOFAR contours starting from 3σ and increasing in powers of two (right panel). The region outlined in green in the central panel marks the area used for the flux density measurement at high- and low-resolution. The measured flux density is displayed in the top left corner and the background RMS σ_{rms} of the maps at the bottom. In the right panel, the pink arrow marks the direction of and distance to the cluster center (M 87), and the redshift-independent distance d is reported in the top left.

NGC 4180 / VCC 73
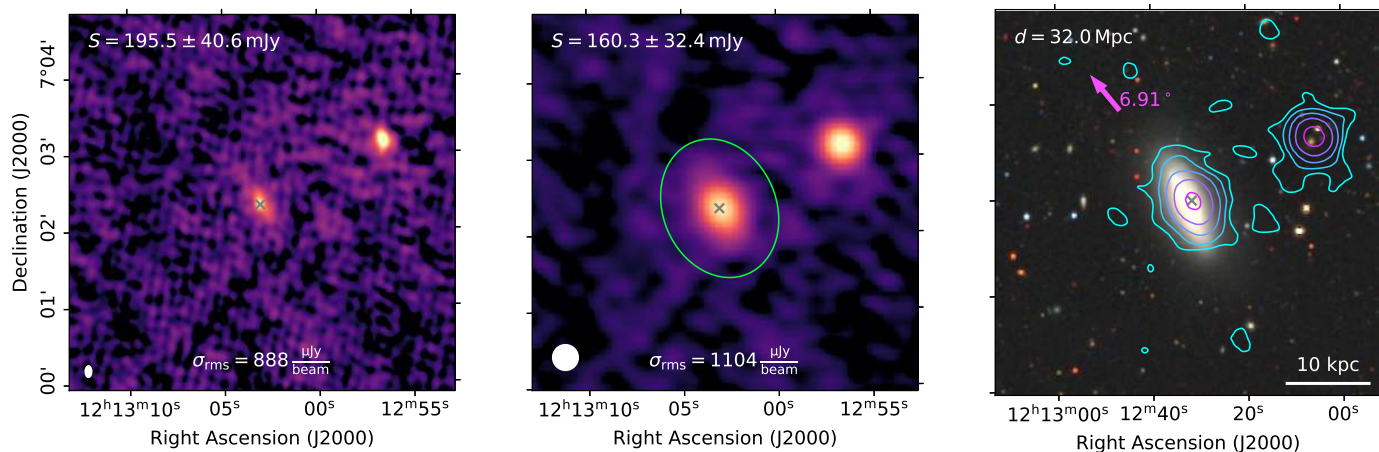
(a)

NGC 4189 / IC 3050 / VCC 89
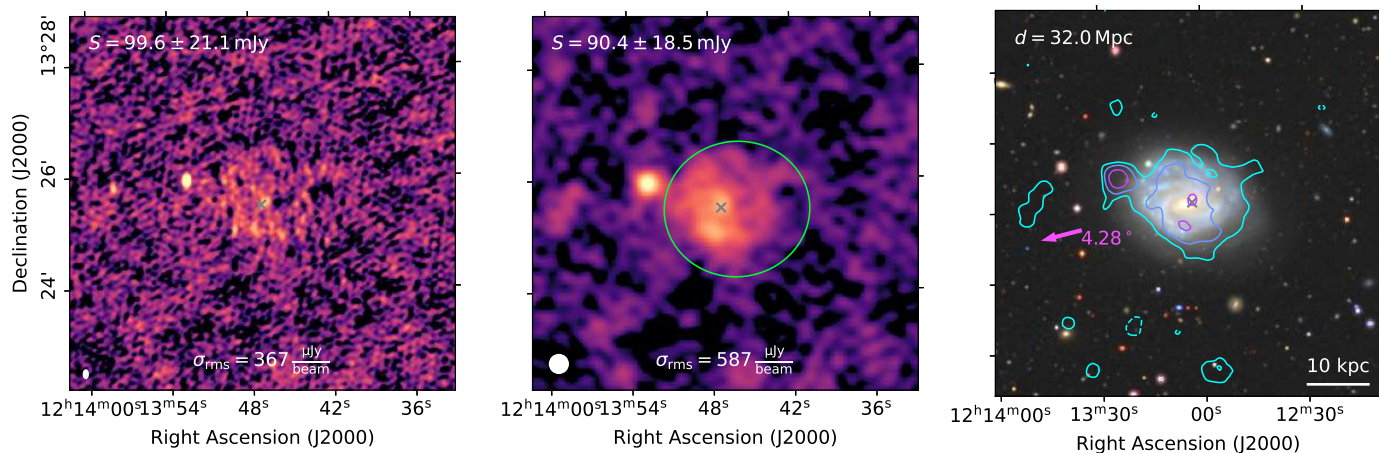
(b)

NGC 4197 / VCC 120

(c)

Fig. A.2: Same as Figure A.1.

IC 3061 / VCC 131

$S = 16.3 \pm 4.3\,\mathrm{mJy}$

$\sigma_{\mathrm{rms}} = 398\,\frac{\mu\mathrm{Jy}}{\mathrm{beam}}$

$S = 11.7 \pm 2.8\,\mathrm{mJy}$

$\sigma_{\mathrm{rms}} = 697\,\frac{\mu\mathrm{Jy}}{\mathrm{beam}}$

$d = 32.0\,\mathrm{Mpc}$

4.17°

10 kpc

(a)

VCC 144

$S = 4.3 \pm 3.2\,\mathrm{mJy}$

$\sigma_{\mathrm{rms}} = 704\,\frac{\mu\mathrm{Jy}}{\mathrm{beam}}$

$S = 6.1 \pm 1.8\,\mathrm{mJy}$

$\sigma_{\mathrm{rms}} = 901\,\frac{\mu\mathrm{Jy}}{\mathrm{beam}}$

$d = 32.0\,\mathrm{Mpc}$

7.66°

10 kpc

(b)

NGC 4208 / VCC 157

$S = 135.3 \pm 27.7\,\mathrm{mJy}$

$\sigma_{\mathrm{rms}} = 309\,\frac{\mu\mathrm{Jy}}{\mathrm{beam}}$

$S = 126.6 \pm 25.5\,\mathrm{mJy}$

$\sigma_{\mathrm{rms}} = 462\,\frac{\mu\mathrm{Jy}}{\mathrm{beam}}$

$d = 16.5\,\mathrm{Mpc}$

3.99°

10 kpc

(c)
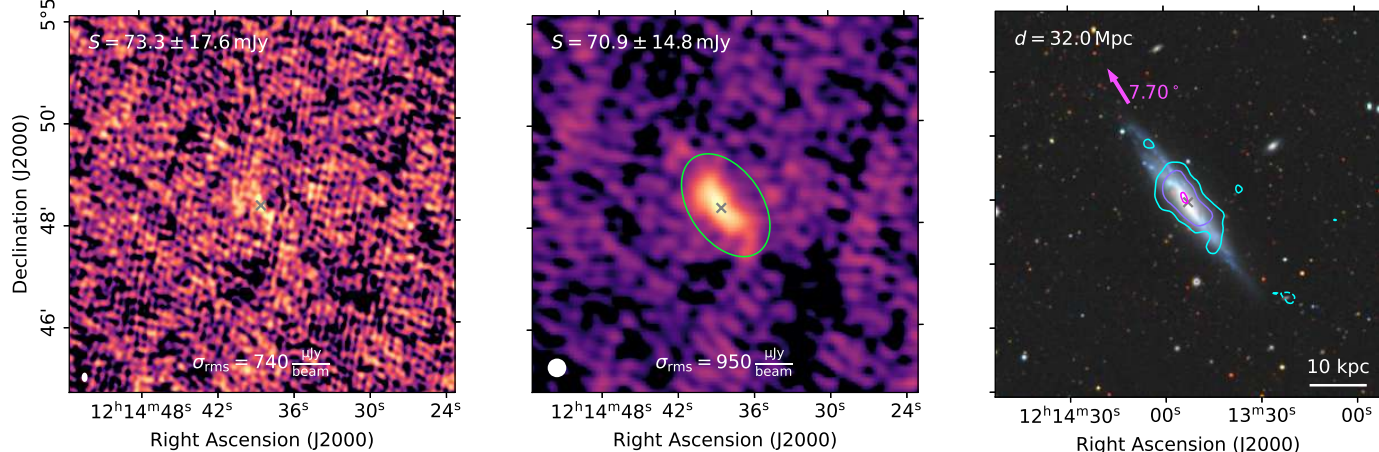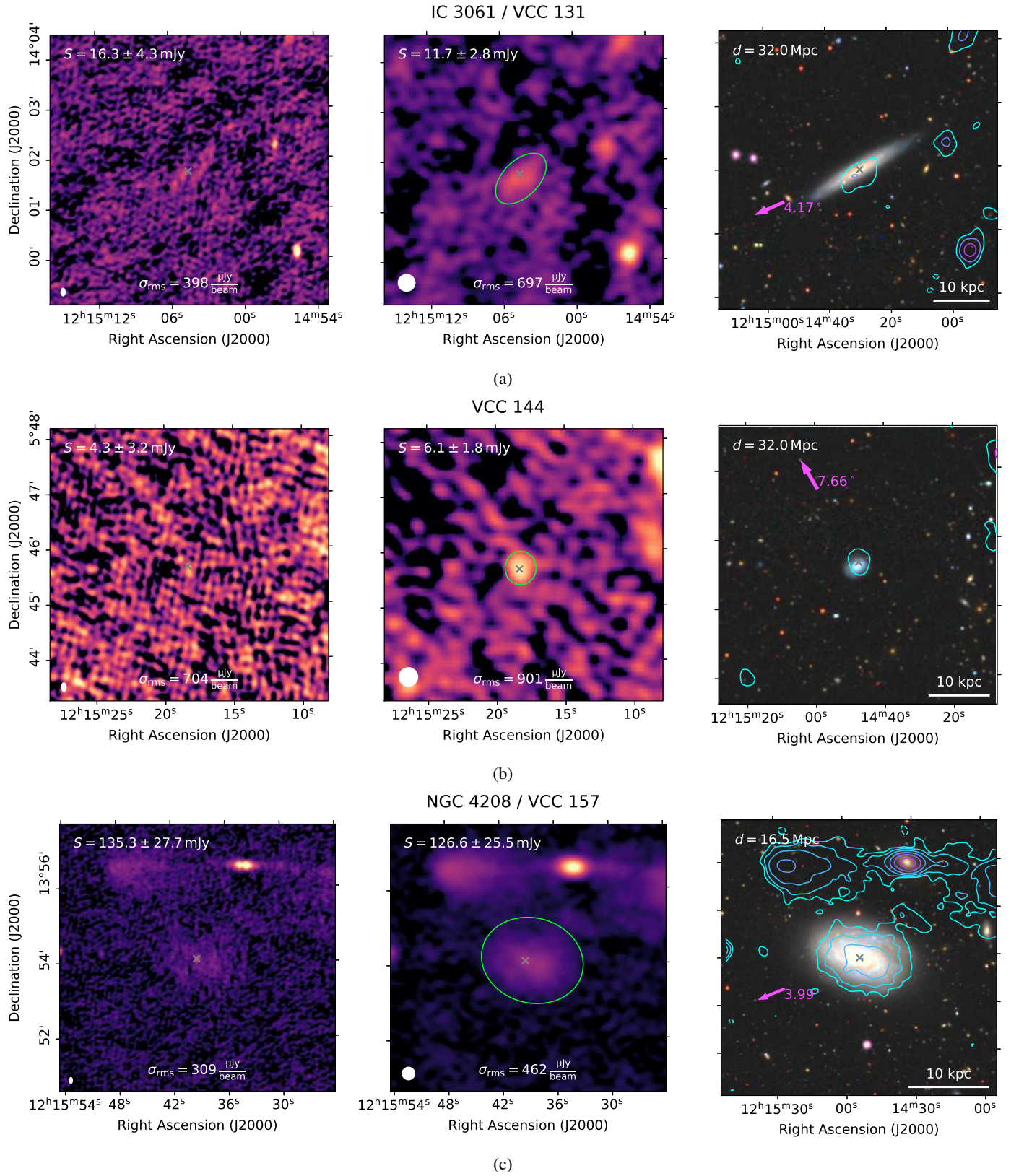
Fig. A.3: Same as Figure A.1.

NGC 4216 / VCC 167
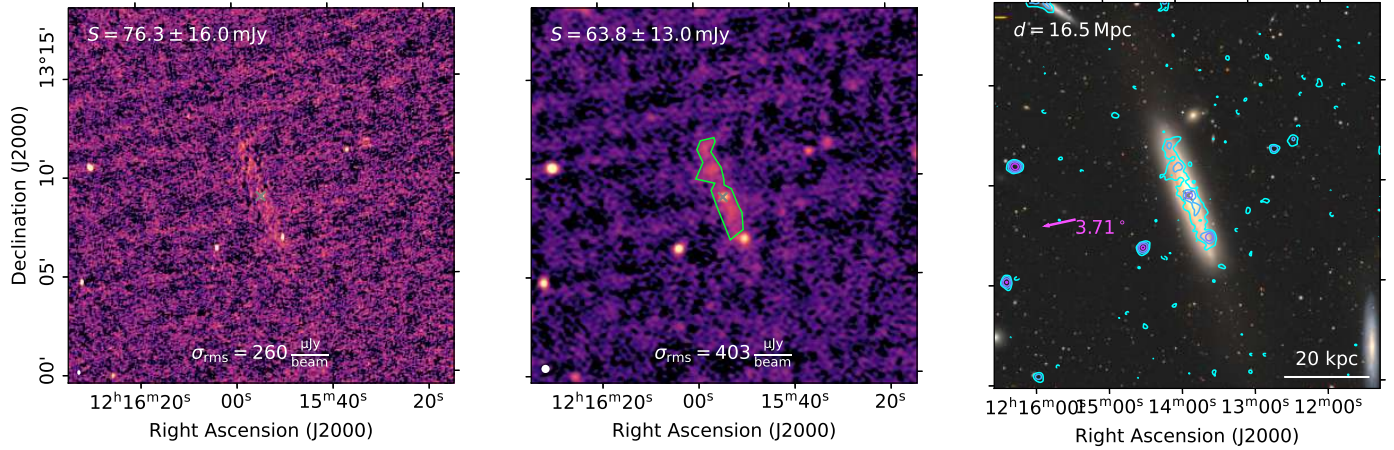
(a)

NGC 4222 / IC 3087 / VCC 187
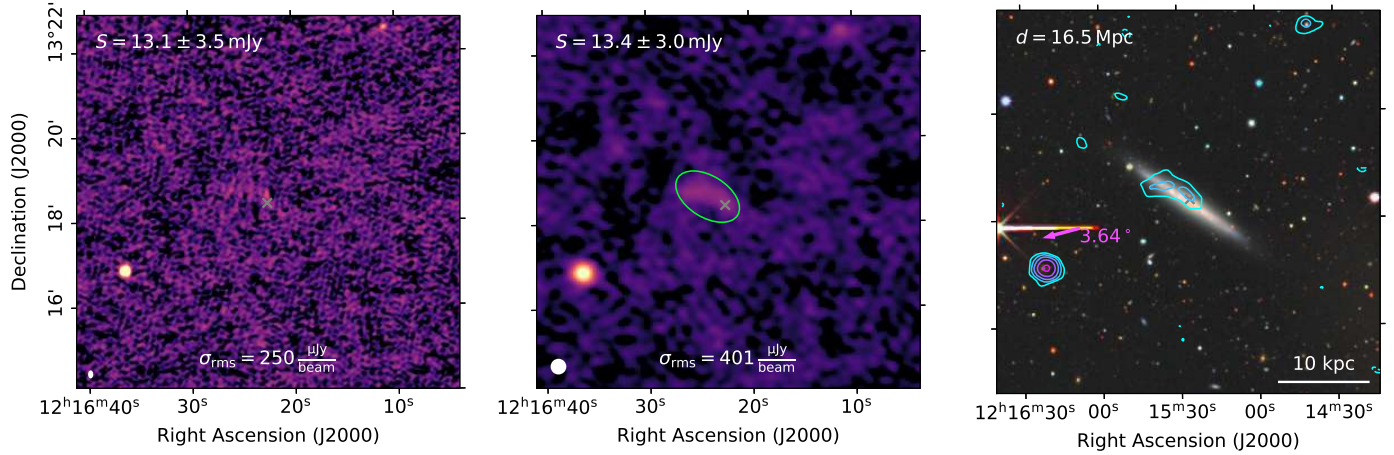
(b)

NGC 4224 / VCC 199

(c)

Fig. A.4: Same as Figure A.1.

NGC 4235 / IC 3098 / VCC 222

(a)

NGC 4237 / VCC 226

(b)

IC 3105 / VCC 241

(c)
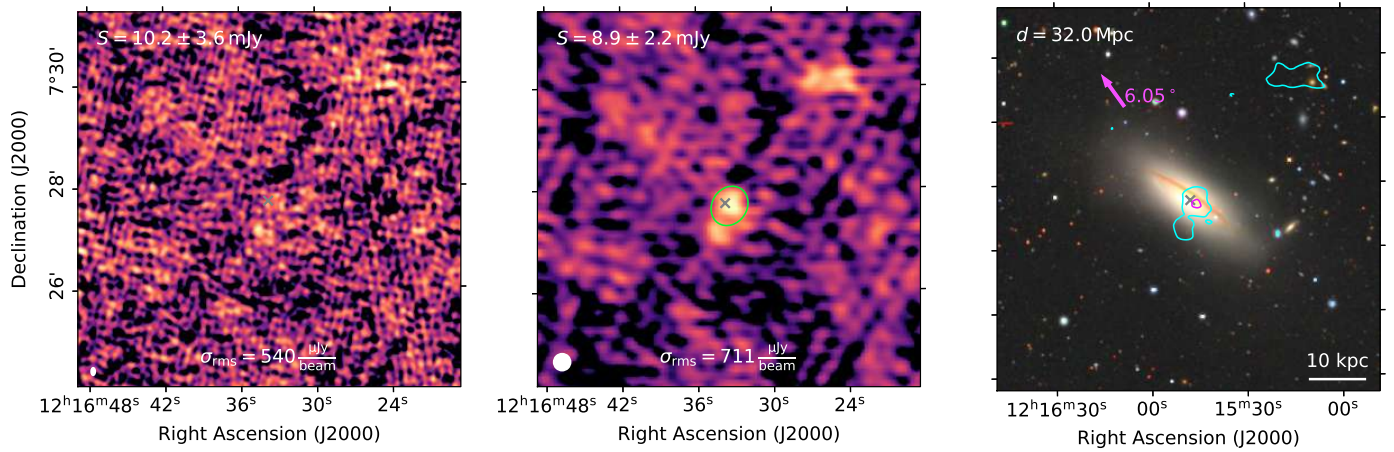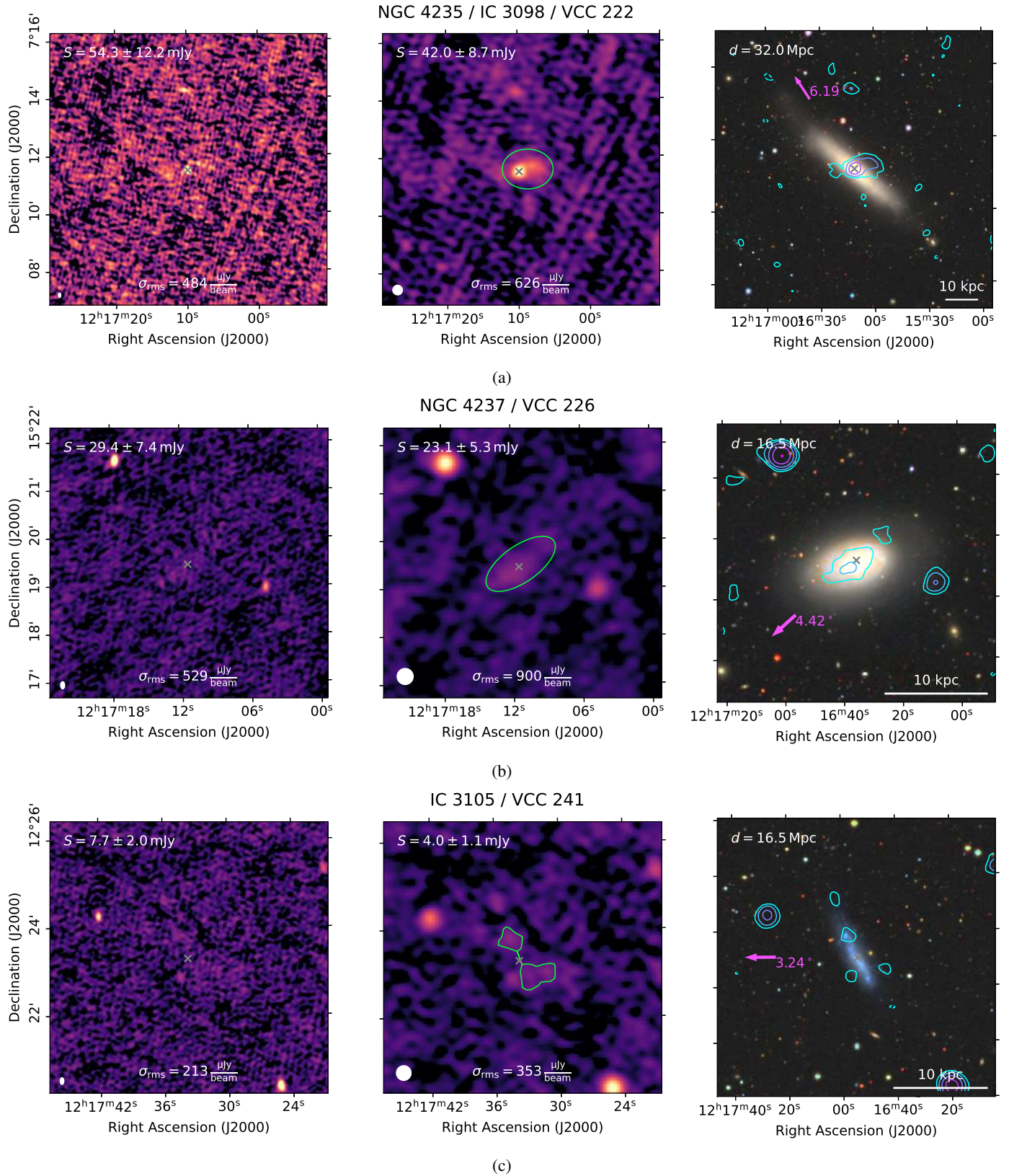
Fig. A.5: Same as Figure A.1.

NGC 4254 / VCC 307

NGC 4261 / VCC 345

NGC 4273 / VCC 382

Fig. A.6: Same as Figure A.1.

NGC 4289 / VCC 449

(a)

NGC 4294 / VCC 465

(b)

NGC 4298 / VCC 483

(c)
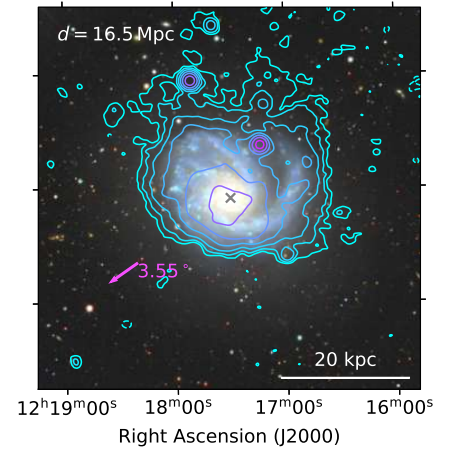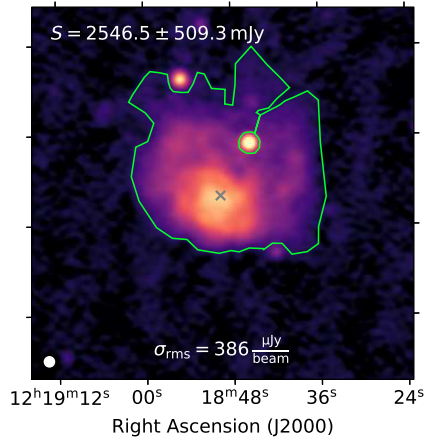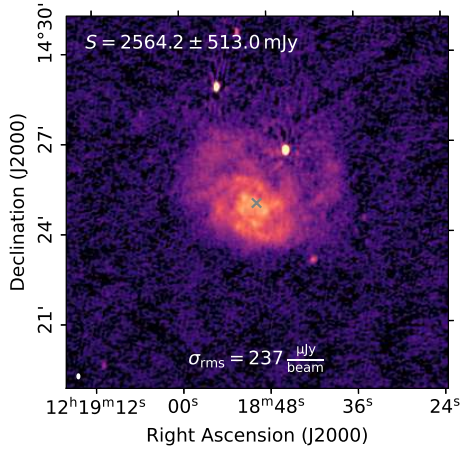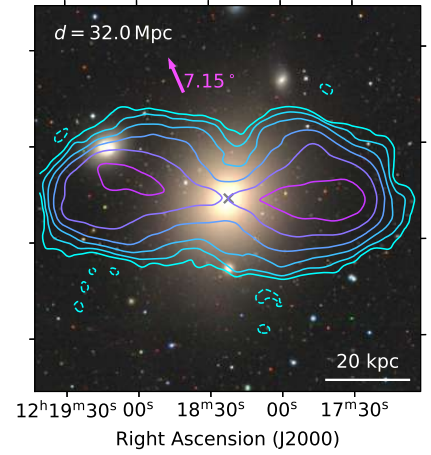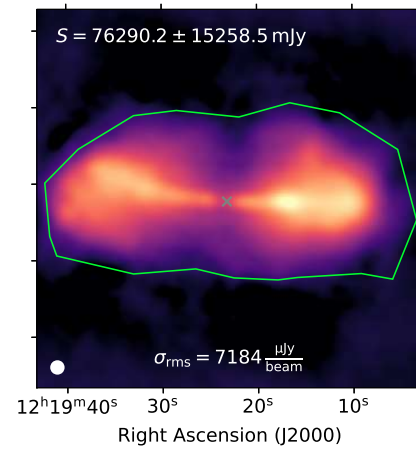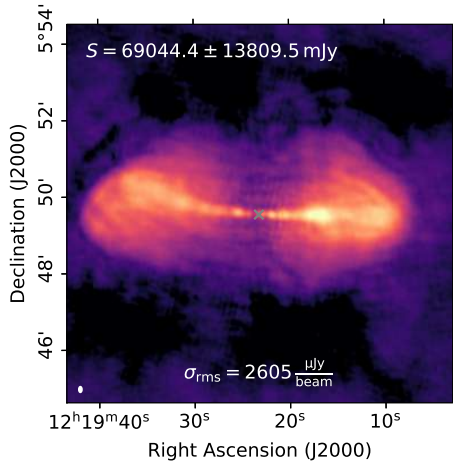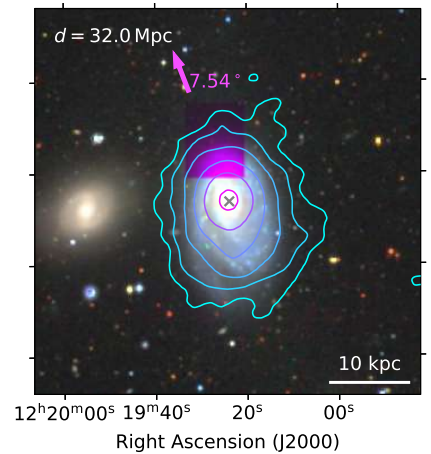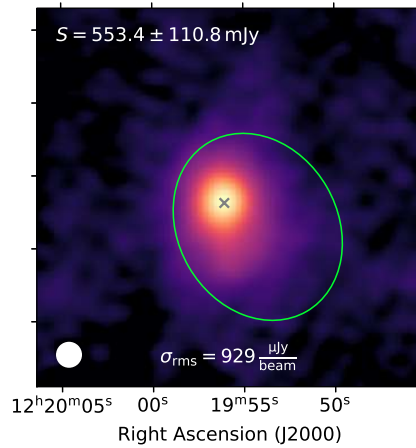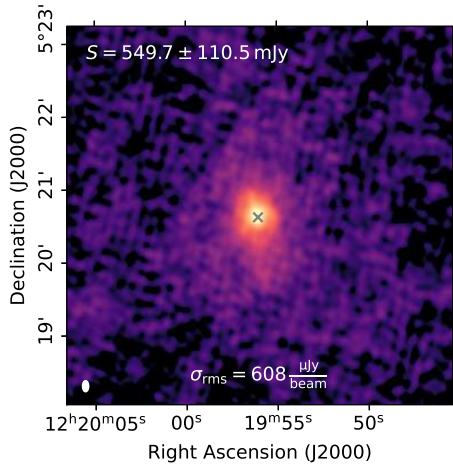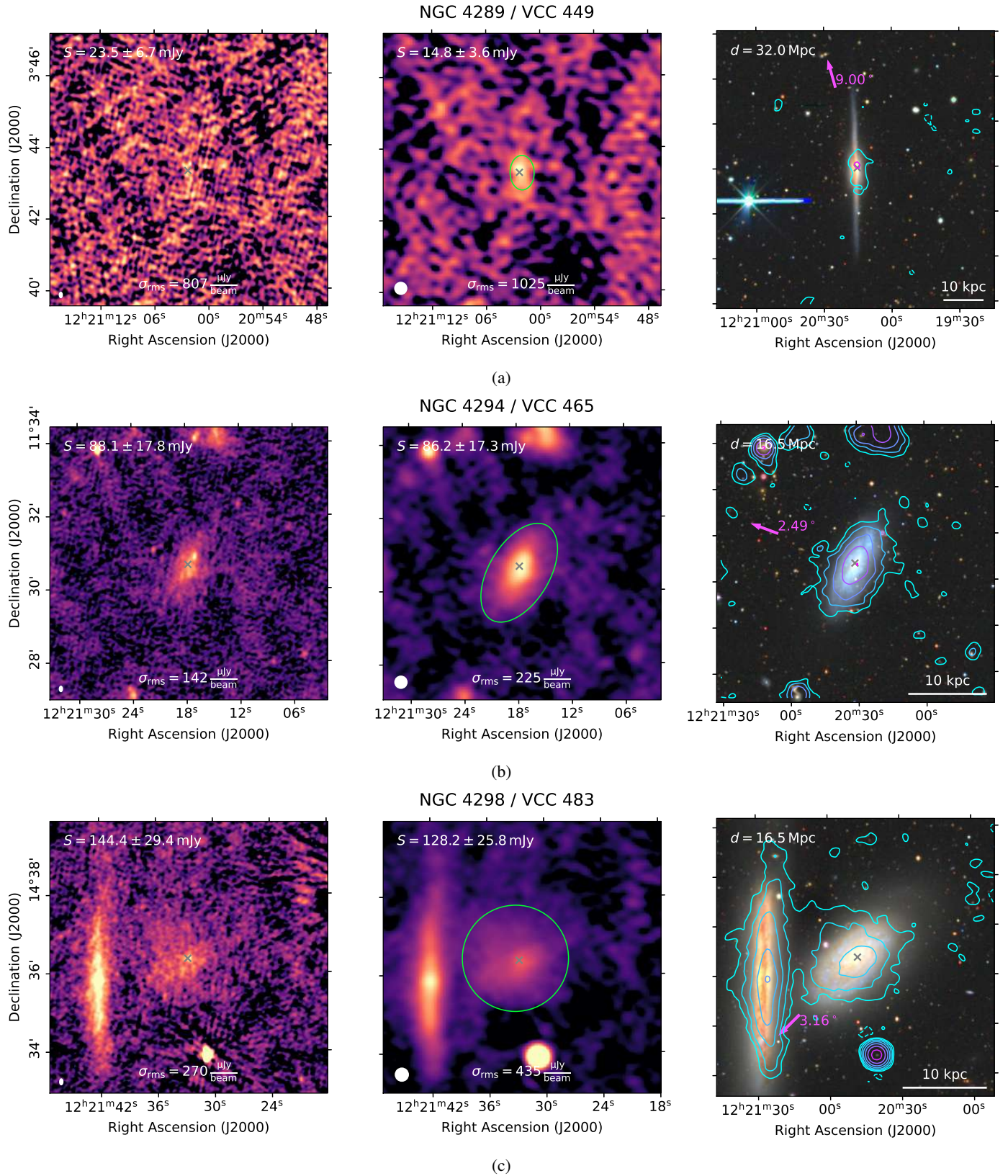
Fig. A.7: Same as Figure A.1.

NGC 4299 / VCC 491
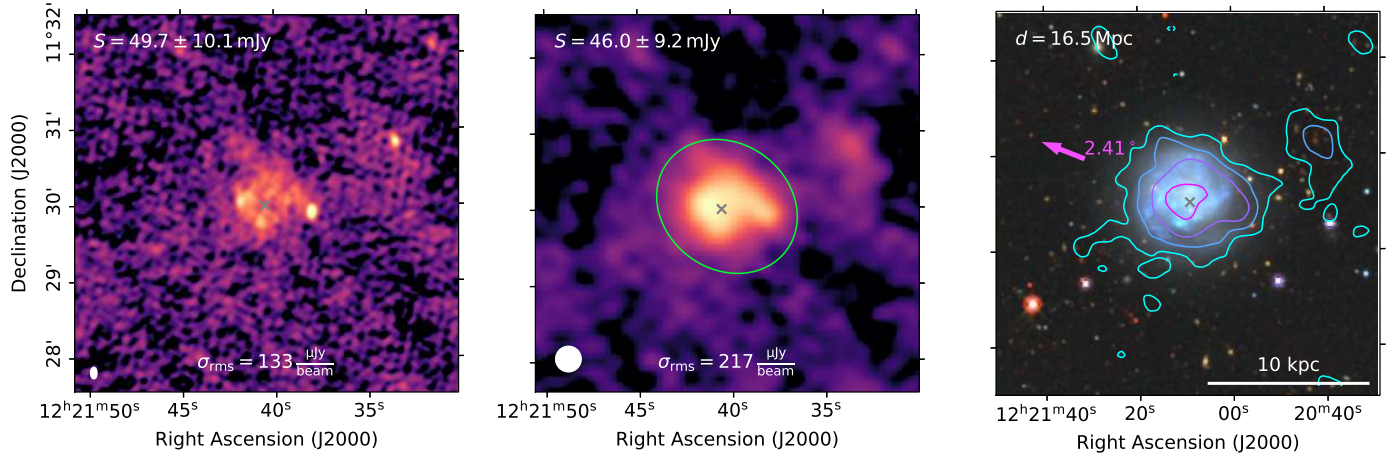
(a)

NGC 4302 / VCC 497
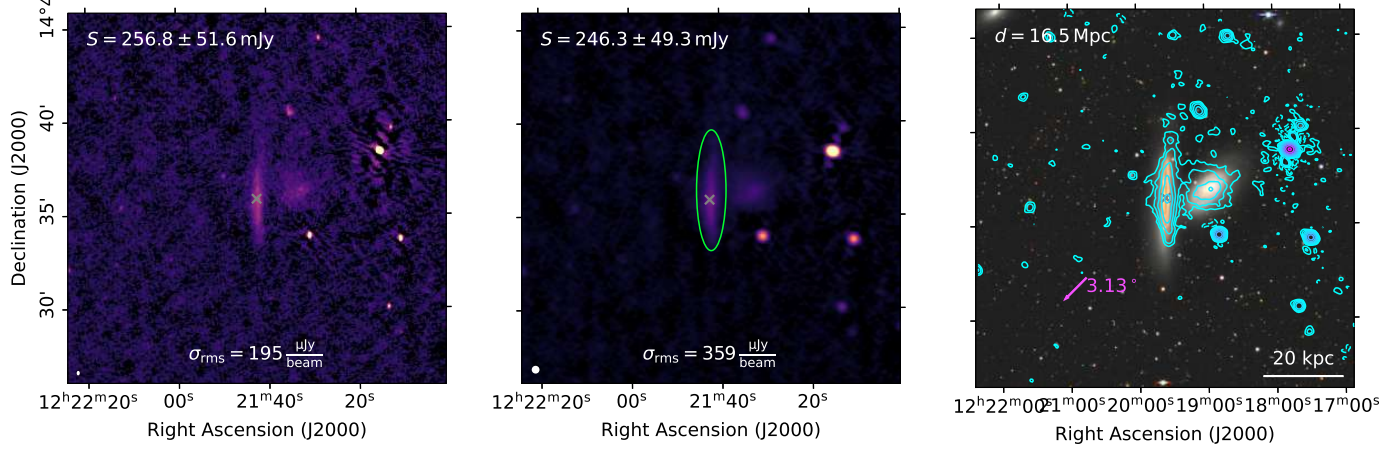
(b)

NGC 4303 / VCC 508

(c)

Fig. A.8: Same as Figure A.1.

NGC 4307 / VCC 524

$S = 10.0 \pm 2.7$ mJy

$\sigma_{rms} = 198 \frac{\mu Jy}{beam}$

$S = 9.5 \pm 2.1$ mJy

$\sigma_{rms} = 333 \frac{\mu Jy}{beam}$

$d = 23.0$ Mpc

3.98°

10 kpc

(a)

NGC 4312 / VCC 559

$S = 38.3 \pm 7.9$ mJy

$\sigma_{rms} = 224 \frac{\mu Jy}{beam}$

$S = 35.7 \pm 7.2$ mJy

$\sigma_{rms} = 373 \frac{\mu Jy}{beam}$

$d = 16.5$ Mpc

3.74°

20 kpc

(b)

NGC 4313 / VCC 570

$S = 4.6 \pm 1.2$ mJy

$\sigma_{rms} = 121 \frac{\mu Jy}{beam}$

$S = 3.9 \pm 0.9$ mJy

$\sigma_{rms} = 209 \frac{\mu Jy}{beam}$

$d = 16.5$ Mpc

2.09°

20 kpc

(c)
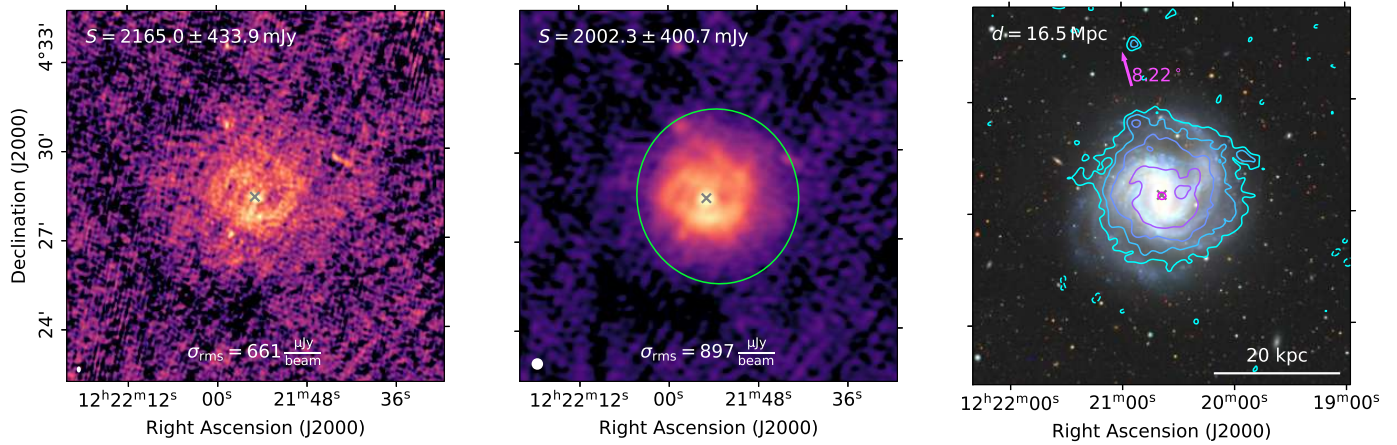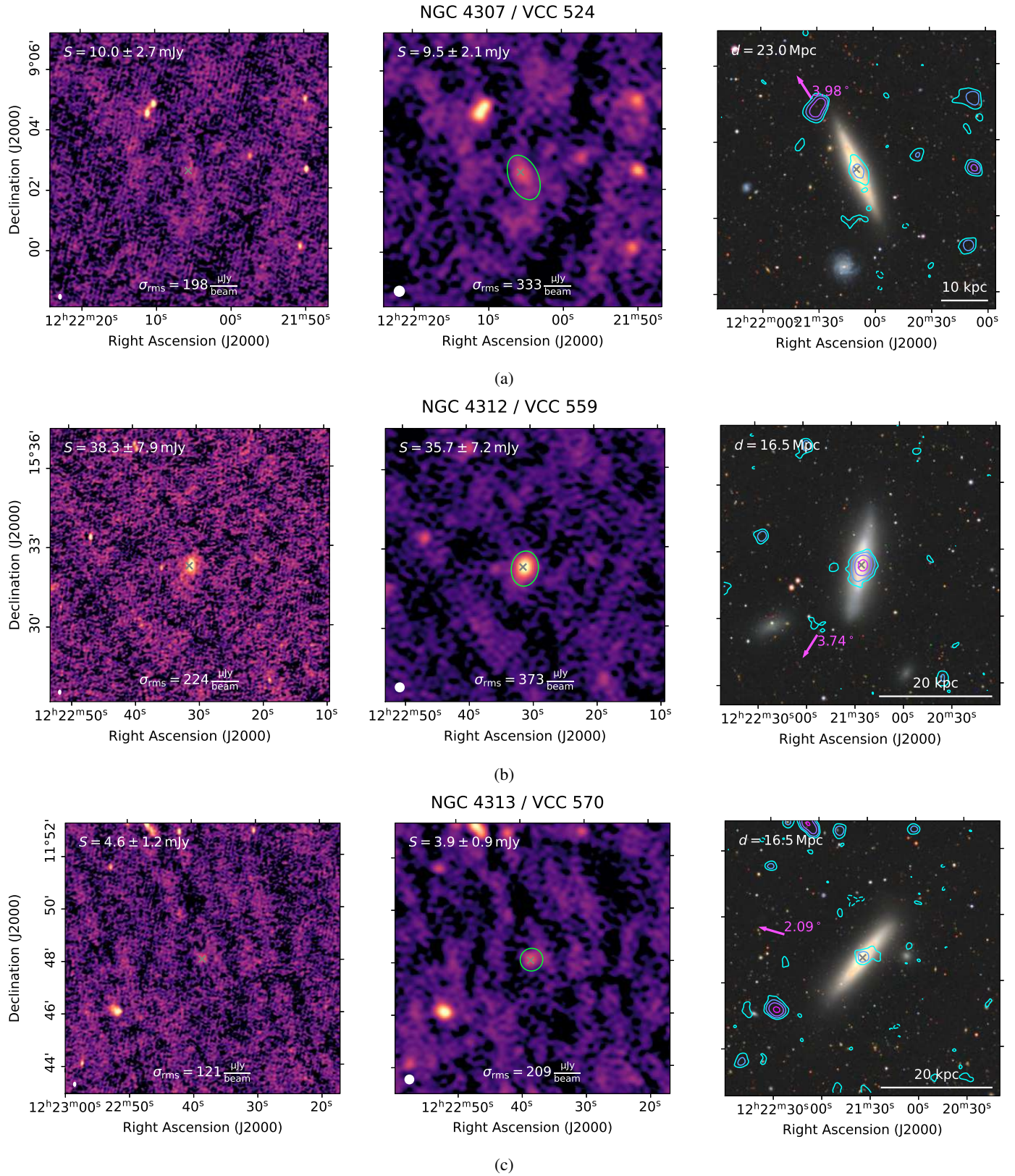
Fig. A.9: Same as Figure A.1.

NGC 4316 / VCC 576
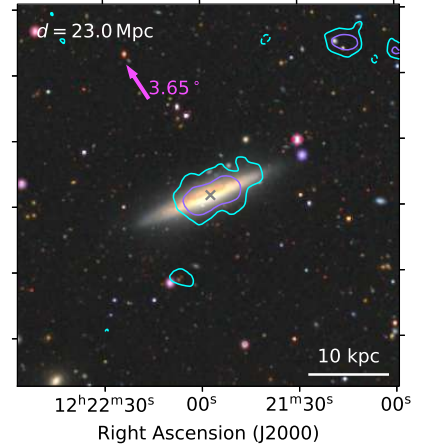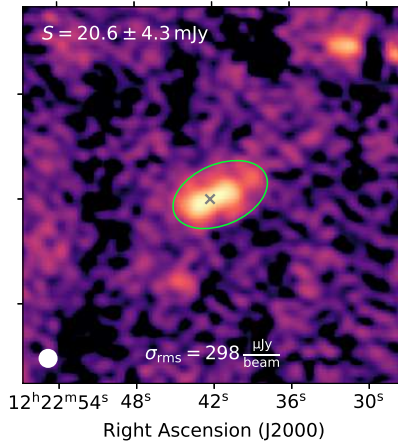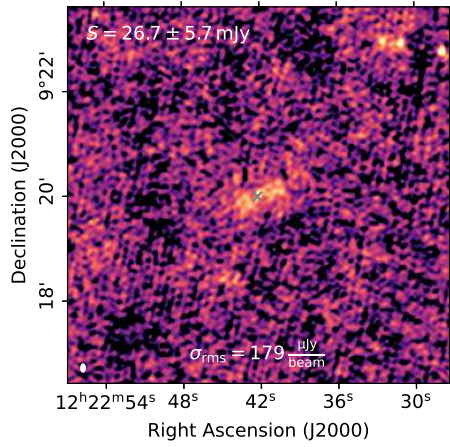
(a)

NGC 4321 / VCC 596
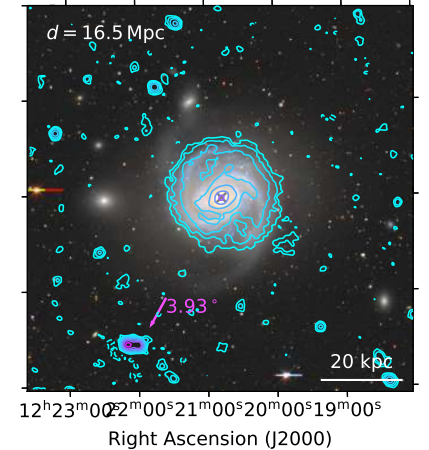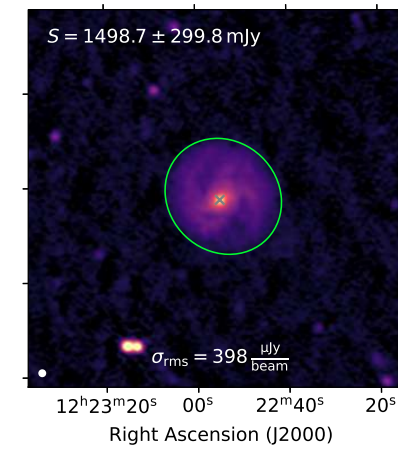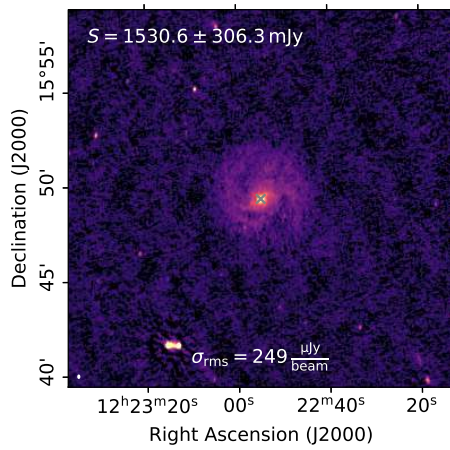
(b)

NGC 4330 / VCC 630
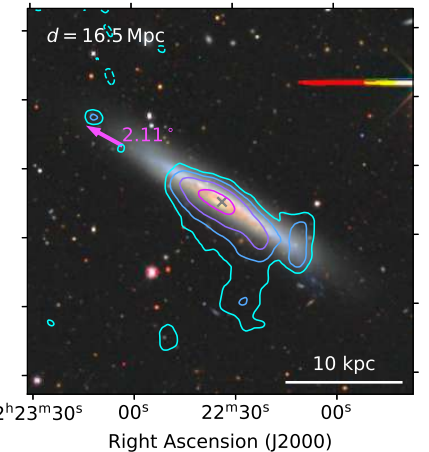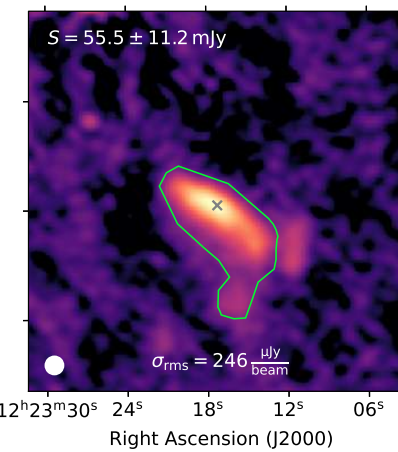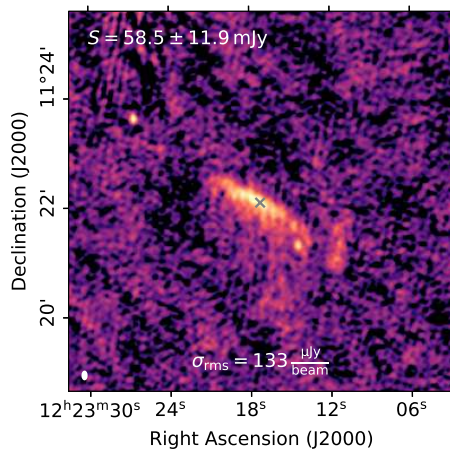
(c)

Fig. A.10: Same as Figure A.1.

NGC 4343 / VCC 656

(a)

IC 3258 / VCC 664

(b)

NGC 4351 / VCC 692

(c)
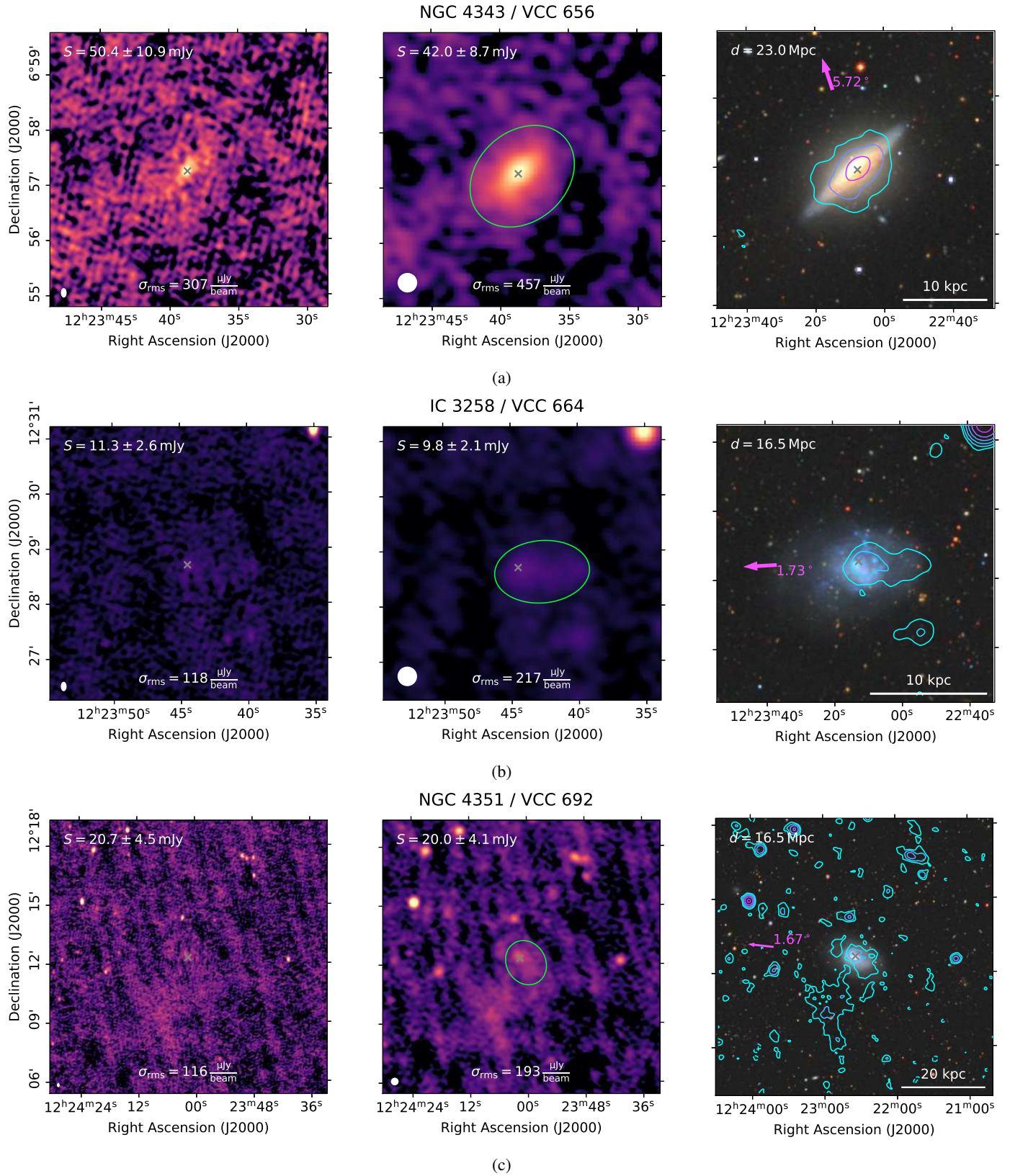
Fig. A.11: Same as Figure A.1.

IC 3268 / VCC 699

NGC 4370 / VCC 758

NGC 4374 / VCC 763

Fig. A.12: Same as Figure A.1.

NGC 4376 / VCC 787

(a)

NGC 4380 / VCC 792

(b)

NGC 4383 / VCC 801

(c)
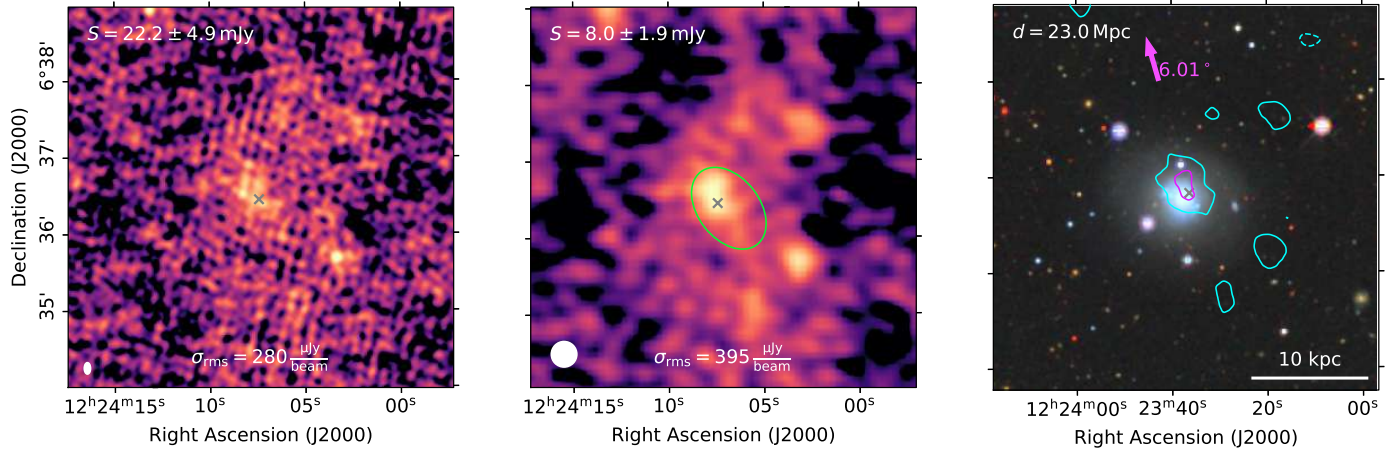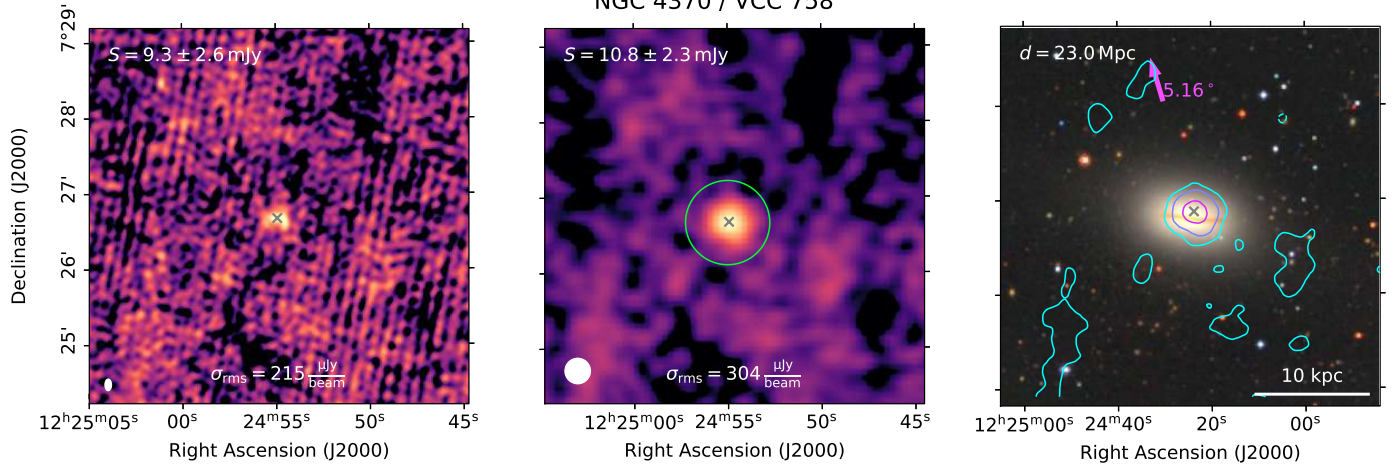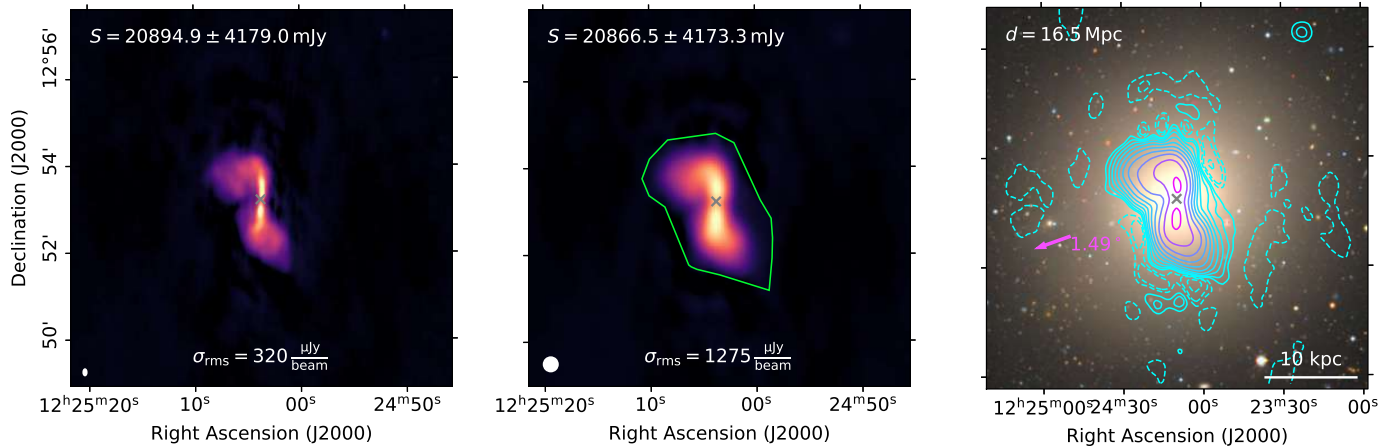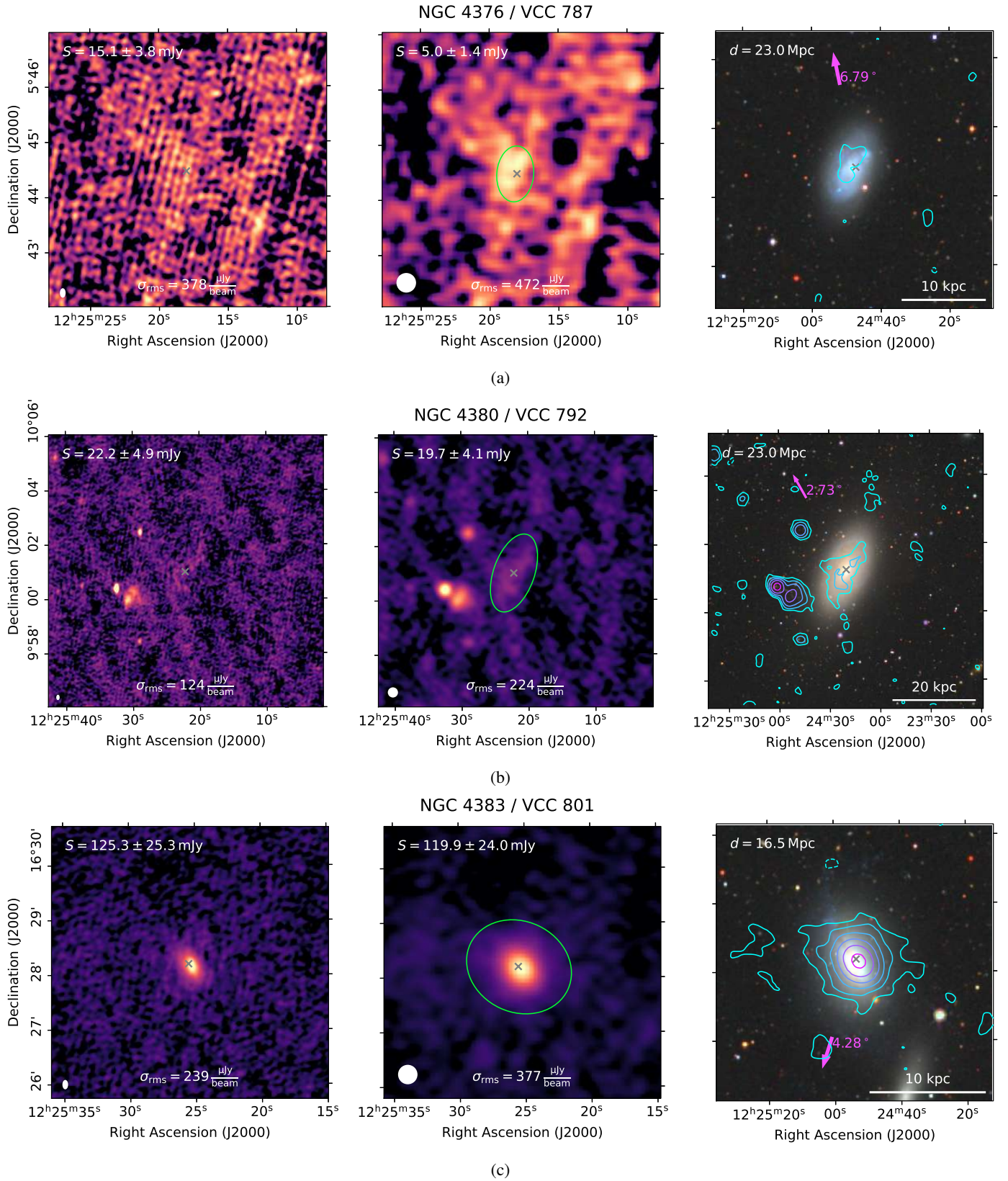
Fig. A.13: Same as Figure A.1.

IC 3322 / VCC 827
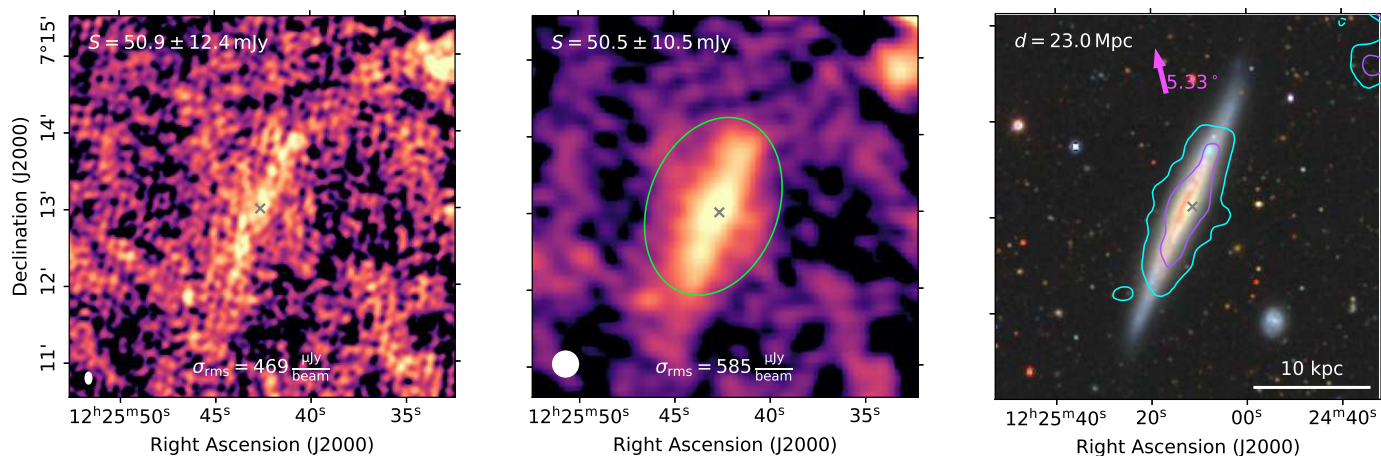
(a)

NGC 4388 / VCC 836
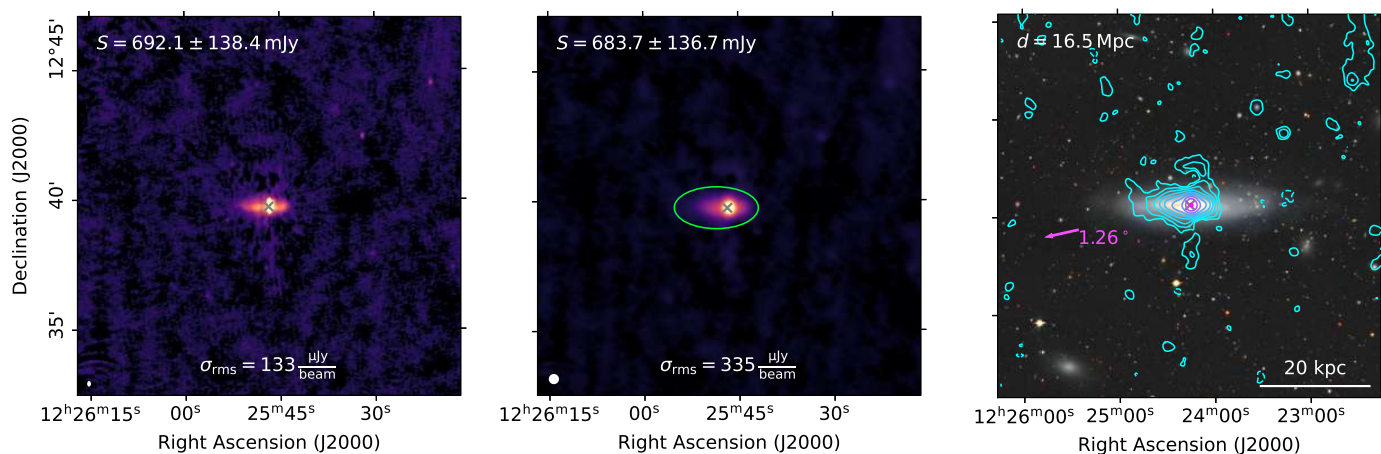
(b)

NGC 4390 / VCC 849
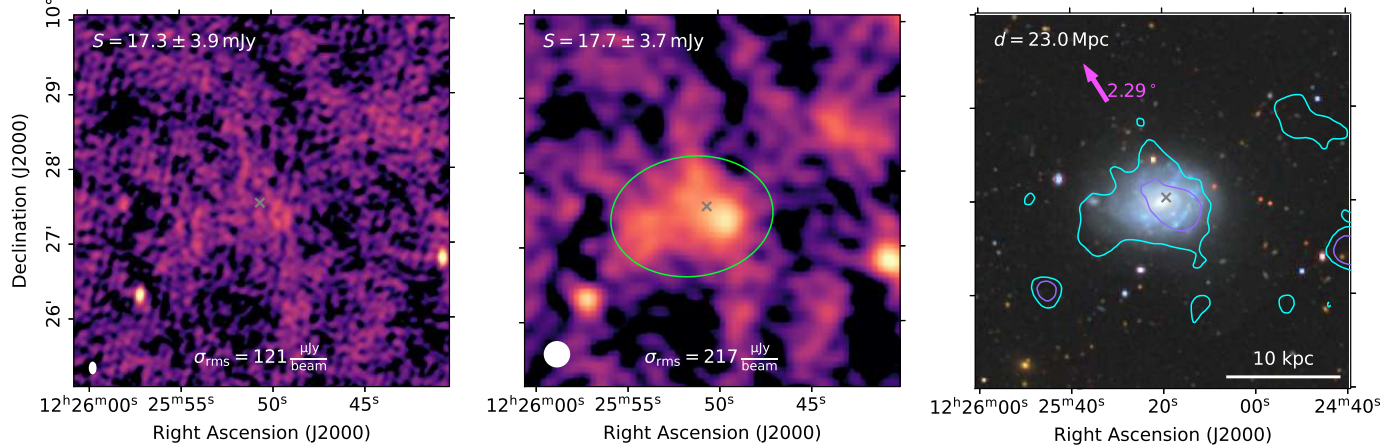
(c)

Fig. A.14: Same as Figure A.1.

IC 3322 / VCC 851

(a)

NGC 4396 / VCC 865

(b)

NGC 4402 / VCC 873

(c)
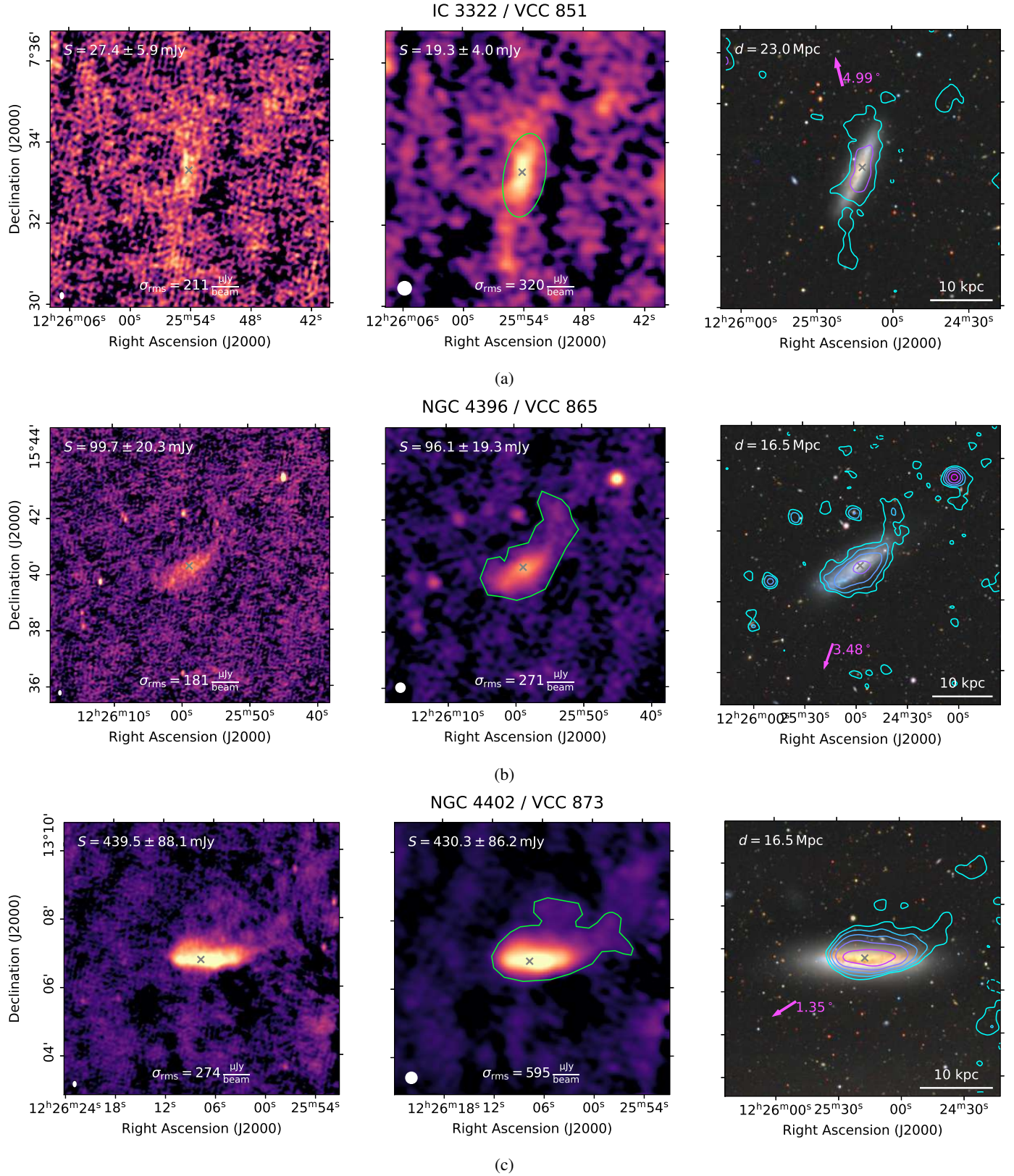
Fig. A.15: Same as Figure A.1.

NGC 4405 / IC 788 / VCC 874
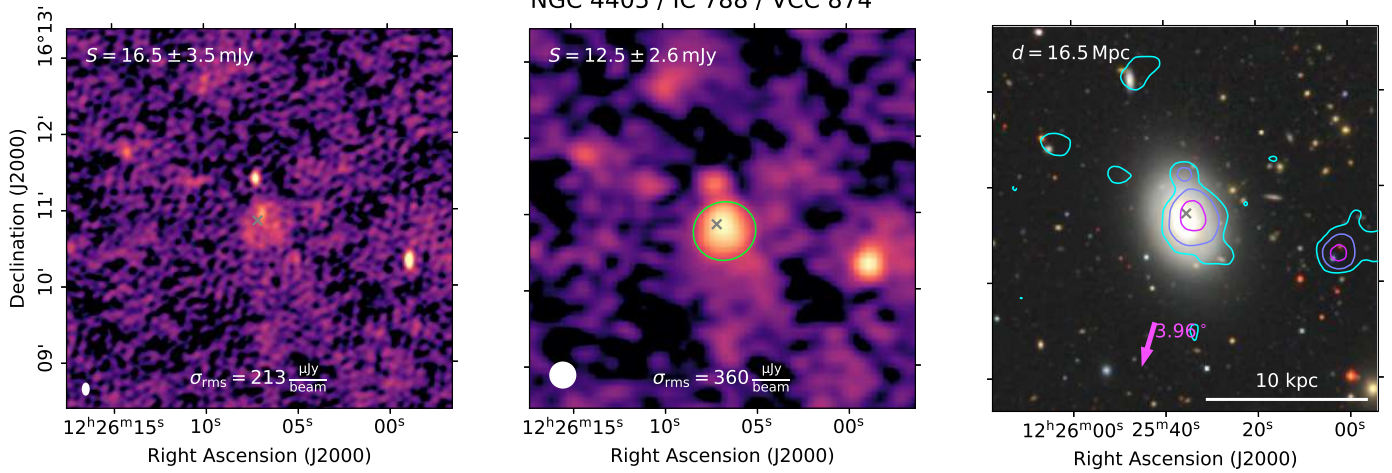
(a)

NGC 4406 / VCC 881
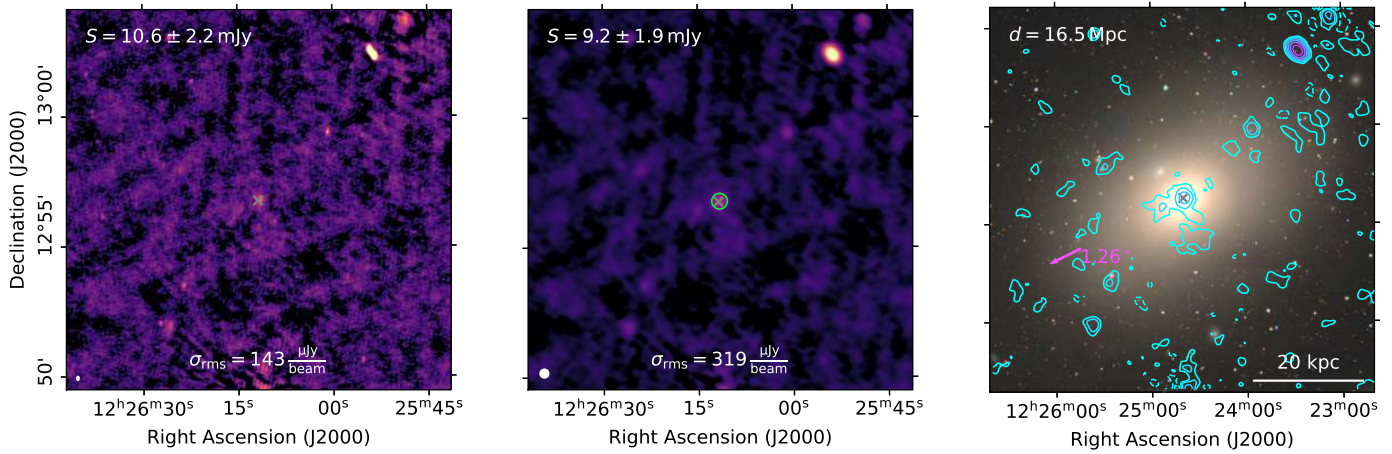
(b)

NGC 4407 / VCC 912
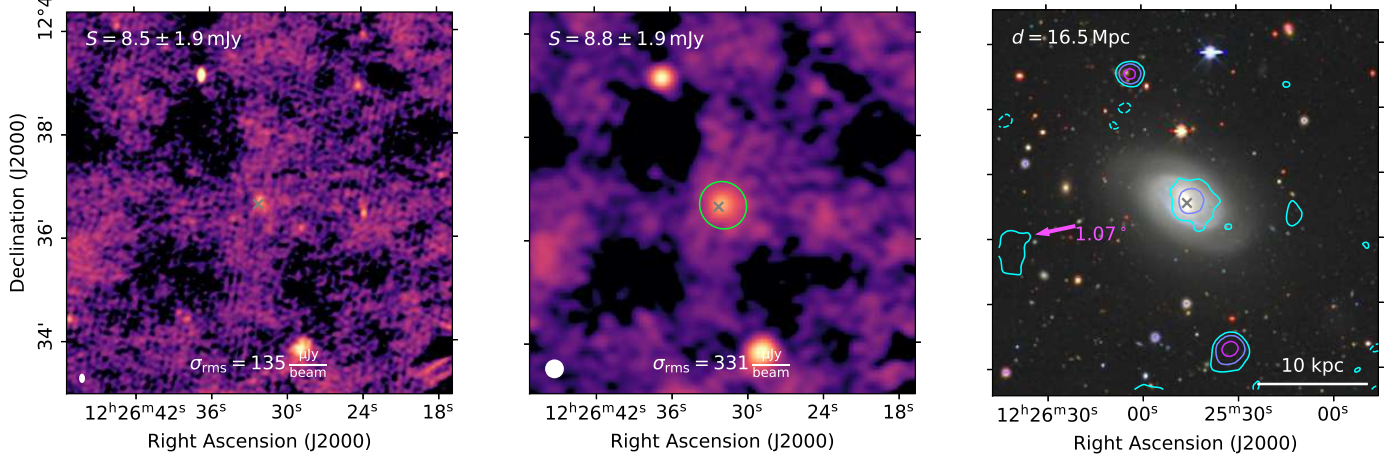
(c)

Fig. A.16: Same as Figure A.1.

NGC 4412 / VCC 921

S = 98.0 ± 21.3 mJy

$\sigma_{rms} = 908 \frac{\mu Jy}{beam}$

S = 40.5 ± 9.0 mJy

$\sigma_{rms} = 1288 \frac{\mu Jy}{beam}$

d = 32.0 Mpc

8.49°

10 kpc

(a)

NGC 4416 / VCC 938

S = 26.6 ± 5.7 mJy

$\sigma_{rms} = 174 \frac{\mu Jy}{beam}$

S = 18.3 ± 3.9 mJy

$\sigma_{rms} = 295 \frac{\mu Jy}{beam}$

d = 16.5 Mpc

4.58°

10 kpc

(b)

NGC 4419 / VCC 958

S = 159.9 ± 32.0 mJy

$\sigma_{rms} = 134 \frac{\mu Jy}{beam}$

S = 155.8 ± 31.2 mJy

$\sigma_{rms} = 247 \frac{\mu Jy}{beam}$

d = 16.5 Mpc

2.82°

10 kpc

(c)

Fig. A.17: Same as Figure A.1.

NGC 4424 / VCC 979

(a)

IC 3365 / VCC 980

(b)

NGC 4429 / VCC 1003

(c)

Fig. A.18: Same as Figure A.1.

NGC 4430 / VCC 1002

(a)

NGC 4435 / VCC 1030

(b)

NGC 4438 / VCC 1043

(c)

Fig. A.19: Same as Figure A.1.

VCC 1091

(a)

NGC 4450 / VCC 1110

(b)

NGC 4451 / VCC 1118

(c)

Fig. A.20: Same as Figure A.1.

IC 3392 / VCC 1126

(a)

NGC 4457 / VCC 1145

(b)

NGC 4459 / VCC 1154

(c)

Fig. A.21: Same as Figure A.1.

NGC 4469 / VCC 1190
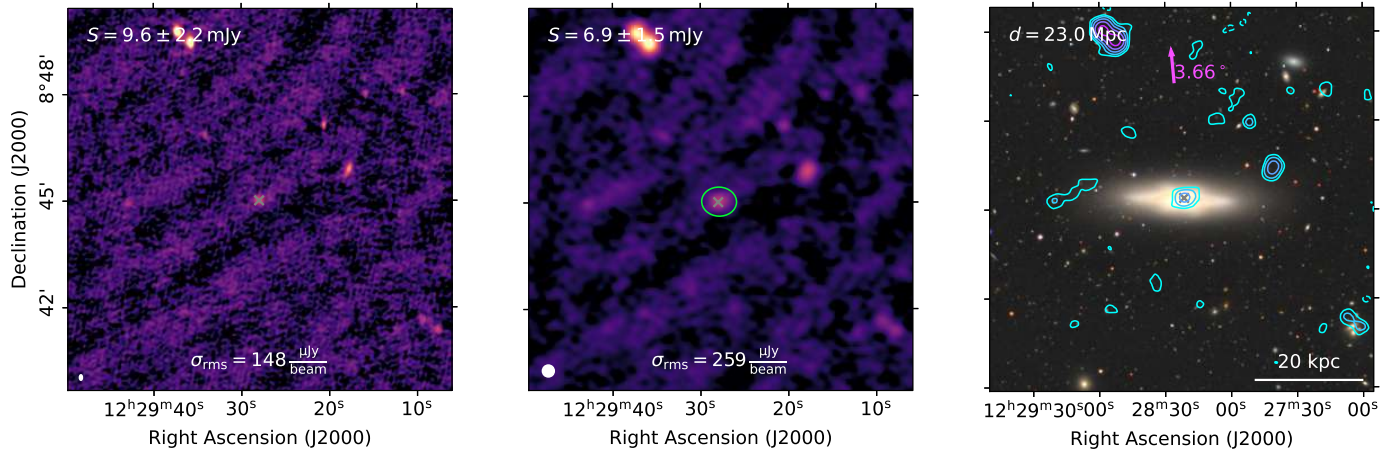
(a)

NGC 4470 / VCC 1205
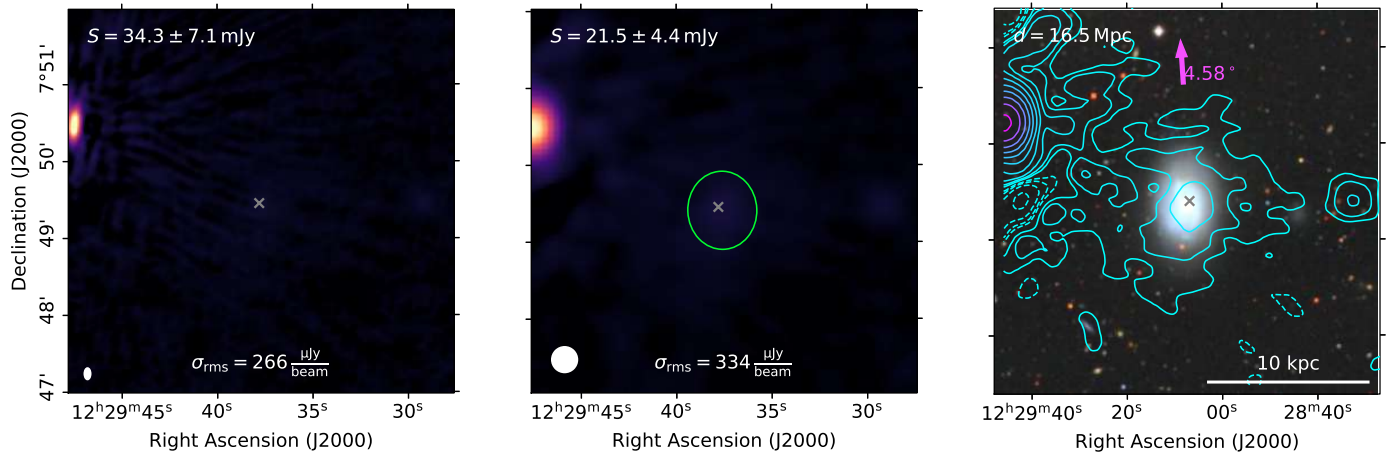
(b)

NGC 4472 / VCC 1226
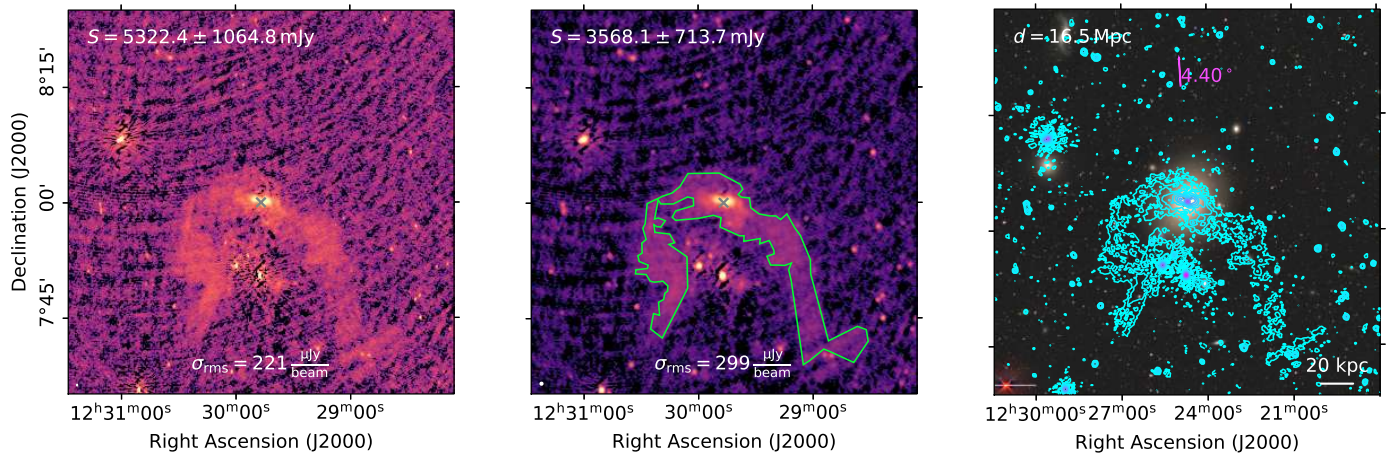
(c)

Fig. A.22: Same as Figure A.1.

NGC 4477 / VCC 1253

(a)

NGC 4480 / VCC 1290

(b)

NGC 4486 / VCC 1316

(c)
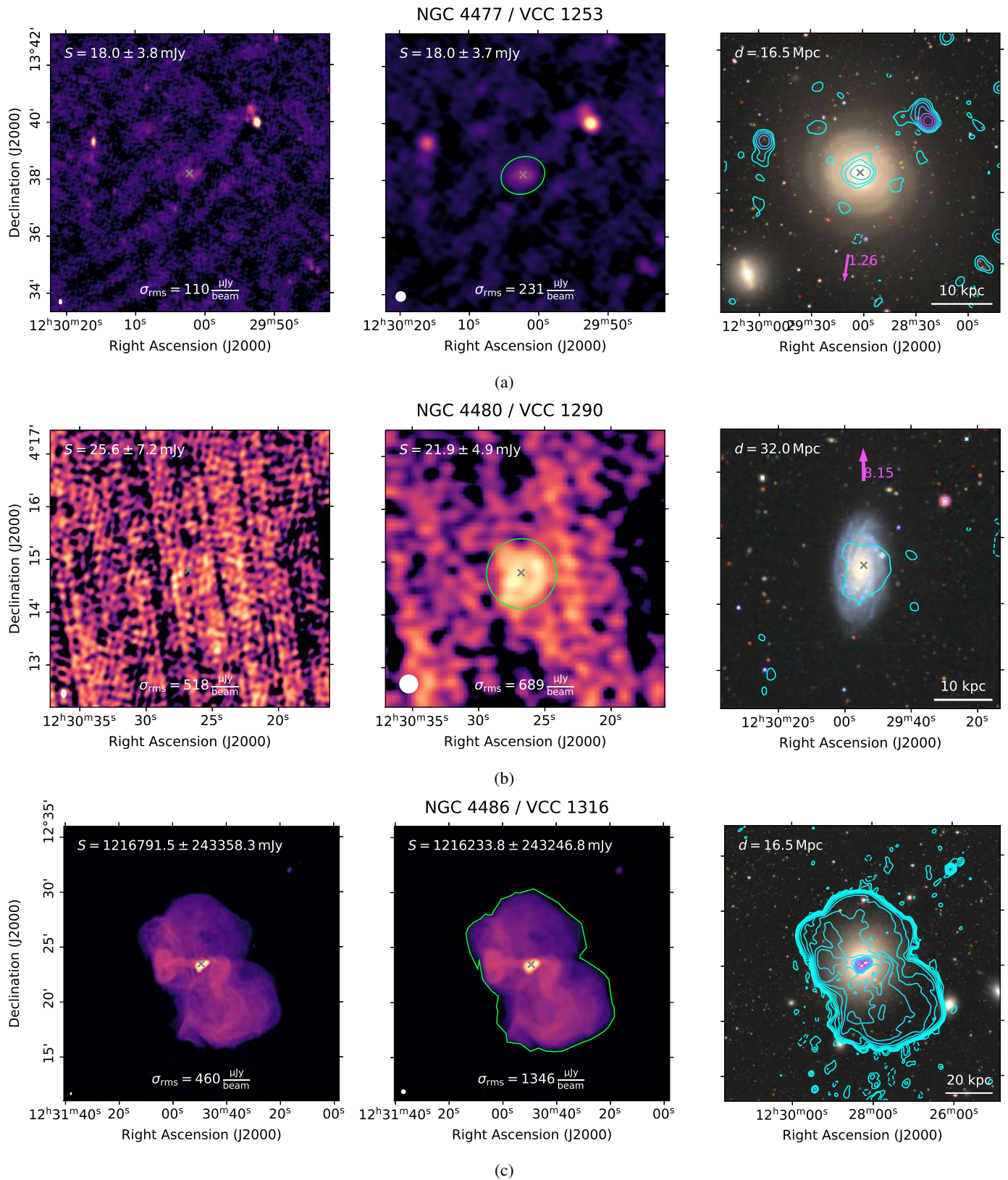
Fig. A.23: Same as Figure A.1.

NGC 4491 / VCC 1326
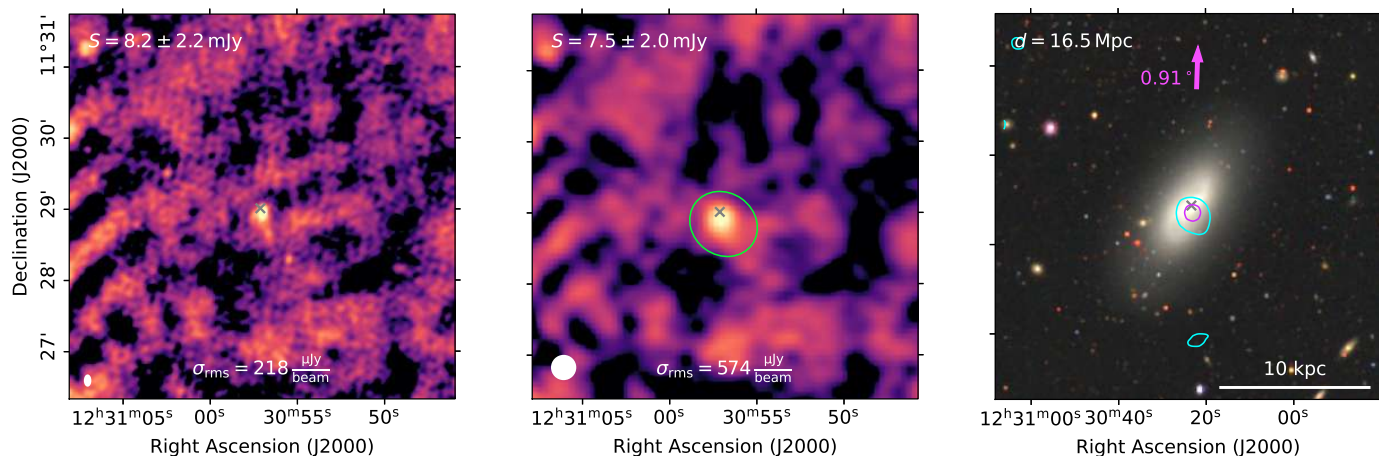
(a)

IC 3453 / VCC 1374
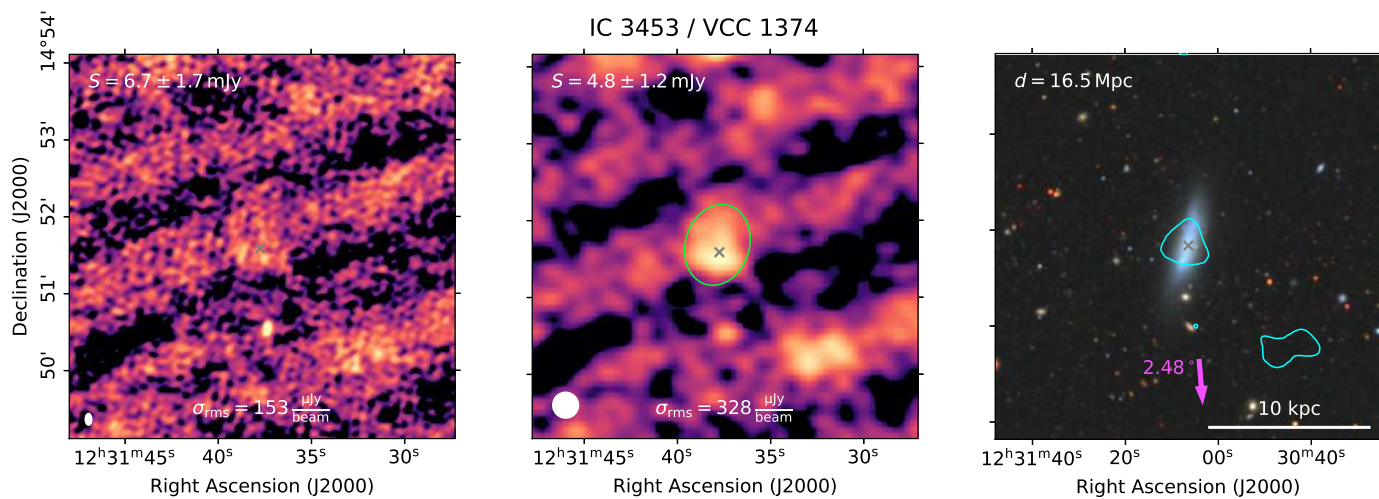
(b)

NGC 4505 / VCC 1375
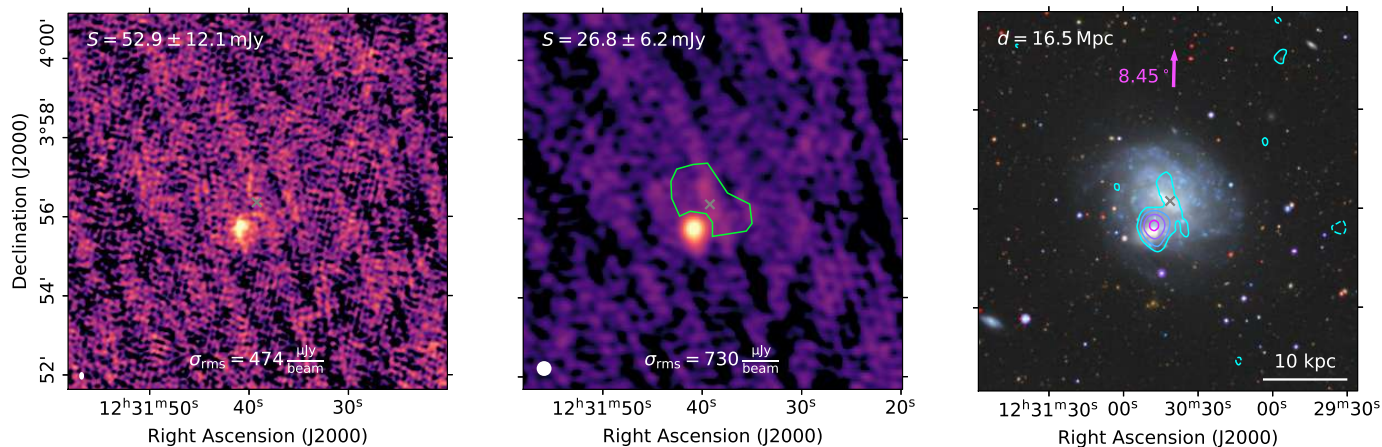
(c)

Fig. A.24: Same as Figure A.1.

IC 797 / VCC 1393

NGC 4501 / VCC 1401

IC 3476 / VCC 1450
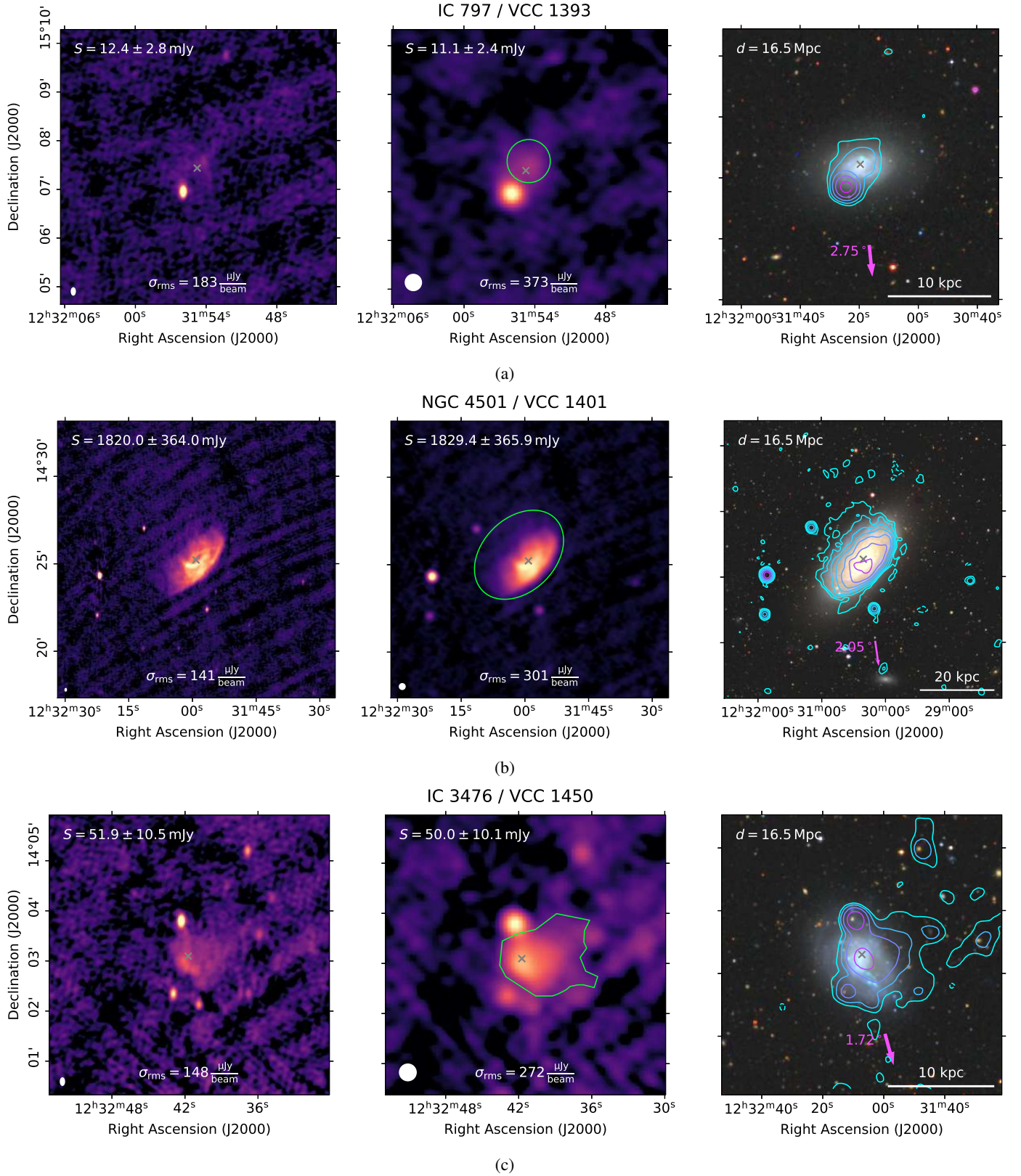
Fig. A.25: Same as Figure A.1.

NGC 4519 / VCC 1508
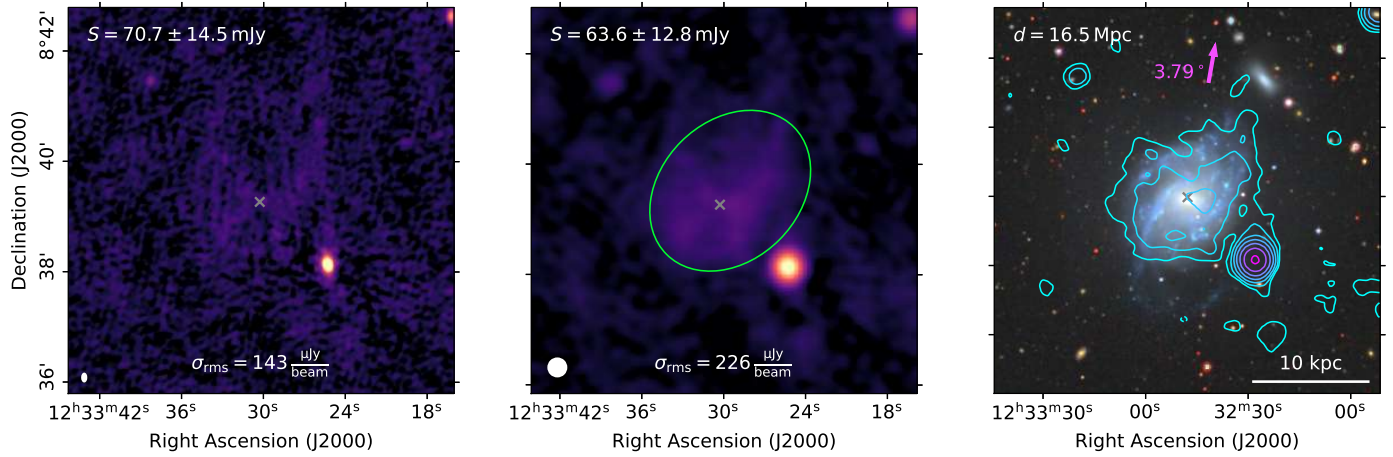
(a)

NGC 4522 / VCC 1516
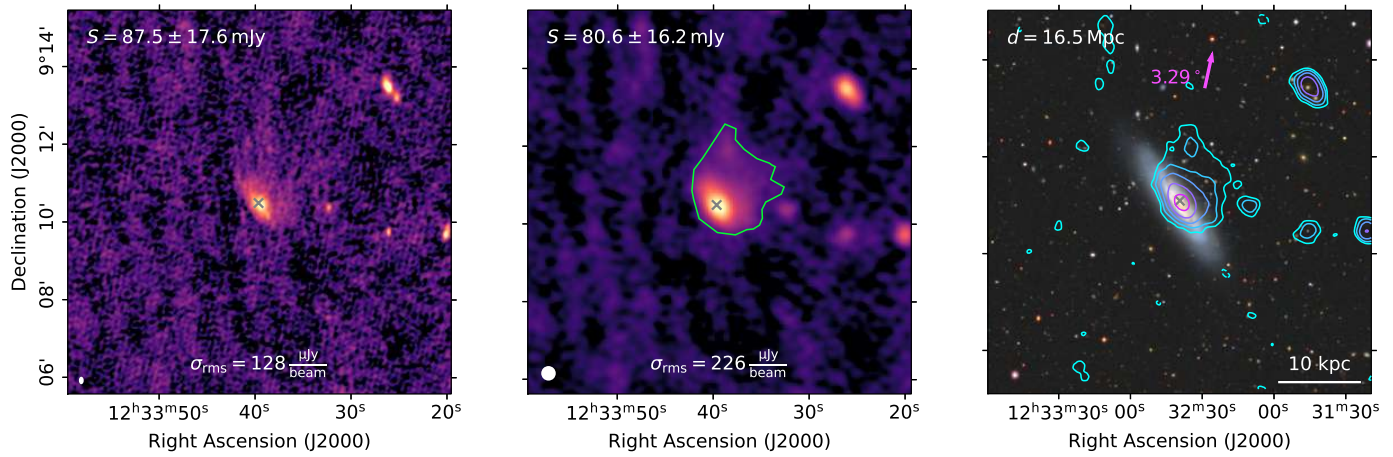
(b)

NGC 4523 / VCC 1524
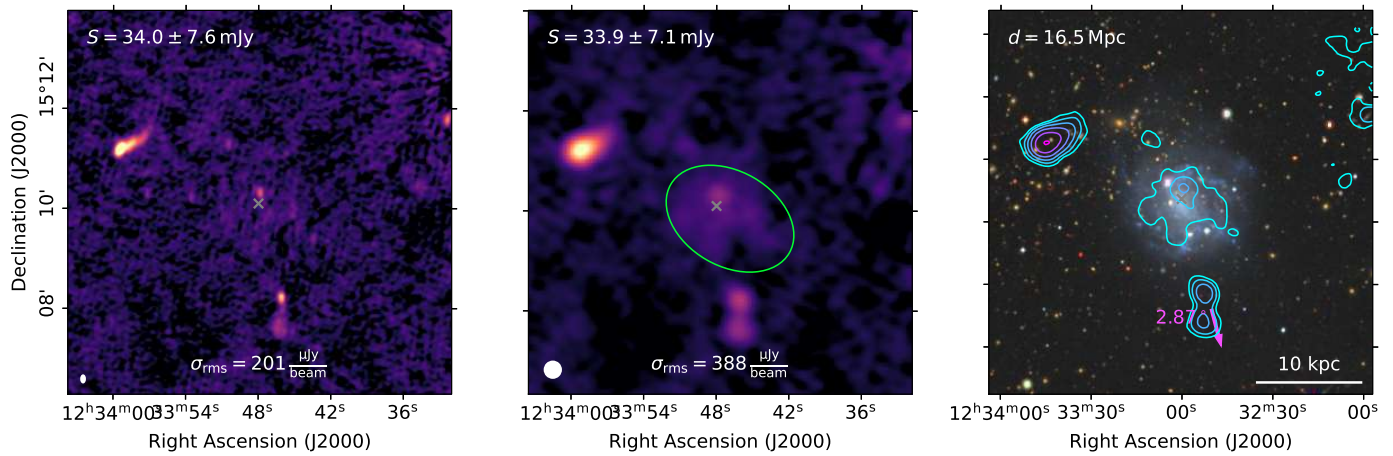
(c)

Fig. A.26: Same as Figure A.1.

IC 800 / VCC 1532

(a)

NGC 4526 / VCC 1535

(b)

NGC 4532 / VCC 1554

(c)

Fig. A.27: Same as Figure A.1.

NGC 4535 / VCC 1555

(a)

IC 3521 / VCC 1575

(b)

NGC 4540 / VCC 1588

(c)

Fig. A.28: Same as Figure A.1.

NGC 4548 / VCC 1615

(a)

NGC 4544 / VCC 1624

(b)

NGC 4552 / VCC 1632

(c)
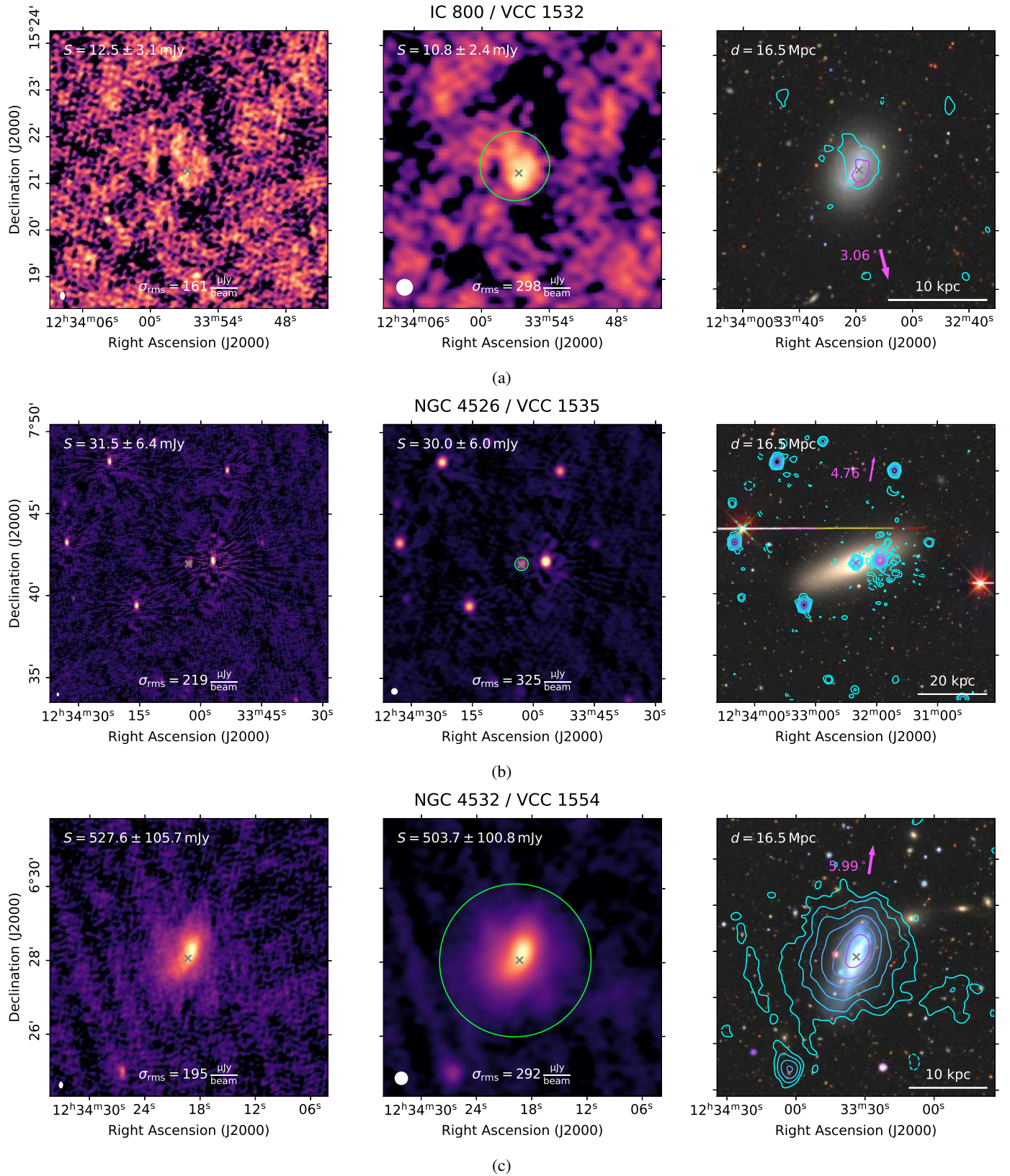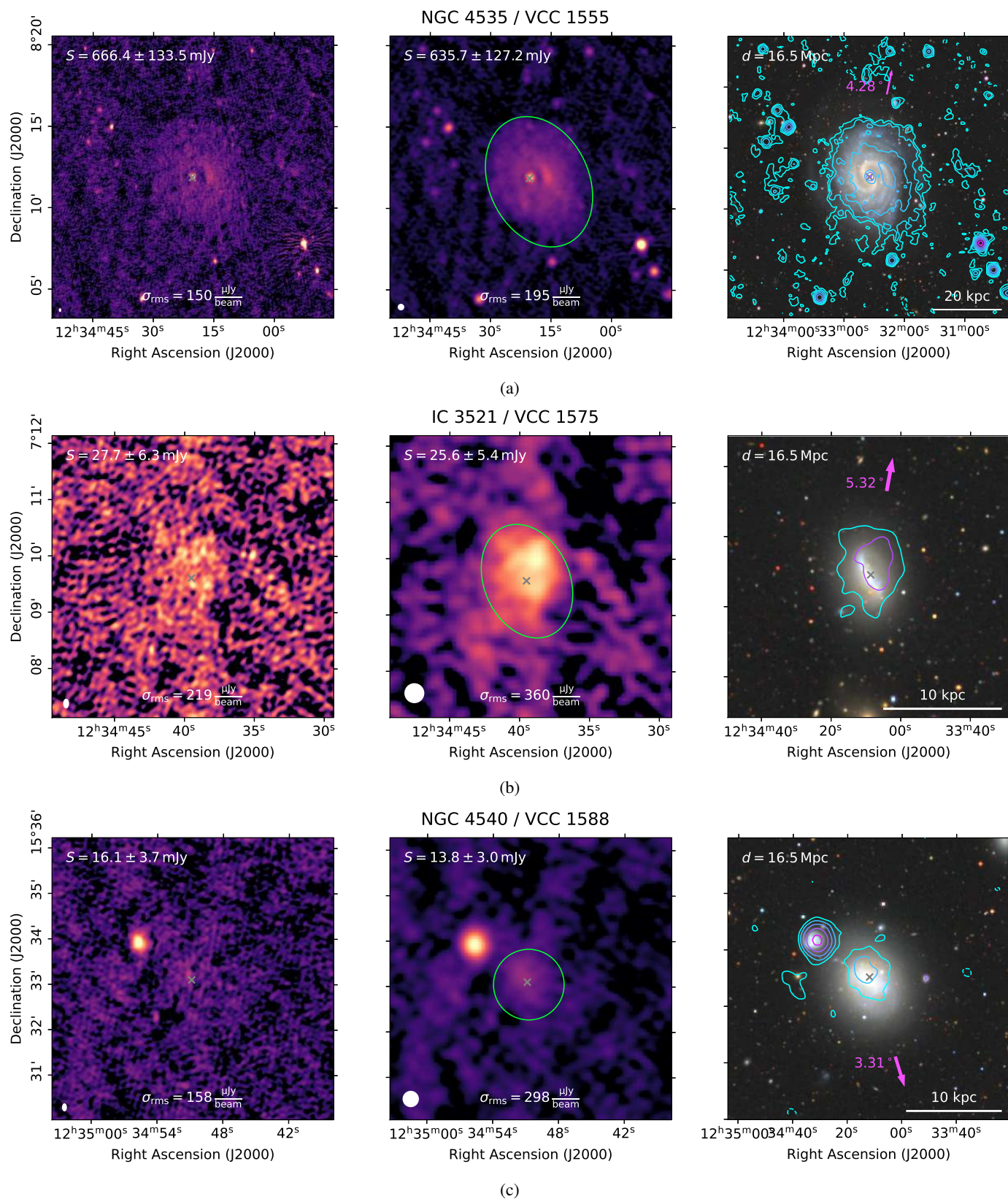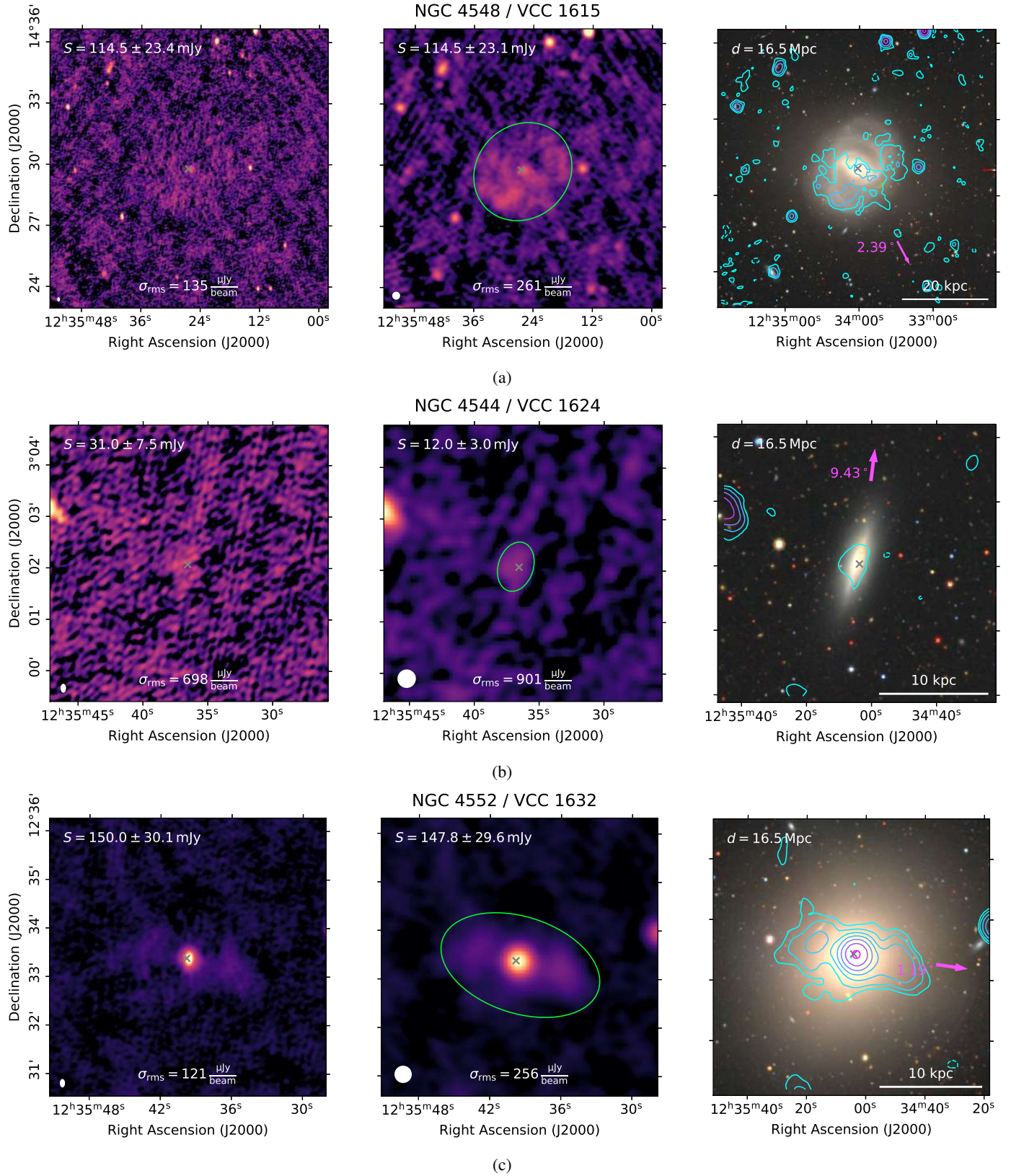
Fig. A.29: Same as Figure A.1.

NGC 4567 / VCC 1673
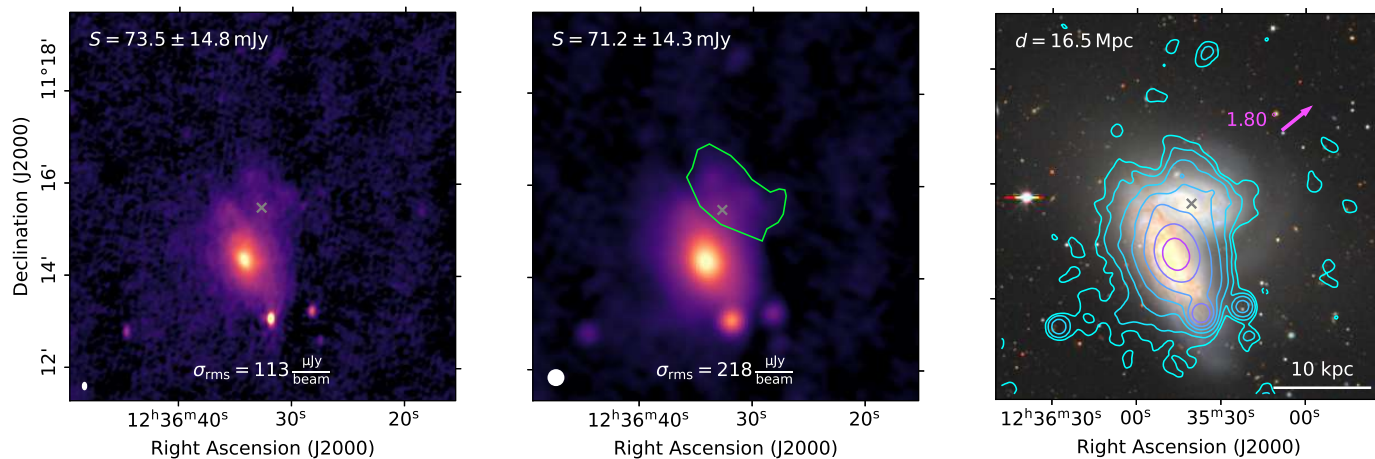
(a)

NGC 4568 / VCC 1676
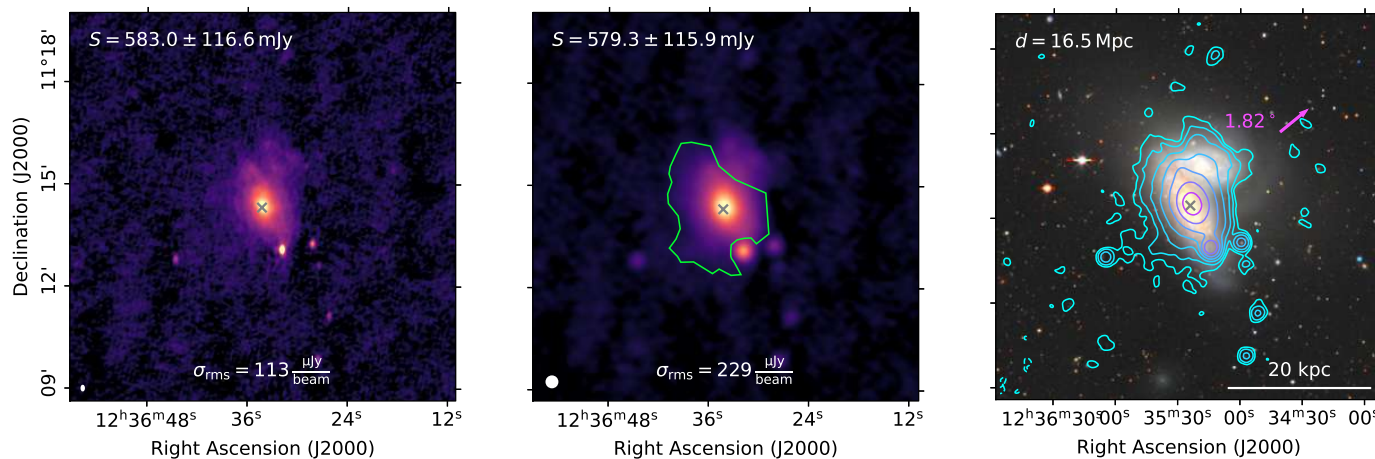
(b)

IC 3583 / VCC 1686
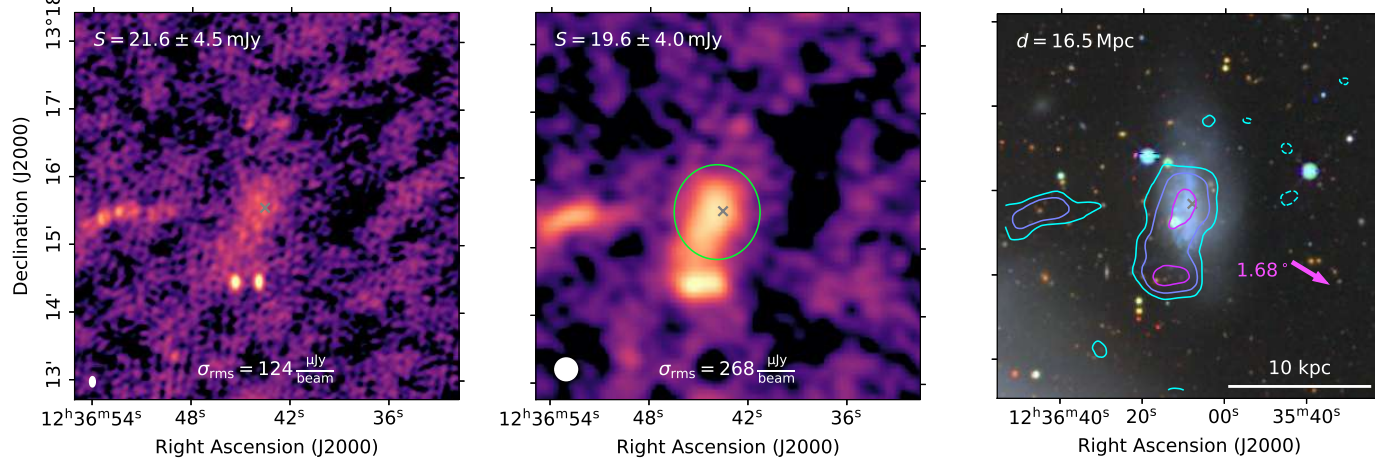
(c)

Fig. A.30: Same as Figure A.1.

NGC 4569 / VCC 1690

(a)

NGC 4571 / IC 3588 / VCC 1696

(b)

NGC 4579 / VCC 1727

(c)

Fig. A.31: Same as Figure A.1.

NGC 4580 / VCC 1730

NGC 4586 / VCC 1760
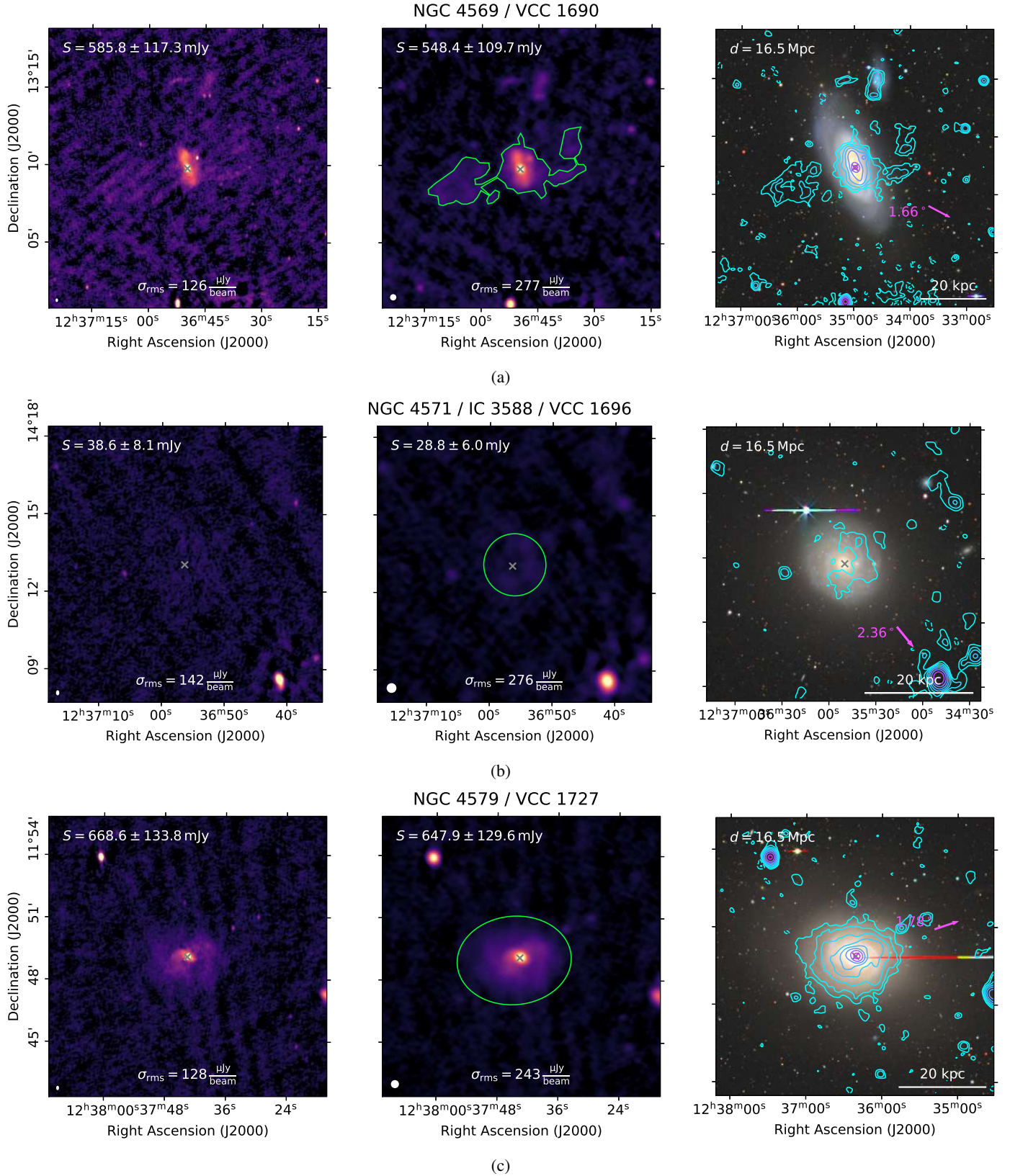
IC 3617 / VCC 1791

Fig. A.32: Same as Figure A.1.

NGC 4595 / VCC 1811

(a)

NGC 4596 / VCC 1813

(b)

NGC 4606 / VCC 1859
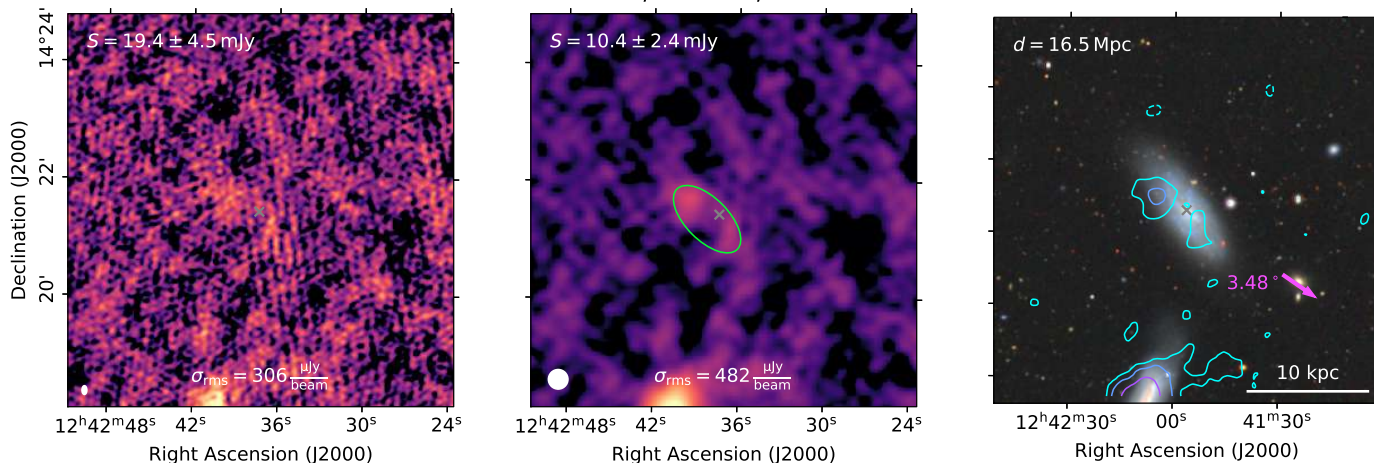

(c)
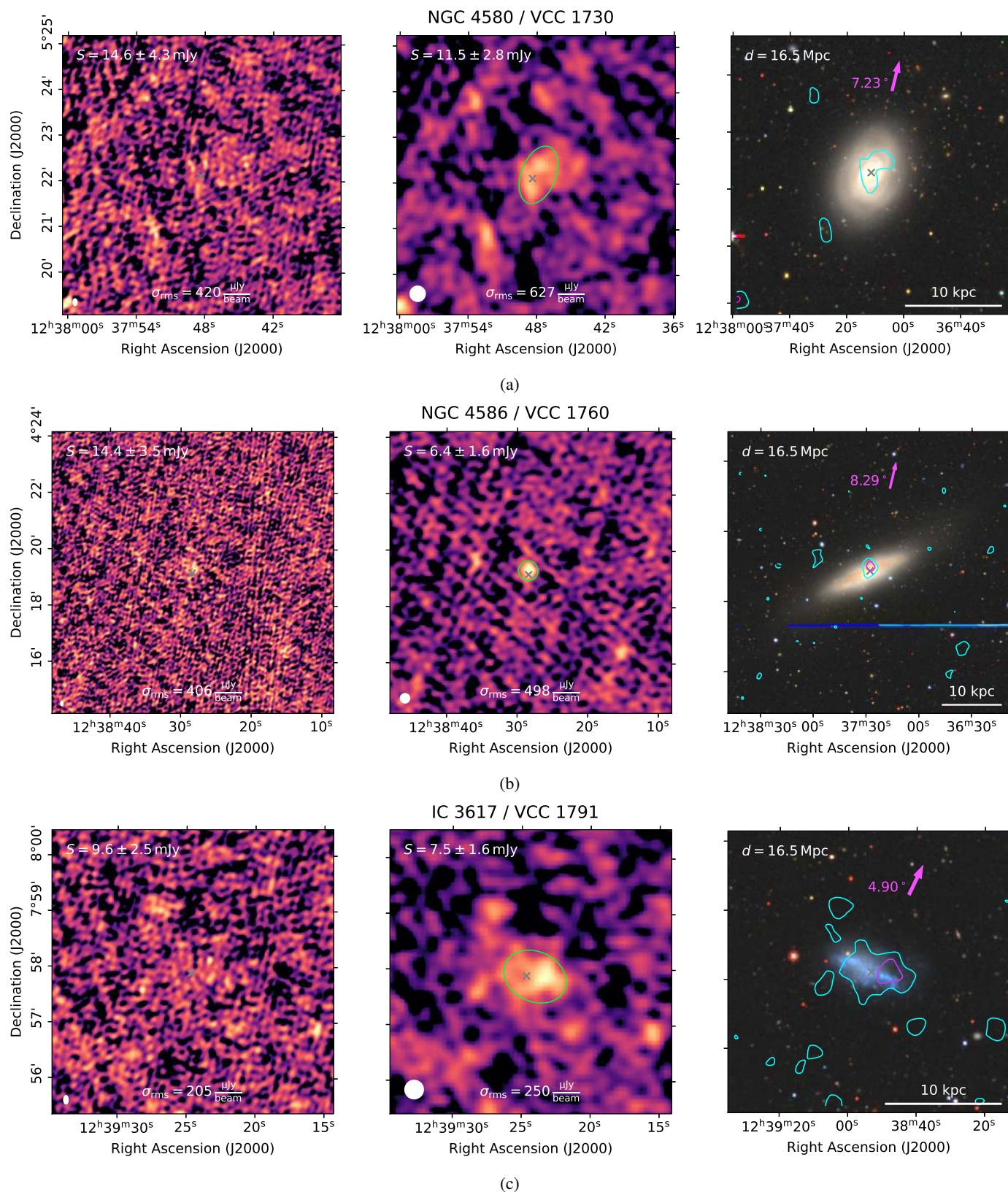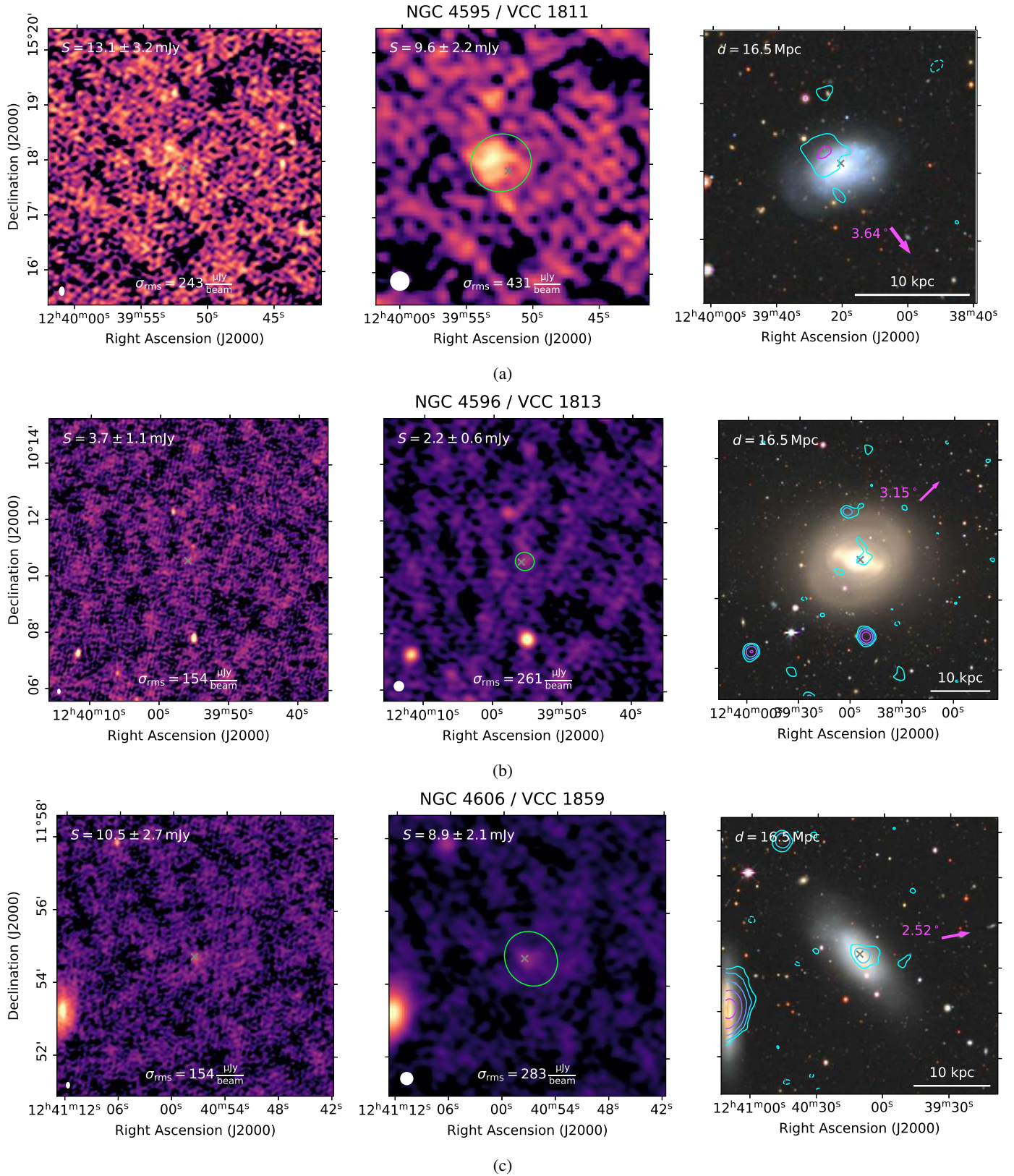
Fig. A.33: Same as Figure A.1.

NGC 4607 / VCC 1868
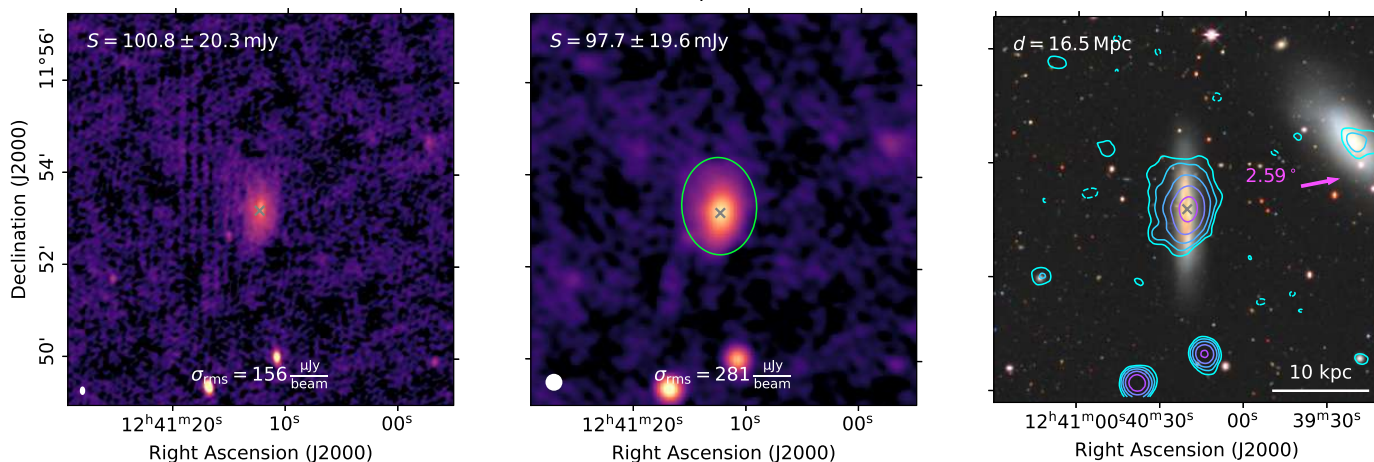
(a)

NGC 4630 / VCC 1923
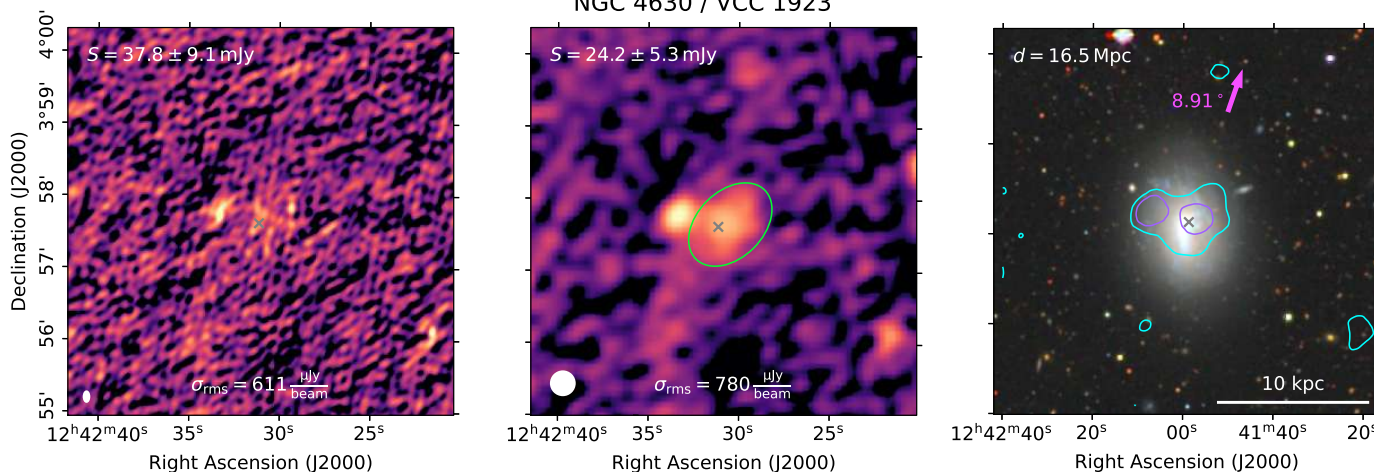
(b)

NGC 4633 / IC 3688 / VCC 1929
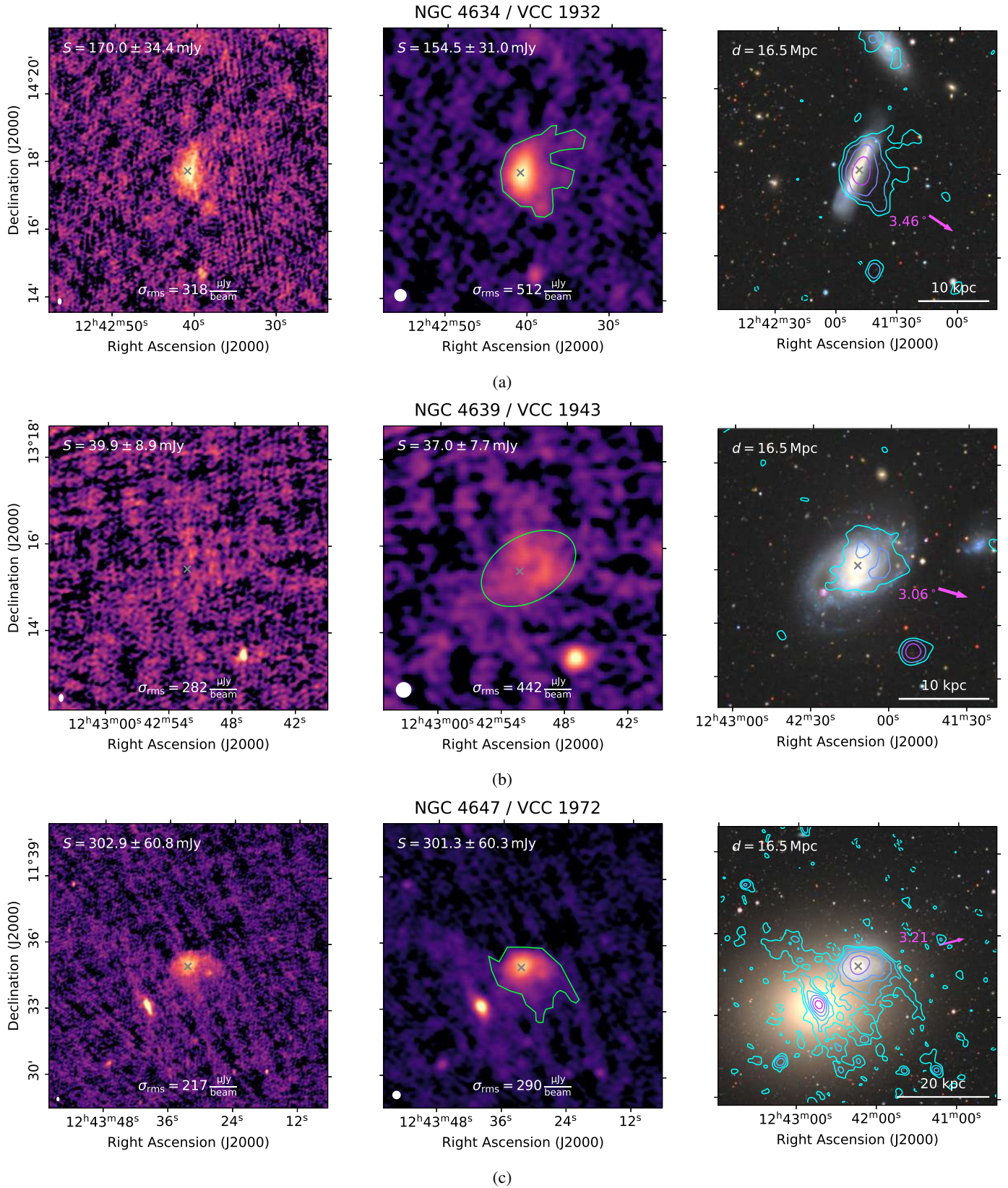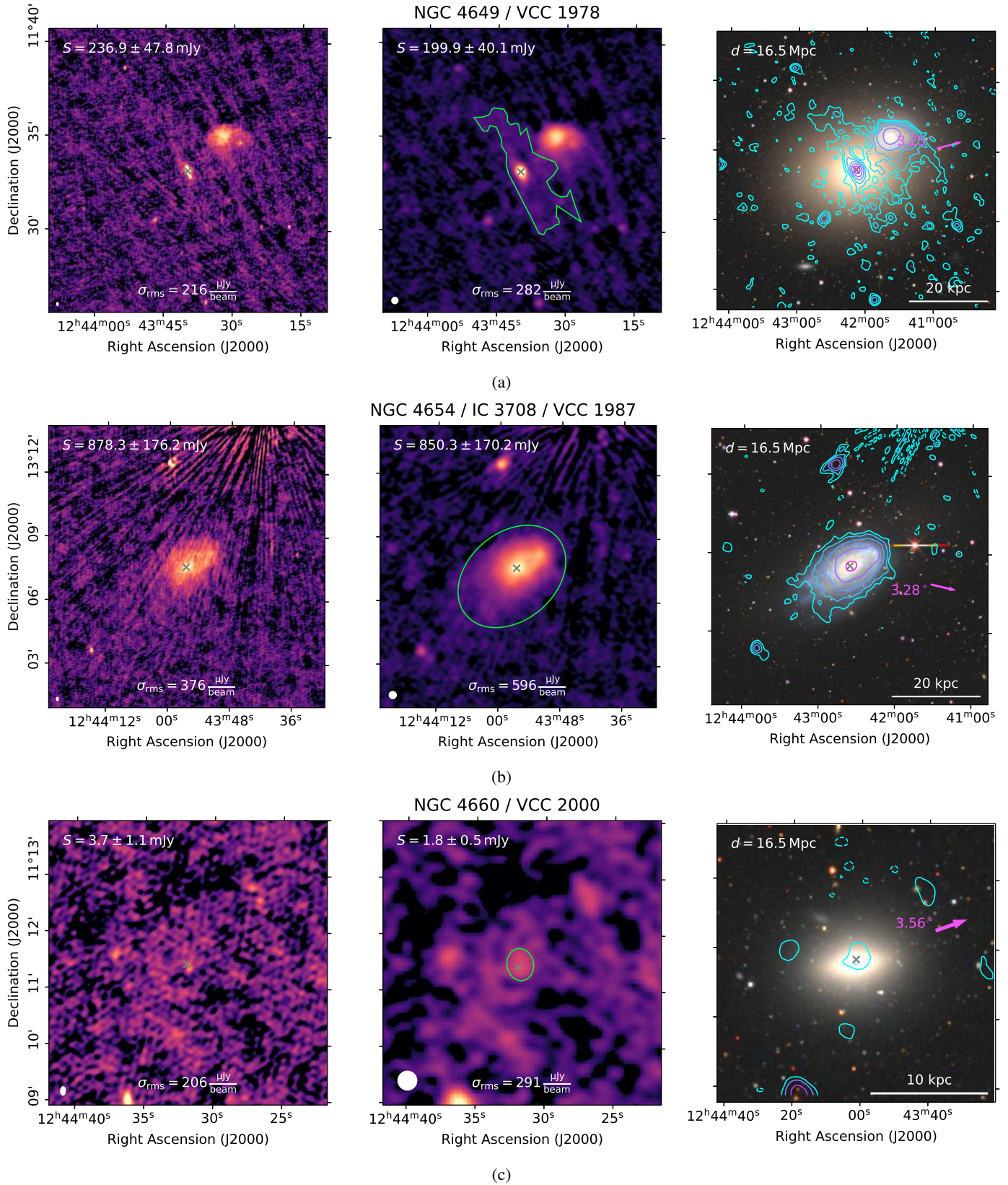

(c)

Fig. A.34: Same as Figure A.1.

NGC 4634 / VCC 1932

(a)

NGC 4639 / VCC 1943

(b)

NGC 4647 / VCC 1972

(c)

Fig. A.35: Same as Figure A.1.

NGC 4649 / VCC 1978

(a)

NGC 4654 / IC 3708 / VCC 1987

(b)

NGC 4660 / VCC 2000

(c)

Fig. A.36: Same as Figure A.1.

NGC 4689 / VCC 2058

(a)

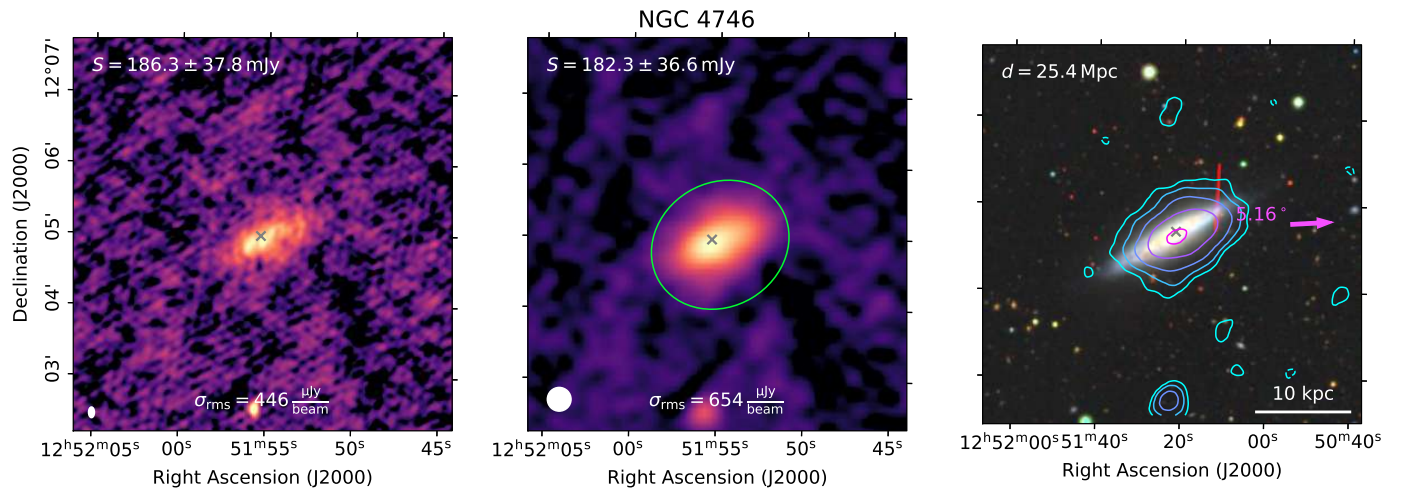## NGC 4694 / VCC 2066

(b)

NGC 4710

(c)
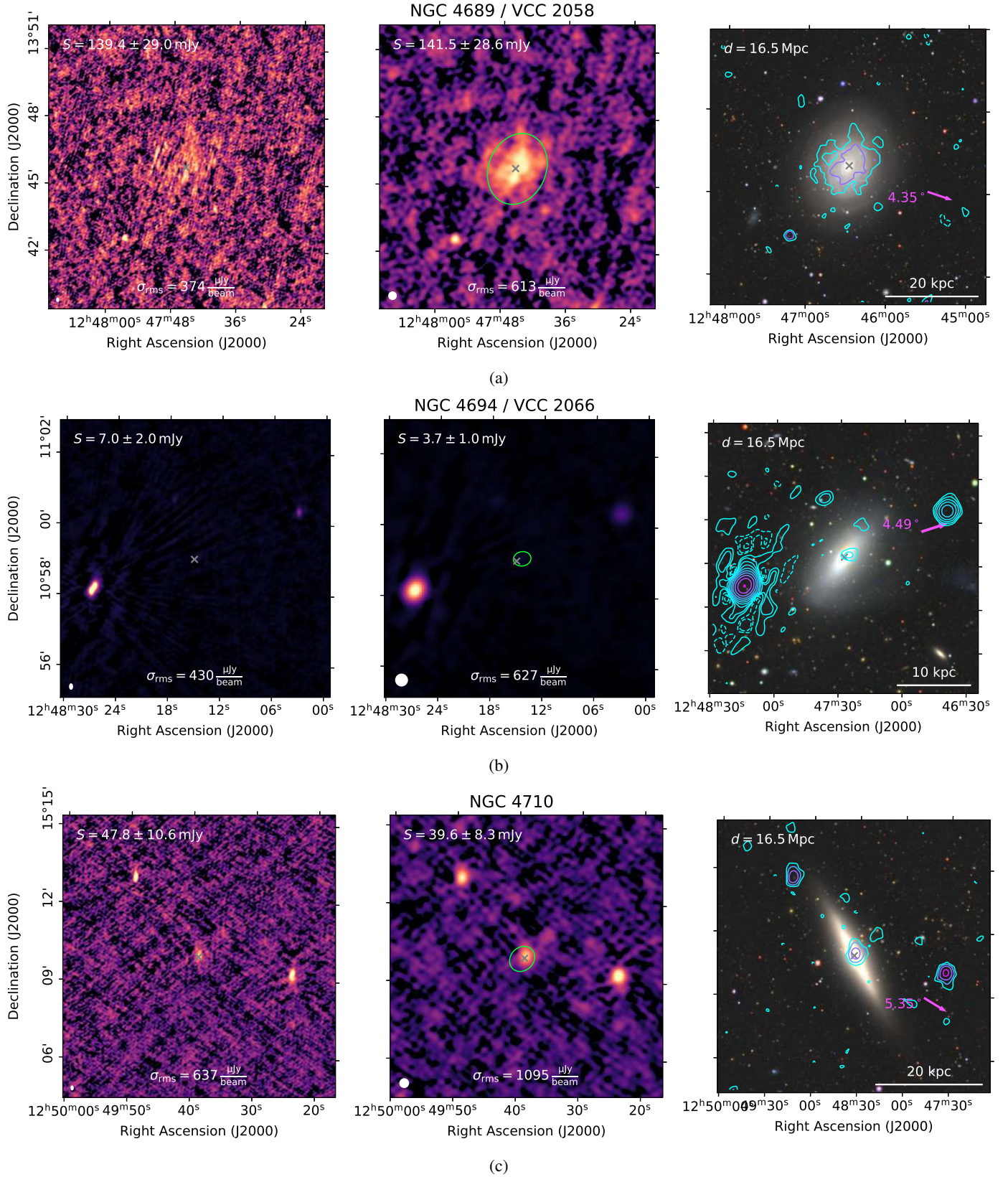
Fig. A.37: Same as Figure A.1.

NGC 4746

Fig. A.38: Same as Figure A.1.